# SIMULTANEOUS VELOCITY AND DENSITY MEASUREMENTS OF FULLY-DEVELOPED RAYLEIGH-TAYLOR TURBULENT MIXING

A Dissertation
Presented to
The Academic Faculty

By

Mark Maged Mikhaeil

In Partial Fulfillment
of the Requirements for the Degree
Doctor of Philosophy in
The George W. Woodruff School of Mechanical Engineering of

Georgia Institute of Technology

May 2020

**SIMULTANEOUS VELOCITY AND DENSITY MEASUREMENTS OF FULLY-DEVELOPED RAYLEIGH-TAYLOR TURBULENT MIXING**

Approved by:


Dr. Devesh Ranjan, Advisor
George W. Woodruff School of Mechanical Engineering
*Georgia Institute of Technology*

Dr. Cyrus Aidun
George W. Woodruff School of Mechanical Engineering
*Georgia Institute of Technology*

Dr. Yogendra Joshi
George W. Woodruff School of Mechanical Engineering
*Georgia Institute of Technology*

Dr. Timothy Lieuwen
Daniel Guggenheim School of Aerospace Engineering
*Georgia Institute of Technology*

Dr. Suresh Menon
Daniel Guggenheim School of Aerospace Engineering
*Georgia Institute of Technology*



Date Approved: December 3, 2019

Blessed be the name of God forever and ever,
For wisdom and might are His.
And He changes the times and the seasons;
He removes kings and raises up kings;
He gives wisdom to the wise
And knowledge to those who have understanding.
He reveals deep and secret things;
He knows what is in the darkness,
And light dwells with Him.

I thank You and praise You,
O God of my fathers;
You have given me wisdom and might,
And have now made known to me what we asked of You,
For You have made known to us the king's demand.

*Daniel 2:20-23*

To God, who has always given me strength.

## ACKNOWLEDGEMENTS

I could not have compiled this dissertation without the help of my mentors, colleagues, friends, family, and other important people in my life.

First and last, I must thank God who gave me the opportunity to start this work, and gave me the strength to complete it. There were many times during the course of this work that I felt the challenges presented were insurmountable, and that I could not overcome them. Through all of these times, He has shown me the faithfulness of His promise:

*but those who hope in the Lord*
*will renew their strength.*
*They will soar on wings like eagles;*
*they will run and not grow weary,*
*they will walk and not be faint.*
-(Isaiah 40:31)

I have no doubt that it was God's will and plan that I would move to Atlanta, perform this research, and write this dissertation. But the opportunity to do this work was manifested through my research adviser and mentor, Professor Devesh Ranjan, to whom I am deeply gracious. These acknowledgements would not be complete without the story of how I was brought into Dr. Ranjan's lab. In 2013, I was an undergraduate at The University of Texas at Austin who was uncertain what career path he wanted to pursue. Professor Llewellyn Rabenberg had seen my proficiency in his class and interest in exploring the lecture material further, and suggested to me that graduate school may be a good option. I applied for undergraduate summer research grants, but I was only offered one at Texas A & M University. The grant was initially offered for me to research compressible flow at the TEES Turbomachinery Laboratory. However, a few weeks before the summer, I received an email from Dr.

Ranjan who had seen my resume and topics of interest, and insisted that I join the Shock Tube and Advanced Mixing laboratory (STAML) for the summer. At the time, I did not understand much about the research conducted at STAML, but I knew that this opportunity would not have appeared, seemingly randomly, unless there was a good reason for it. I accepted Dr. Ranjan's offer and spent the summer completing experiments on the lab's first supercritical carbon dioxide heat-exchanger facility. At the end of the summer, I won 2$^{nd}$ place in the poster competition held among the 200 undergraduate summer research grant recipients based on the measurements I had taken. The following October, while applying to graduate schools, I received a call from Dr. Ranjan explaining that he had accepted a new faculty position at Georgia Tech and that he wanted me to accompany him there to begin my PhD working on the Rayleigh-Taylor instability gas tunnel facility. This project was different from the one I had been working on the summer before, and I had been planning on completing a Masters, not a PhD. But again I knew that this opportunity would not have been presented to me unless there was a good reason. I accepted again, and helped Dr. Ranjan to start the new STAM Lab at Georgia Tech. Since that time, Dr. Ranjan has helped me both in performing ground-breaking research and in developing my career. Through all of the challenges, he has provided guidance and reminded me that nothing worth doing comes easy. Now approaching the end of my graduate school journey, I see that one of the good reasons why God willed for me to complete this specific journey is so that I could learn from Dr. Ranjan and have his support.

This dissertation also would not have been possible without the members of my reading committee: Professor Cyrus Aidun, Professor Yogendra Joshi, Professor Timothy Lieuwen, and Professor Suresh Menon. Their time and feedback on this scientific research has led to my deeper understanding of the material, and the overall improvement of the dissertation. I am grateful to them for their contributions.

I must also thank all of the STAM Lab members, who helped me in both my

research and in my personal growth. Most specially, I must thank my friend and brother-in-arms on the gas tunnel facility, Prasoon Suchandra. It suffices to say that this work would not have been completed without him. Beyond his help in designing, building, and running the experiment, he has encouraged me to always see the positive side of whatever situation we are in, and inspired confidence in me and in my talents. Together, we have shared some failures, some successes, and one Christmas in the lab, and for that shared experience he will forever be a friend to me. I'd also like to thank Stephen Johnston and Dr. Svyatoslav Yorish, who together have served as miracle-workers for the gas tunnel facility. Not once in the course of my PhD work did I encounter a technical issue in the facility or diagnostics which could not be solved by their combined expertise and creativity. For this, and their sacrifice of their time and effort, I thank them deeply. Next, I'd like to thank Dr. Gokul Pathikonda for his help in developing and implementing the diagnostics for the gas tunnel facility. Beyond his diagnostic expertise, Gokul frequently helped to give me a scientific focus and direction and encouraged me to see the silver lining in every experiment run, even if it was not as we desired.

I am also grateful to all the other members of STAM Lab who have provided me with support, ideas and comments: Dr. Mohammad Mohaghar, John Carter, Benjamin Musci, Dan Fries, and Brad Ochs. Special thanks must also be made to the other members of STAM Lab who have been my friends and colleagues over the years: Sam Petter, Steven Roth, Cameron Ahmad, Sam Lim, Alon Katz, Miad Karimi, Jessica Imgrund, Taegyu Kang, Malavika Bagepalli, Justin Yarrington, Dr. Vladimer Tsiklashvili, and Dr. Dorrin Jarrahbashi. I also want to specially thank the many researchers who were present in the lab when I started at Texas A & M University and helped me begin my PhD journey: Dr. Bhanesh Akula, Dr. Jacob MacFarland, Dr. Sandeep Pidaparti, David Reilly, Thomas Finn, and Dr. Sarat Kuchibhatla.

This dissertation would not have been possible without the support of my parents, Maged and Renee Mikhail. They made the hard decision to leave behind their lives in Egypt to come to the United States so that their children would have as many opportunities as possible. Their love, encouragement, guidance, and sacrifice has shaped me into the person I am today. Most importantly, they raised me to believe that anything is possible for those who love God. For that, I always thank them. I'd also like to thank my brother, George Mikhaeil, who is the best of us in the family. He has encouraged me to put everything that I could into this dissertation, because I see that he puts everything he can into all that he does.

Lastly, I'd like to thank my best friend and help-meet Magy Mekhail. Magy and I began dating less than a week after I presented my PhD proposal, after having been friends for nearly ten years. It is no surprise, then, that I see the beginning of our relationship as a turning point in my research. Through all of the challenges I have experienced in completing this PhD, she has always been there with words of encouragement and a reminder that God is capable of all. She has been patient with me to the extreme and has always believed in me, even when I doubted in my ability to finish this dissertation. I cannot express in words how much I thank her for her love and support.

## TABLE OF CONTENTS

**Acknowledgments** . . . . . v

**List of Tables** . . . . . xii

**List of Figures** . . . . . xiii

**Chapter 1: Introduction** . . . . . 1

1.1 Motivation . . . . . 1

1.2 Overview . . . . . 3

1.3 Experimental History . . . . . 10

1.3.1 Single-Mode RTI Experiments . . . . . 10

1.3.2 RTI Experiments in the Fully Turbulent Regime . . . . . 12

1.3.3 Statistically Steady RTI Experiments . . . . . 14

1.3.4 Modern Experimental Studies of RTI . . . . . 16

1.4 RTI Modeling . . . . . 18

1.4.1 Modeling of the non-linear regime . . . . . 19

1.4.2 *RANS*-type models . . . . . 21

1.4.3 The BHR model . . . . . 22

1.5 Objectives . . . . . 25

**Chapter 2: Experimental Methodology** . . . . . 29

2.1 Experimental Facility . . . . . 29

2.1.1 Light Gas Injection System . . . . . 35

2.2 Diagnostics . . . . . 39

2.2.1 Scales for Imaging Diagnostics . . . . . 39

2.2.2 Particle Image Velocimetry . . . . . 41

2.2.3 Laser Induced Fluorescence . . . . . 44

2.2.4 Uncertainty Quantification . . . . . 55

**Chapter 3: Simultaneous Density-Velocity Measurements of the Rayleigh-Taylor Instability** . . . . . 62

3.1 Outline of Experimental Campaign . . . . . 62

3.2 LIF Results . . . . . 65

3.2.1 Volume Fraction and Mixing Width . . . . . 65

3.2.2 Volume Fraction Probability Density Function . . . . . 71

3.3 PIV Results . . . . . 73

3.3.1 Root Mean Square of Velocity Fluctuations . . . . . 75

3.3.2 Self-Similarity of the Velocity Profiles . . . . . 77

3.3.3 Skewness and Kurtosis . . . . . 80

3.3.4 Anisotropy Tensor . . . . . 82

3.4 Simultaneous PIV/LIF Results . . . . . 84

3.4.1 Turbulent Mass Flux . . . . . 84

3.4.2 Reynolds Stress . . . . . 88

3.4.3 Turbulent Kinetic Energy . . . . . 90

3.4.4 Conditional Statistics . . . . . 91

**Chapter 4: Measures of Molecular Mixing . . . . . 96**

4.1 Molecular Mixing Parameter . . . . . 96

4.2 Scalar Dissipation and Total Mixing Rate . . . . . 99

4.3 Density-Specific-Volume Correlation . . . . . 102

4.4 Density-Specific-Volume Correlation Evolution Equation Budget . . . 104

**Chapter 5: Energy Transfer in the Rayleigh-Taylor Instability . . . . 107**

5.1 Potential Energy Release . . . . . 107

5.2 Turbulent Kinetic Energy Evolution Equation Budget . . . . . 111

5.3 Taylor Microscale . . . . . 122

5.4 Estimates of Dissipation . . . . . 125

**Chapter 6: Conclusions . . . . . 128**

**Appendix ARTI Turbulent/Non-turbulent Interface . . . . . 134**

A.1 Introduction . . . . . 134

A.2 Analysis Method . . . . . 137

A.3 Results . . . . . 138

A.4 Conclusions . . . . . 145

**References . . . . . 146**

## LIST OF TABLES


3.1 Outline of experimental settings for the simultaneous PIV/LIF campaign. 64

3.2 Measures of the bubble and spike heights, the half-width of the mixing region, and the mixing centerline for the three Reynolds numbers investigated. . . . . 67

3.3 Calculations of the Richardson number for the three Reynolds number experiments performed. . . . . 73

3.4 Conditional statistics evaluated for the $\mathrm{Re} = 4050$ case at $Y = 0$ . . . 95

5.1 Details on the measured changes in potential energy, turbulent kinetic energy, and dissipated energy for the three Reynolds numbers studied. 110

## LIST OF FIGURES


1.1 Schematics of indirect- and direct-drive ICF. Typical targets used in laser-driven ICF are indirectly driven (upper left) or directly driven (upper right). In either case, a spherical capsule is prepared at $t = 0$ with a layer of DT fuel on its inside surface. As the capsule surface absorbs energy and ablates, pressure accelerates the shell of remaining ablator and DT fuel inwards—an implosion. By the time the shell is at approximately one-fifth of its initial radius it is travelling at a speed of many hundreds of kilometres per second. By the time the implosion reaches minimum radius, a hotspot of DT has formed, surrounded by colder and denser DT fuel. . . . . 2

1.2 The balance of forces at the interface perturbation which lead to the development of RTI . . . . . 3

1.3 The four regimes of the Rayleigh-Taylor instability growth. (a) The exponential growth regime. (b) The saturation regime. (c) The structure formation regime. (d) The turbulent regime. . . . . 5

1.4 Vertical slice of density from a 3D simulation. Overlayed are the mixing widths of the bubble and spike, $h_b$ and $h_s$, measured from the geometric centerline. In a low Atwood number flow, the growth of the bubble and spike are symmetric so that $h_b = h_s = h$. . . . . 8

1.5 RTI simulations performed at Atwood number $\mathcal{A} = 0.15$ and 0.9, showing the asymmetry between the bubble and spike structures that occurs at large $\mathcal{A}$, compared to the symmetry of the Boussinesq instability. . 10

2.1 3D render of the gas tunnel facility. . . . . 29

2.2 Coordinate system of the gas tunnel. $x$, $y$, and $z$ represent the streamwise, cross-stream, and span-wise directions with respect to the flow, respectively. To illustrate the splitter plate location, the wire mesh grid has not been shown. . . . . 30

2.3 3D renderings of the bottom half of the gas tunnel facility settling section. Green arrows represent the flow direction of gas into and out of the settling section. The gas injection and PIV injection setup have been removed for clarity. (a) A model illustrating the arrangement and orientation of mixing fans and support beams in the settling section, with red arrows representing the flow direction of each fan. (b) A model illustrating the sliding grates that can be used to increase the major pressure losses in the bottom stream. . . . . 32

2.4 The impact of the addition of the mixing fans on the mean concentration profile $\overline{C}$, fluctuating concentration profile $C'$, and normalized fluctuating vertical velocity profile $v'/\overline{u}$. Measurements are taken at the $x = 1.25\,\mathrm{m}$ location. . . . . 33

2.5 A schematic of the light gas injection system and acetone bubbler system before injection into the gas tunnel. . . . . 35

2.6 A simplified schematic showing the PIV and LIF laser, optics, and camera setups. . . . . 41

2.7 A 3D model of the acetone bubbler with cross-section cutout . . . . . 46

2.8 Images showing the methodology for processing the LIF images (1/3). Raw images first go through background subtraction, and are then transformed to world coordinates through the use of previously acquired calibration images. . . . . 50

2.9 Images showing the methodology for processing the LIF images (2/3). Coordinate transformed images are masked, and pixel intensity is summed across $x$ to obtain the variation in line intensity along the beam path 51

2.10 Images showing the methodology for processing the LIF images (3/3). Raw line intensities are vignette corrected, filtered, scaled to the appropriate concentrations, and stitched to form the final concentration profile. . . . . 52

2.11 Examples of the relative PIV uncertainty fields for both $u$ and $v$, measured at the three mixing Reynolds numbers. . . . . 57

3.1 The variation of experimental Atwood number and associated uncertainty (95 % confidence interval) over time for all six total experimental runs, comprising three Reynolds number experiments. . . . . 65

3.2 Profiles of the mean volume fraction of the heavy gas stream, $\overline{f_1}$, at the three Reynolds numbers tested. . . . . 66

3.3 Normalized profiles of the mean volume fraction of the heavy gas, $\overline{f_1}$ for the three Reynolds numbers tested. Superimposed is an error function profile of equal width. . . . . 68

3.4 Normalized profiles of the mean volume fraction of the heavy gas, $\overline{f_1}$ for the three Reynolds numbers tested, but with the spatial coordinate normalized by $h_f$ instead of $h$. . . . . 69

3.5 Normalized profiles of the root-mean-square density fluctuation for the three Reynolds numbers tested. . . . . 71

3.6 Probability density functions of the volume fraction of the heavy gas, $f_1$, for the three Reynolds numbers tested at 5 normalized $y$-coordinate locations. . . . . 72

3.7 Profiles of the mean horizontal and vertical velocity, $u$ and $v$, respectively, together with the associated uncertainty. . . . . 74

3.8 Profiles of the root mean square of the fluctuation of the horizontal and vertical velocity components, $u'_{\mathrm{RMS}}$ and $v'_{\mathrm{RMS}}$, together with the associated uncertainty in the statistic. . . . . 75

3.9 The maximum $u'_{\mathrm{RMS}}$ and $v'_{\mathrm{RMS}}$ at each downstream location $x$ measured, against the instability development time for that $x$ location, $t$. The line through the $v'_{\mathrm{RMS}}$ points describes the least-square linear fit. 76

3.10 Profiles of the RMS horizontal and vertical velocity fluctuations, normalized by the Goncharov bubble velocity. . . . . 78

3.11 Profiles of the skewness and kurtosis of the horizontal and vertical velocity fluctuations for the three Reynolds numbers tested. . . . . 81

3.12 Profiles of the components of the anisotropy tensor, $b_{ij}$, for the Re = 4050 experimental case. . . . . 83

3.13 Profiles of the negative vertical turbulent mass flux, $a_y$, together with the associated uncertainty in the statistic. . . . . 84

3.14 The probability density function of the density-velocity correlation, $\rho' v'$, after normalization for the Re = 2260 and Re = 4050 cases, evaluated at $Y = 0$. . . . . 86

3.15 Profiles of the negative vertical turbulent mass flux, $a_y$, normalized by the self-similar velocity scale, $U_{h_f}^2$. . . . . 87

3.16 Profiles of the Reynolds stress components, $R_{xx}$ and $R_{yy}$, normalized by the mean density profile and the self-similar velocity, $U_{h_f}$, for the three Reynolds numbers tested . . . . . 88

3.17 Profiles of the relative contribution of terms in the Reynolds Stress decomposition, T1, T2, and T3, normalized by the total Reynolds stress, $R_{ij}$ for both $R_{xx}$ and $R_{yy}$. Profiles are presented from the Re = 4050 case. . . . . 89

3.18 Profiles of the turbulent kinetic energy, $k$, normalized by the self-similar velocity scale, $U_{h_f}$. . . . . 90

3.19 Probability density functions of the normalized density, velocity, and density-velocity correlation for the sampling conditions $\rho' < 0$ and $\rho' > 0$. 92

3.20 Probability density functions of the normalized velocity, density, and density-velocity correlation for the sampling conditions $v' < 0$ and $v' > 0$. 94

4.1 Profiles of the molecular mixing parameter, $\theta$, for the three Reynolds numbers tested. . . . . 97

4.3 Profiles of the mean scalar dissipation, $\overline{\chi}$, for the three Reynolds numbers tested. . . . . 100

4.4 The integral of the scalar dissipation over the domain, also known as the total mixing rate of the flow, at each Reynolds number tested. . . 101

4.5 Profiles of the density-specfic-volume correlation, $b$, for the three Reynolds numbers tested, along with the associated error in the statistic. . . . 103

4.6 Profiles of the density-specific-volume correlation, $b$, normalized against the maximum possible value of $b$ given the volume fractions present at the spatial location, $b_{\max}$ . . . . . 104

4.7 Profiles of the terms of the density-specific-volume correlation evolution equation budget, T2, T3, T4, and their sum for the Re = 4050 case. . . . . 106

5.1 The ratio of turbulent kinetic energy generated by the RTI, $\Delta KE$, and dissipated energy, $D$, compared to the potential energy released in the flow, $\Delta PE$ for the three Reynolds numbers tested. . . . . 109

5.2 Profile of the advection term, $C^k$, and the relative contributions of the horizontal and vertical gradient terms. . . . . 115

5.3 Profile of the production term, $P^k$, and the relative contributions of the velocity gradient stretching term and the variable density pressure gradient term. . . . . 116

5.4 Profile of the turbulent transport term, $D^k$, and the relative contributions of the horizontal and vertical velocity fluctuations. . . . . 118

5.5 Profile of the dissipation, $\epsilon^k$. . . . . 120

5.6 Profiles of the terms of the $k$ budget, evaluated for the Re = 4050 case. 121

5.7 Profiles of the Taylor microscale $\lambda_{v,y}$ measured based on $y$ gradients of the vertical velocity fluctuation, $v'$, for the three Reynolds numbers tested. Results are normalized based on the half-width of the mixing region. . . . . 123

5.8 Profiles of the Taylor microscales measured based on $x$ and $y$ gradients of the horizontal and vertical velocity fluctuations, $u'$ and $v'$ for the Re = 4050 experimental case. . . . . 124

5.9 Profiles of the Taylor microscale $\lambda_{v,x}$ measured based on $x$ gradients of the vertical velocity fluctuation, $v'$, for the three Reynolds numbers tested. Results are normalized based on the half-width of the mixing region and the inverse square root of the Reynolds number, $\mathrm{Re}^{-1/2}$. . 125

5.10 Profiles of the dissipation of turbulent kinetic energy found using the Taylor microscale and the $k$ budget. . . . . 127

A.1 Left: Cross section image of an RTI direct numerical simulation. Right: Cross section image of a turbulent jet experiment. . . . . 134

A.2 A schematic of the turbulent/non-turbulent interface bounding the turbulent region of an RTI mixing layer. . . . . 136

A.3 Four instantaneous measurements of the volume fraction profile, found using LIF, together with the bubble interface location found using a 95 % threshold. . . . . 137

A.4 The probability density function of the normalized interface location, $Y_I$, for the Re = 4050 case. . . . . 139

A.5 The profile of the interface conditionally averaged volume fraction, $\langle f_1 \rangle_I$, for the Re = 4050 experiment. . . . . 140

A.6 A mie scattering visualization image taken at the Re = 4050 downstream location, showing the general shape of the bubble structure . . 141

A.7 The profile of the interface conditionally averaged horizontal and vertical velocity fluctuations, $\langle u'u' \rangle_I^{1/2}$ and $\langle v'v' \rangle_I^{1/2}$, for the Re = 4050 experiment, normalized by the Goncharov bubble velocity, $v_\infty$. . . . . 142

A.8 The profile of the interface conditionally averaged spanwise vorticity, $\langle \omega'\omega' \rangle_I^{1/2}$, for the Re = 4050 experiment, normalized by the Goncharov bubble velocity, $v_\infty$, and the mixing height, $h$. . . . . 143

A.9 The profile of the interface conditionally averaged scalar dissipation, $\langle \chi \rangle_I$, for the Re = 4050 experiment. . . . . 144

## SUMMARY

The dynamics of molecular mixing and the energy transfer process in the Rayleigh-Taylor instability (RTI) are studied through the collection and analysis of simultaneous density-velocity field measurements. Statistically stationary experiments are performed in the "convective-type" gas tunnel facility, with density contrast achieved through the injection of helium into the bottom stream. To observe the structure of the self-similar regime, three experiments at Atwood number $\mathcal{A} \approx 0.1$ are captured at three outer-scale Reynolds numbers, 520, 2260, and 4050. To study the mixing and dynamics of the flow, both particle image velocimetry (PIV) and laser induced fluorescence (LIF) are employed simultaneously. This allows, for the first time in an RTI flow, the simultaneous field measurement of velocity and density. Together, these can be used to measure statistics of velocity, density and velocity-density cross-correlated terms. The experimental understanding of the interaction between the large-scale motion of the RTI bubble and spike structures and the resulting mixing and energy transfer will serve as a useful validation tool for predictive turbulence models. This will help develop our understanding of a variety of physical phenomena, most importantly the ignition of Type Ia supernovae, and the implosion of the inertial confinement fusion (ICF) fuel target.

Statistics of the volume fraction, density, and velocity show self-similar collapse of RTI profiles at large Reynolds number $\mathrm{Re} > 2000$. The probability density function of the volume fraction shows an increase in mixed material at the center of the mixing region as Reynolds number increases, but the presence of unmixed entrained fluid in the core persists. Flat velocity profiles indicate homogeneous turbulence characteristics in the core of the mixing region. Significant anisotropy develops in the flow, with horizontal velocity fluctuations being only 60 % of the vertical velocity fluctuations. Meanwhile, the turbulent mass flux, the leading term in the production

of turbulent kinetic energy in the flow, is shown to be asymmetric with increased peak towards the spike.

Measurements of the molecular mixing show that mixing is maximized at the core of the flow and increases with increased Reynolds number. However, the rate of mixing peaks at Reynolds number around 2260, suggesting a regime transition in the flow around this Reynolds number. The analysis of the density-specific-volume correlation, $b$, shows that the potential for mixing is mostly limited in the flow by the relative concentrations of the top and bottom fluid. The transport equation of $b$ shows that it is mostly produced in the core of the mixing region, but that the spatial evolution of its profile is the result of transport by bulk motion of the bubble and spike.

Energy transfer from gravitational potential energy to turbulent kinetic energy and viscous dissipation is observed to occur in the experiment with a ratio of dissipated energy to potential energy released of 38 %. The analysis of the turbulent kinetic energy transport equation budget reveals that production is the dominant mechanism towards the growth of turbulent kinetic energy of the flow, and is asymmetrically skewed towards the spike. The viscous dissipation is also skewed towards the spike, suggesting that it serves as a balancing mechanism for the growth rate of turbulent kinetic energy. The budget of turbulent kinetic energy reveals the nature of the energy transfer process in the flow, from the production of turbulent kinetic energy at the core of the flow to its transport to the edges by large-scale fluctuations of the bubble and spike structures.

# CHAPTER 1
# INTRODUCTION

## 1.1 Motivation

Rayleigh-Taylor instability (RTI) driven turbulent mixing occurs in a variety of phenomena extending an enormous range of scales. At astronomical scales, RTI mixing is an important mechanism in the understanding of Type Ia supernovae [1–4]. These supernovae occur when a white dwarf in a binary star system accretes mass from its binary companion, increasing its mass and temperature and igniting a carbon fusion reaction in its core. As the deflagration front of the reaction propagates to the star's surface, it leaves behind an expanding region of low density fusion products surrounded by high density unreacted material. The resulting configuration is RTI unstable and the instability development affects the propagation of the deflagration front. Because of their use as standard candles, the proper modeling of Type Ia supernovae is critical to the accurate measurement of cosmic distances and the expansion rate of the universe.

At micron scales, RTI hydrodynamics play an integral part in the physics of inertial confinement fusion (ICF) [6–11]. The ICF target is composed of a spherical shell of ablator material, around 1 mm in diameter, filled with deuterium-tritium (DT) gas. The target can be driven either directly or indirectly, and the subsequent ICF process is outlined in figure 1.1. A driver rapidly delivers high energy laser radiation to the ablator, which undergoes phase change to a plasma and expands. The expansion of the outer ablator compresses the inner DT gas to a radius 30 to 40 times smaller than the initial radius, initiating a fusion reaction in the "hot-spot" at the core of the gas. As the temperature of plasma in the hot-spot increases, the plasma expands

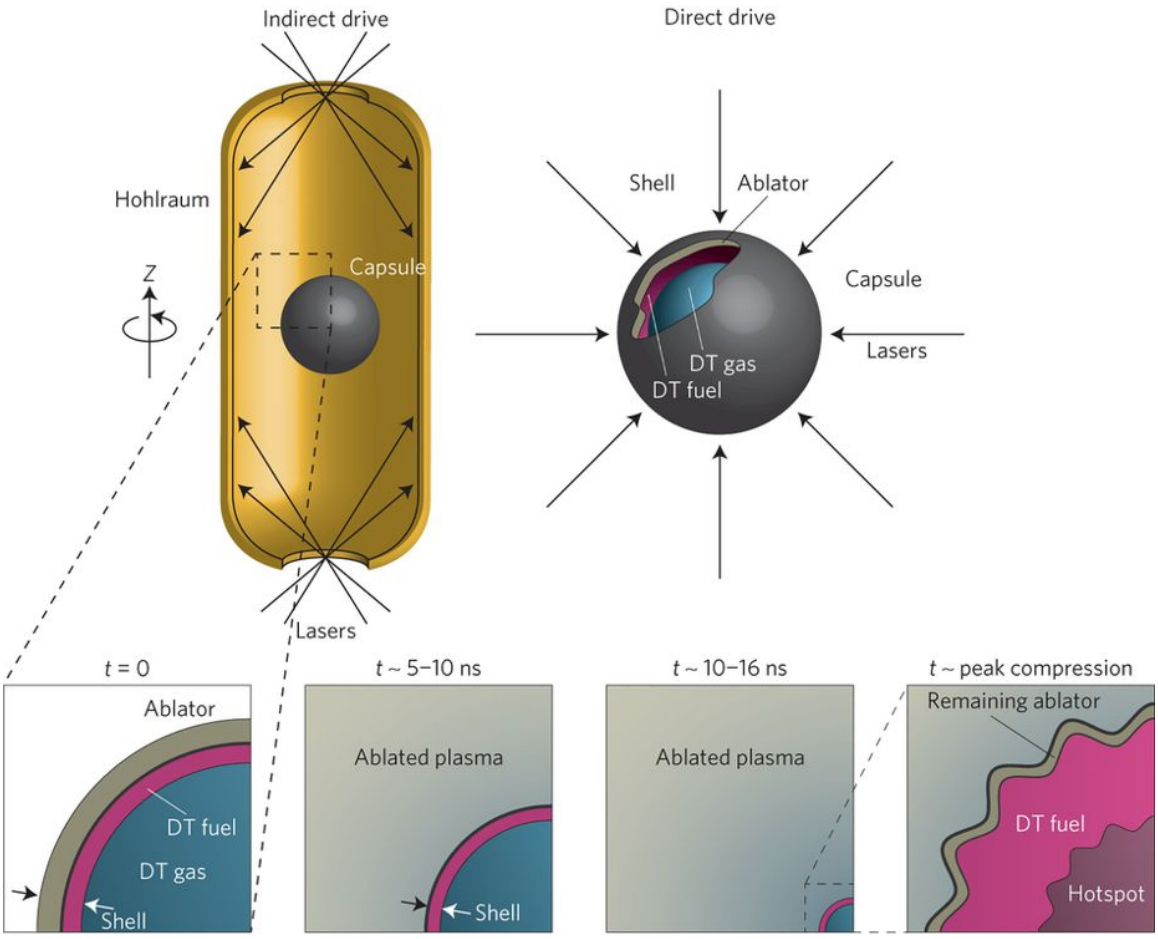


Figure 1.1: Schematics of indirect- and direct-drive ICF. Typical targets used in laser-driven ICF are indirectly driven (upper left) or directly driven (upper right). In either case, a spherical capsule is prepared at $t = 0$ with a layer of DT fuel on its inside surface. As the capsule surface absorbs energy and ablates, pressure accelerates the shell of remaining ablator and DT fuel inwards—an implosion. By the time the shell is at approximately one-fifth of its initial radius it is travelling at a speed of many hundreds of kilometres per second. By the time the implosion reaches minimum radius, a hotspot of DT has formed, surrounded by colder and denser DT fuel.
*Source:* Figure 1, Betti and Hurricane [5], with permission.

and causes the compression to decelerate. There are two occurrences of RTI in the ICF process. The first is when the low density plasma ablator material expands and compresses the high density, low temperature DT gas. The second is when the low density plasma in the core hot-spot expands and decelerates the high density shell compressing into it. Because hydrodynamic effects like RTI affect the motion of the entire target, they are considered to be the strongest effects in the ICF process [12].

Correctly modeling RTI and other hydrodynamic effects is essential to the design of ICF targets and achieving the dream of using controlled thermonuclear fusion as a means of energy production.

Between these two examples of RTI turbulent mixing at extreme conditions exist many other natural and synthetic situations including spray atomization [13], premixed combustion [14], salt dome formation [15], estuary flow [16], and atmospheric and oceanic convection [17]. In all of these scenarios, the difference in density between fluids in a gravitational or acceleration field lead to perturbation growth, and the fundamental understanding of RTI is crucial to the development of theories and predictive models.

## 1.2 Overview

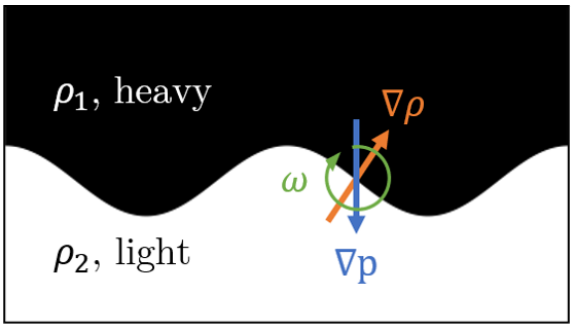


Figure 1.2: The balance of forces at the interface perturbation which lead to the development of RTI

The Rayleigh-Taylor instability (RTI) occurs at the unstable perturbed interface between two fluids of different densities. To illustrate the balance of moments at the interface, consider a simplified schematic of the unstable interface shown in Figure 1.2, and examine the vorticity equation for compressible fluids only experiencing conservative body forces, equation 1.1.

$$\frac{D\omega}{Dt} = (\omega \cdot \boldsymbol{\nabla})u - \omega(\boldsymbol{\nabla} \cdot u) + \boldsymbol{\nabla} \times \left(\frac{1}{\rho}\boldsymbol{\nabla} \cdot \tau\right) + \frac{1}{\rho^2}\boldsymbol{\nabla}\rho \times \boldsymbol{\nabla}p \qquad (1.1)$$

If the gradients of pressure and density are misaligned such that $\boldsymbol{\nabla} p \cdot \boldsymbol{\nabla} \rho < 0$, then the final term of equation 1.1 is non-zero and baroclinic vorticity is deposited at the interface. This causes the interface to roll-up in such a way as to grow the perturbation. In many applications, the pressure gradient is caused by hydrostatic forces, governed by the gravitational acceleration $g$. The density gradient is caused by differences in densities between the heavy fluid with density $\rho_1$ and the light fluid with density $\rho_2$. The difference between the densities is non-dimensionalized by the Atwood number $\mathcal{A}$ defined by equation 1.2.

$$\mathcal{A} = \frac{\rho_1 - \rho_2}{\rho_1 + \rho_2} \tag{1.2}$$

The range of possible values of $\mathcal{A}$ is from zero to unity, with zero representing two fluids of identical density and unity representing the limit of a fluid pair where the heavy fluid is infinitely more dense than the light fluid. At small values of $\mathcal{A}$, the flow may be analyzed using a Boussinesq approximation [18]. In other words, the variation of density is considered to have negligible impact on the inertial properties of the fluid, and only serves to cause buoyant forces. As $\mathcal{A}$ exceeds approximately 0.2 and approaches unity, the Boussinesq approximation becomes invalid and variable density effects have significant importance in the inertial properties of the fluid and subsequently on the production of turbulence.

Sharp [19] delineates the growth of the instability into four regimes, which are shown in figure 1.3. In the initial stages of the instability, the amplitude of the perturbation $\eta$ is much smaller than the wavelength $\lambda$. Early investigations of RTI in this regime applied linear stability theory to analyze the instability growth rate and, for simplicity, assumed fluids that were incompressible and invsicid with no surface tension at their interface. This was the approach of Lord Rayleigh [20], who performed the linear stability analysis on the equations of motion and Taylor [21] who considered the velocity potentials of the flow. Both showed that the perturbation amplitude grew

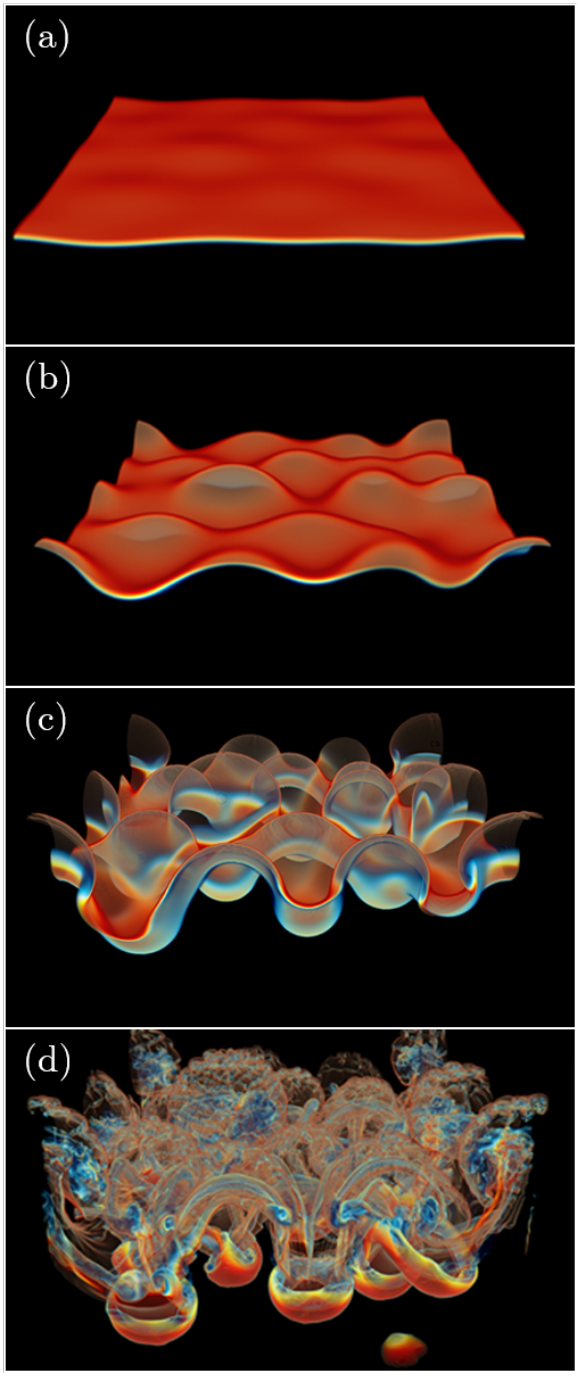


Figure 1.3: The four regimes of the Rayleigh-Taylor instability growth. (a) The exponential growth regime. (b) The saturation regime. (c) The structure formation regime. (d) The turbulent regime.

exponentially with time $t$, as shown in equation 1.3, with growth rate $\gamma$ described by

equation 1.4 where $\kappa = 2\pi/\lambda$ is the perturbation wavenumber.

$$\eta(t) = \eta(0)e^{\gamma t} \tag{1.3}$$

$$\gamma^2 = \kappa g \mathcal{A} \tag{1.4}$$

Equation 1.4 is the dispersion relation for incompressible, inviscid RTI flows with no surface tension. It shows that smaller wavelength perturbations grow faster than larger wavelength structures at a rate that depends exponentially on their size. In the case of viscous fluids, the dispersion relation deviates from equation 1.4 and in general cannot be solved analytically [22]. Viscosity has the effect of reducing the growth rate of small wavelength perturbations, leading to the existence of a most unstable wavenumber $\kappa_{max}$ at which $\gamma$ is a maximum. The computation of $\kappa_{max}$ and $\gamma(\kappa_{max})$ can be performed numerically and is dependent on $\mathcal{A}$ and the viscosities of the fluids [23]. However, a useful approximation for the most unstable wavelength $\lambda_{max} = 2\pi/\kappa_{max}$ is provided by Plesset and Whipple [24] as

$$\lambda_{max} = 4\pi \left( \frac{\tilde{\nu}^2}{\mathcal{A}g} \right)^{1/3} \tag{1.5}$$

with the mixed fluid viscosity, $\tilde{\nu}$, defined as

$$\tilde{\nu} = \frac{\mu_1 + \mu_2}{\rho_1 + \rho_2} \tag{1.6}$$

where $\mu_1$ and $\mu_2$ are the dynamic viscosities of the heavy and light fluid, respectively. In any case, the perturbation grows exponentially until the amplitude becomes approximately half the wavelength and non-linear effects become important [25].

In the second regime, the evolution of the perturbation is strongly affected by non-linearity and three-dimensional effects and the generation of larger structures.

These structures take on the appearance of alternating and interpenetrating *bubbles* of rising light fluid and *spikes* of falling heavy fluid. The shape of the bubble and spike structures is strongly influenced by $\mathcal{A}$. If $\mathcal{A} \approx 0$, the bubble and spike structures are largely symmetric, but as $\mathcal{A} \to 1$, asymmetry develops between the bubble and the spike leading to wide, round bubbles separated by narrow, sharp spikes. In this regime, the growth rate of the bubbles saturate to a terminal velocity called the bubble velocity $v_\infty$. $v_\infty$ is dependent on $\mathcal{A}$, $\kappa$, $g$, and the geometry of the instability, and is the subject of significant theoretical effort [26–28].

The third regime is characterized by the continued growth and non-linear interaction of the bubble and spike structures. As the bubble and spike move past one another, shear causes Kelvin-Helmholtz instabilities (KHI) to develop causing the generation of roll-ups and mushroom-cap like structures on the interface. If the initial perturbation is multimodal in character, modal interaction will appear in two general forms [29–32]. The first, mode competition, occurs if long wavelength modes are present in the initial perturbation. These will grow exponentially according to linear stability theory, but reach saturation at later times than smaller wavelength modes. At sufficiently late times, long wavelength modes dominate the overall growth of the perturbation, and smaller wavelength perturbations have negligible effect on the large-scale growth of the interface. The second, mode coupling, is the non-linear coupling of saturated short wavelength modes to generate a structure of larger wavelength. In both processes, modal interactions tend to lead to the generation of larger structures in the flow.

In the final stage, various mechanisms cause the breakup of the bubble and spike structures and the development of a large range of scales characterized by small-scale vortices. Thus, the flow-field enters a fully turbulent state. In this regime, it is thought that the flow becomes self-similar and loses memory of its initial perturbation so that the only physical scale remaining is the half-width of the mixing region, $h$

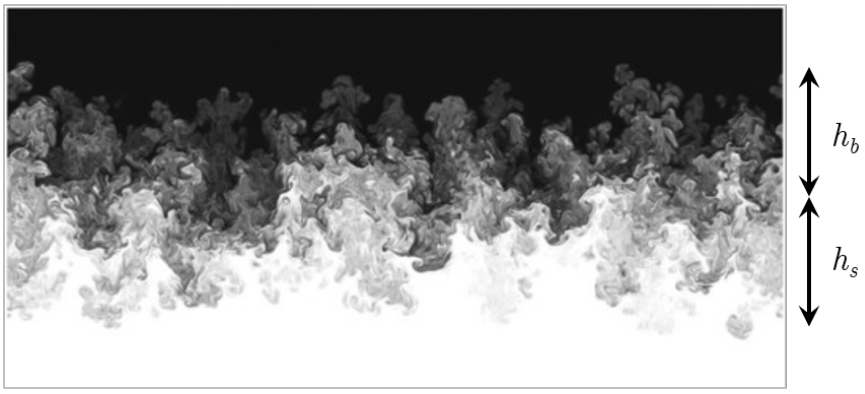


Figure 1.4: Vertical slice of density from a 3D simulation. Overlayed are the mixing widths of the bubble and spike, $h_b$ and $h_s$, measured from the geometric centerline. In a low Atwood number flow, the growth of the bubble and spike are symmetric so that $h_b = h_s = h$.
*Source:* Figure 2, Cabot [33], with permission.

[34]. Early experiments in the fully turbulent regime by Read [35] found that $h$ grew quadratically in time elapsed from the onset of instability, also called the instability development time $t$ by equation 1.7.

$$h = \alpha \mathcal{A} g t^2 \tag{1.7}$$

This quadratic growth rate has been confirmed through a variety of methods. Youngs [36] extended the exponential growth rate of the linear theory, determining that if the dominant wavelength of the flow scales as $h$ that a quadratic growth rate must follow. Anuchina et al. [37] and Cook and Dimotakis [38] found the result through dimensional analysis, assuming that memory of the initial perturbation wavelength is forgotten in the fully turbulent regime. Ristorcelli and Clark [34] applied an ansatz of self-similarity to the Navier-Stokes equations to arrive at a differential equation for $h$, $\dot{h}^2 = 4\alpha \mathcal{A} g h$. The solutions to this equation yield the quadratic growth rate. In addition, a large number of experiments [35, 39–43] and simulations [44–46] have all shown the existence of a quadratic growth rate in the fully turbulent regime. In equation 1.7, $\alpha$ is the RTI growth rate parameter, originally believed to be

a constant. However, experiments and simulations have shown that this parameter can take on a wide range of values from 0.02 to 0.16, depending on the density ratio, acceleration, and initial perturbation [47]. There is also a clear discrepancy between the growth rate found between simulations and experiments, with simulations typically having smaller growth rates. Furthermore, as $\mathcal{A} \to 1$, structural asymmetry develops between the bubble and the spike, causing the bubble growth rate parameter $\alpha_b$ to differ significantly from the spike growth rate parameter $\alpha_s$.

The precise point of mixing transition to the fully turbulent regime is an unanswered question. Dimotakis [49] notes that jet flows exhibit a qualitative transition in phenomenology as their outer scale Reynolds number exceeds a critical value, $\mathrm{Re}_{tr} \approx 1 - 2 \times 10^4$, or as the Taylor Reynolds number exceeds a critical value, $\mathrm{Re}_{\lambda,tr} \approx 100$. He generalized this concept into a hypothesis that other flows also transition to turbulence at a similar Reynolds number. In the case of RTI, the outer scale Reynolds number is most often defined by equation 1.8,

$$\mathrm{Re} = \frac{UL}{\nu} \tag{1.8}$$

where $\nu$ is the kinematic viscosity of the mixture, $L$ is an appropriate length scale for the large scale flow, and $U$ is an appropriate velocity scale. For RTI flows, $L$ is typically chosen to be some multiple of the mixing half-width, $h$. $U$ is typically based either on the growth rate of the mixing width, $\dot{h} = \frac{\partial h}{\partial t}$, or on some measure of the velocity of the turbulence, such as the root mean square velocity fluctuations, $v'_{\mathrm{RMS}}$. Nevertheless, neither the transition criteria presented by Dimotakis [49] nor the appropriate length or velocity scale for the Reynolds number are universally recognized, and the precise dynamics and structure of the fully turbulent regime is still a point of contention.

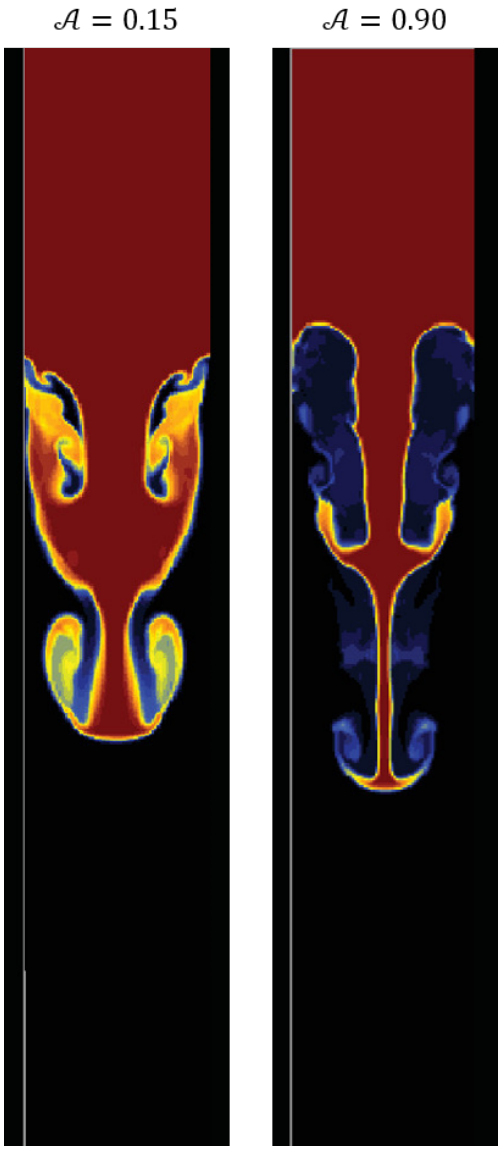


Figure 1.5: RTI simulations performed at Atwood number $\mathcal{A} = 0.15$ and 0.9, showing the asymmetry between the bubble and spike structures that occurs at large $\mathcal{A}$, compared to the symmetry of the Boussinesq instability.
*Source:* Figure 2 and 5, Ramaprabhu et al. [48], with permission.

## 1.3 Experimental History

### 1.3.1 Single-Mode RTI Experiments

The first RTI experiments were interested in single-mode perturbation growth before the fully turbulent regime [25, 50–52].

Most of these experiments were "box-type" or *transient* experiments, in which a stably stratified fluid pair in a rectangular tank was suddenly accelerated. The fluid pair used in these experiments were typically gas-liquid pairs, resulting in $\mathcal{A} \approx 1$. In addition, the presence of surface tension maintained a distinct interface between the fluids, leaving behind a distinct fluid-gas interface that could be easily tracked.

Lewis [25], a collaborator of Taylor, used a compressed air system to suddenly accelerate air towards a stable liquid-gas interface, generating an instability as a result of the artificial acceleration, which was as high as $140g$. $\mathcal{A}$ could be modulated by changing the liquid used. This experiment confirmed the linear stability theory growth rate of Taylor [21] and the transition to the non-linear regime. It also gave an estimate for the bubble velocity in the saturation regime using the same form as that of Davies and Taylor [53], as a fraction of the velocity scale $V_{\text{bubble}} = \sqrt{gR}$, where $R$ is the radius of a rising cylindrical bubble.

Emmons et al. [50], Cole and Tankin [51], and Ratafia [52] performed similar single-mode perturbation experiments, using bungee cables or compressed air to accelerate a stable fluid pair with a single mode interface downward at large accelerations. Emmons et al. [50] noticed that in large wavenumber experiments where there were many small perturbations across the interface that small imperfections in the sizes of different perturbations caused certain bubbles to grow faster than their neighbors and prevent their growth, effectively reducing the number of bubbles as time progressed. This represented the first documentation of competition between bubbles in the non-linear regime. Ratafia [52] was the first to follow the instability beyond the non-linear regime and noted on the development of KHI roll ups on the interface where the bubble and spike sheared past one another.

Despite the importance of these early experiments, they were limited in the quality of single-mode interface produced and the imaging diagnostics available at their time. These obstacles were overcome in 2001 by Waddell et al. [54], who studied the

single-mode 2D RTI by filling a tank with two liquids in a stable configuration and accelerating the tank downwards quickly using a heavy weight accelerator assembly. Through careful selection of the fluid pair, both miscible and immiscible experiments were performed at Atwood numbers between 0.15 and 0.34. By oscillating the tank horizontally at a fixed interval, a precise and symmetric 2D sinusoidal interface between the fluids could be formed before the tank was accelerated. Planar laser induced fluorescence (PLIF) images were captured to visually record the instability growth, which was found to closely match that predicted by linear stability theory (Equation 1.3). Furthermore, in the non-linear saturation regime, the bubbles were found to saturate to the bubble velocity $v_\infty$ predicted by Layzer [26]. Using the same facility as Waddell et al. [54], Wilkinson and Jacobs [55] oscillated a square horizontal cross-section tank around a diagonal axis to generate precise 3D sinusoidal perturbations to compare the growth of the single-mode 2D and 3D RTI at early development times. The results again agreed with linear stability theory, but showed a different saturation bubble velocity that had good agreement with the theoretical work of Goncharov [28].

The single-mode RTI experiments discussed above were used to confirm the growth rate in the linear regime and the subsequent non-linear saturation regime, but could not provide the sustained acceleration required to force the mix into the fully turbulent regime.

### 1.3.2 RTI Experiments in the Fully Turbulent Regime

Read [35] was the first to experimentally study the instability growth in the fully turbulent regime, which he accomplished by accelerating the tank over a long distance using rocket motors. His results were the first to suggest that the late-stage RTI growth was determined by equation 1.7 with a first estimate of $\alpha = 0.07$, as well as the first to suggest the existence of asymmetry in the bubble and spike growth rates

for large $\mathcal{A}$.

In the experiment of Read [35], the acceleration method was not precise enough to provide a constant and easily predictable acceleration, and so the acceleration profile had to be recorded with time and estimated. Dimonte and Schneider [56] solved this problem by using linear electric motors with precise acceleration characteristics. This allowed not just the application of a constant acceleration, but the ability to run experiments with increasing, decreasing, or impulsive acceleration. Later experiments by Dimonte and Schneider [41] performed a wide parametric sweep of $\mathcal{A}$, studying the ratio of asymmetry between the bubble and spike mixing width. The result was an empirical power law for the ratio between the bubble and spike growth rate parameters, $\alpha_s/\alpha_b = (\rho_1/\rho_2)^{0.33}$.

Many other transient RTI experiments have been performed by rapidly accelerating a rectangular tank, mostly collecting information about the density profiles across the mixing region and growth rate information [43, 57, 58]. However, other novel techniques for generating an RTI interface have also been explored. The facility built by Smeeton and Youngs [59] and replicated by Andrews and Spalding [39] considers a tank of narrow width filled with liquids in a stable configuration. A random multimode initial perturbation of small amplitude is applied to the interface, and the tank is quickly overturned. These experiments found the bubble growth rate parameter to be $\alpha_b = 0.06$. However, they were novel in the fact that they represented distinctly 2D RTI flows, where there was an acceleration in a direction both normal and tangential to the perturbed fluid interface. Other transient experiments have been performed by removing a barrier separating the two fluids [40, 60–64]. However, few of these experiments have measured the dynamics of the mixing region, or attained any statistical measures of the characteristics of the developing turbulence.

### 1.3.3 Statistically Steady RTI Experiments

Because any single realization in the fully turbulent regime is chaotic and strongly dependent on initial conditions, the analysis of the regime as a whole requires a statistical approach.

The limitation of transient experiments is that many experimental realizations must be recorded to create an ensemble from which statistics may be collected, sometimes on the order of thousands. Thus, studying the RTI fully turbulent regime using transient experiments requires a prohibitively expensive amount of experimental time.

To overcome this limitation, Snider and Andrews [65] designed a "convective-type" or *statistically steady* experimental facility in which two fluids of different densities flowed parallel to one another separated by a thin splitter plate. The streams met each other as they flowed past the splitter plate and into an optically accessible test section, and RTI developed at the unstable interface between the two streams. The instability continued to grow as the fluids convected across the test section and out of the facility.

At its core, this facility applied Taylor's hypothesis [66] to transform the instability development time, $t$, into the stream-wise distance from the splitter plate, $x$, through the convective velocity $U_c$ by $x = U_c t$, similar to the procedure utilized in grid turbulence experiments [67]. Rather than conducting several experimental realizations to compile a statistical ensemble of RTI structures, a probe or camera was placed at a stationary position in the flow and captured hundreds or thousands of instances of fully turbulent structures as they convected past the measurement location.

The first statistically steady experimental facility built was the water channel facility developed by Snider and Andrews [65]. It used hot and cold water ($\mathcal{A} \approx 1 \times 10^{-3}$), with one fluid marked with nigrosin dye to capture the first measurements of concentration profiles across the mixing height at different measurement times. They also collected measurements of the growth rate parameter, estimating that

$\alpha = 0.07$. Later experiments by Wilson et al. [68] and Wilson and Andrews [69] in the same facility using thermocouple arrays with high temporal resolution allowed the quantification of the power spectrum of density fluctuations, first suggesting the existence of a $-5/3$ power law scaling.

The first velocity measurements in the water channel were collected by Ramaprabhu and Andrews [70], who used particle image velocimetry (PIV) to capture stream-wise and cross-stream velocity fields and statistics. By seeding the top and bottom water streams with different concentrations of PIV particles, an estimate of the stream concentrations could be found, giving a simultaneous density measurement. This experiment was improved in Ramaprabhu and Andrews [71] and showed that velocity profiles collapsed onto self-similar forms at later development times. They also found the existence of a $-3$ power law scaling for the dissipation range using data from a high temporal resolution thermocouple array. Later experiments by Mueschke et al. [72] and Mueschke et al. [73] analyzed the modal content of the initial condition and quantified the effect of Schmidt number on the extent of molecular mixing. In this regard, Mueschke et al. [73] was the first to link RTI back to the fundamental problems of turbulent mixing [49].

To study the RTI fully turbulent regime in the non-Boussinesq regime, Banerjee and Andrews [42] developed a gas tunnel facility analogous to the water channel facility which used air and an air-helium mixture as the two fluids. The concentration of helium in the air-helium mixture could be controlled to alter the Atwood number, and experiments up to $\mathcal{A} = 0.1$ were performed. Backlit fog visualization with a digital imaging technique was used to capture the density profiles across the mixture and hot-wire anemometry was used to capture velocity statistics. Further experiments by Kraft et al. [74], Banerjee et al. [75] developed a multi-position multi-overheat hotwire anemometry method that was able to capture simultaneous velocity-density statistics at Atwood numbers up to $\mathcal{A} = 0.25$. They also developed a hotwire anemometry

method that used a single three-wire probe with a cold-wire temperature probe to capture velocity-density statistics at Atwood number $\mathcal{A} = 0.6$. Results from the gas tunnel facility showed that the RTI mixing layer at large $\mathcal{A}$ was strongly anisotropic with velocity fluctuations in the acceleration direction, $v'$, being approximately twice as strong as in the acceleration normal directions, $u'$ and $w'$. They also elaborated on the extent of asymmetry between the bubble and the spike, finding that the bubble growth rate parameter remained relatively constant with increasing $\mathcal{A}$ at $\alpha_b = 0.05$ while the spike growth rate parameter increased with $\mathcal{A}$ to a maximum of $\alpha_s = 0.085$ at $\mathcal{A} = 0.6$.

### 1.3.4 Modern Experimental Studies of RTI

The current state of RTI research is distinguished by high-resolution and high-speed photography, laser imaging techniques, and extensive data sets providing significant statistical information.

Akula and Ranjan [76] improved upon the design of the gas tunnel facility used by Banerjee and Andrews [42] and Banerjee et al. [75], allowing the measurement of RTI turbulent mixing at $\mathcal{A} = 0.73$. By implementing planar PIV, velocity profiles could be computed across the entire mixing region, and showed the same self-similar collapse that had been previously shown by Ramaprabhu and Andrews [71]. In addition, velocity statistics across the layer showed the same anisotropy present in the experiments of Banerjee et al. [75]. Further work by Akula et al. [77] showed the impact of overlying shear on the growth of the fully turbulent RTI and determined a criteria based on the Richardson number of the flow in order to determine if the growth was dominated by shear or buoyant forces.

Further work on the water channel facility by [78, 79] modified the experimental setup to include a flapping splitter plate, connected to a servo mechanism capable of precisely modulating its motion. This allowed the prescription of specific initial

conditions, including combinations of several sinusoidal modes. Results found that the growth rate of the instability increased with the application of more modes, but that the phase angles of the superimposed modes had virtually no impact on the turbulent characteristics of the flow in the fully turbulent regime. The phase angle did have influence on the bubble and spike structures generated, causing them to lean preferentially in the direction of the phase shift.

Lawrie and Dalziel [80] and Davies Wykes and Dalziel [81] developed a novel filling technique for the tank with removable barrier first developed by Linden and Redondo [60]. By precisely adding in fluids of different salinity, a varying stable density profile could be applied to the top and bottom streams, resulting in an RTI setup that reaches a stable equilibrium after some mixing time. The mixing efficiency between the two streams was studied and found to reach an asymptote of 0.5. The RTI growth rate parameter for the bubble was found to be around $\alpha_b = 0.07$.

Charonko and Prestridge [82] studied the effect of RTI on a turbulent jet of heavy fluid coflowing with a light fluid. By coupling PIV with planar laser induced fluorescence (PLIF), the combined velocity-density statistics in an entire field could be captured. This information was used to compute the budgets of production, transport, advection, and dissipation in the turbulent kinetic energy equation across the jet mixing layer.

Morgan et al. [83] developed a novel facility in which a three-dimensional single-mode interface was accelerated by a rarefaction wave, and used high-speed photography to capture the evolution of the interface. Experimental results were compared to simulations and found good agreement between predicted growth rates and experimental growth rates. However, they were also able to show that no clear transition to a fully turbulent regime was achieved, even as the outer scale Reynolds number exceeded $1 \times 10^4$.

In seeking to develop an RTI experiment which had volumetric radiation deposi-

tion analogous to that experienced by the ICF capsule, Wachtor et al. [84] created an RTI setup in which two liquids originally sit in a small chamber in a stable configuration. The bottom fluid is rapidly irradiated with a strong microwave field which changes the fluid density to being lighter than the top fluid, initiating the instability. A model was used to predict the variation in density due to volumetric energy deposition. As a result of the time-variable Atwood number in this experiment, the authors proposed that the mixing layer width will grow faster in the presence of volumetric energy deposition, and showed through theory and experimental results that $h \sim t^3$ instead of the typical $h \sim t^2$ typically observed in the RTI self-similar regime.

To study the impact of Coriolis effects on the growth of RTI, Baldwin et al. [85] built a facility in which a cylindrical tank containing a fluid pair in a stable configuration was moved into a magnetic field. The lighter top fluid was selected to be paramagnetic and the heavier bottom fluid was selected to be diamagnetic, such that the magnetic field applied a body force in both fluids towards the interface, changing the effective density gradient and Atwood number of the interface and starting the RTI growth of perturbations. The tank could be rotated along an axis normal to the interface, and the effect of the rotation on the growth rate could be measured. It was found that rotation served to slow the RTI growth rate and stabilize long wavelength perturbations, resulting in finer interfacial structures.

## 1.4 RTI Modeling

Most RTI phenomena develop past the linear regime and into the non-linear and turbulent regimes. Linear stability analysis is inadequate in these regimes, so there is a need to develop analysis techniques to predict the later time instability development. Furthermore, while the physics of the flow are entirely defined by the Navier-Stokes equations, there are many obstacles making numerical computation impractical for many applications. For one, many applications involve a large spectrum of scales

that make the numerical resolution infeasible to achieve. In most cases, it is unrealistic to simulate to the large Reynolds numbers associated with the flow while also completing the calculation in a reasonable turnaround time sufficient to make engineering decisions. In most practical applications, there are also added layers of complex physics that exacerbate the computational costs of numerical computation. In the case of ICF capsule design and Type Ia supernovae analysis, one must contend with compressibility, variable acceleration/gravity, high-energy-density, and magnetohydrodynamics. For these reasons, most attempts to develop predictive tools to analyze late stage RTI have focused on modeling the instability.

### 1.4.1 Modeling of the non-linear regime

The earliest attempts to model the non-linear regime applied potential flow analysis to a single-mode perturbation to predict the growth of a single bubble structure into late time. This technique was pioneered by Layzer [26], who solved the potential flow equations in the vicinity of the bubble tip for the case of $\mathcal{A} = 1$. The technique was applied in both 2D, considering solutions of a single wavelength bubble in the plane (Fourier modes) and in 3D, considering an axisymmetric bubble in a cylinder (Bessel modes). The analysis showed that the bubbles reached an asymptotic velocity, termed the bubble velocity $v_\infty$, which differed between 2D and 3D and were dependent on the gravitational acceleration and the size of the bubble. These results were consistent with the experimental bubble velocity found by Davies and Taylor [53] and with the numerical solution of Birkhoff and Carter [27].

Zufiria [86] extended the work of Layzer [26] by allowing the bubble size to change, making it possible to analyze a train of bubbles each with different initial size. This technique was used to study how bubble competition would result in the destruction of small bubbles, as larger neighbors fed on their velocity. The resulting single-mode bubble velocity matched that of Layzer [26], while the multi-mode random initial

perturbation resulted in a quadratic bubble growth rate similar to the expectation in the self-similar regime. The bubble growth rate parameter $\alpha_b$ was found to be between 0.03 and 0.04.

Goncharov [28] modified the theory of Layzer [26] to allow arbitrary Atwood number $\mathcal{A}$. This was accomplished by solving a potential flow equation for both the light and heavy fluid simultaneously, rather than for just the heavy fluid. By decomposing the velocity potentials into single-mode Fourier or Bessel functions, an evolution system involving five ordinary differential equations can be solved numerically. Goncharov [28] found that the bubble velocity saturates at late time to

$$v_\infty = \begin{cases} \sqrt{\dfrac{2\mathcal{A}g}{1+\mathcal{A}}\dfrac{1}{\kappa}} & : \text{2D} \\ \\ \sqrt{\dfrac{2\mathcal{A}g}{1+\mathcal{A}}\dfrac{1}{3\kappa}} & : \text{3D} \end{cases} \tag{1.9}$$

Where $\kappa$ is the single-mode perturbation wavenumber, given as

$$\kappa = \begin{cases} \dfrac{2\pi}{\lambda} & : \text{2D} \\ \\ \dfrac{2\beta_1}{D} & : \text{3D} \end{cases} \tag{1.10}$$

where $\lambda$ is the 2D bubble width, $D$ is the 3D bubble diameter, and $\beta_1 \approx 3.8317$ is the first zero of the first-order Bessel function.

All of the above potential flow models assume that the shape of the fluid interface is single-valued. However, in the third regime of the RTI phenomenology, vortical motion at the location where the bubble and spike shear past each other cause KHI roll-ups and the interface geometry becomes more complex. This leads to a loss of accuracy of these models. Furthermore, the potential flow models solve the velocity potentials numerically in the vicinity of the bubble tip. They predict the spike growth poorly as a result, especially as $\mathcal{A} \to 0$. Lastly, these models do nothing to predict

how entrainment, dispersion, and diffusion might result in molecular mixing of the two fluids. These shortcomings prevent the accurate prediction of the RTI development into the self-similar fully turbulent regime.

### 1.4.2 *RANS*-type models

The most common models for the fully turbulent regime in the early days of RTI research were buoyancy-drag models. Some examples of these models can be found in Dimonte and Schneider [41], Baker and Freeman [87], Oron et al. [88]. These models assume that the acceleration of the bubble front can be computed as a force balance of the buoyancy forces and drag forces on the bubble. The simple nature of these models allowed them to easily be modified to consider 1D cylindrical or spherical geometries, converging geometries, or the addition of ICF or supernovae physics. This has allowed their use for practical engineering applications [89, 90]. However, these models do not handle turbulence directly [91], and can have limitations in expansion to 2D and 3D geometries, or scenarios involving multiple interfaces or de-mixing [92].

In practice, Reynolds-averaged Navier-Stokes (RANS) models are the models most developed by the RTI community and most used for engineering analysis of RTI in the fully turbulent regime. A RANS model operates by splitting the ensemble-variable quantities of the flow into a mean and fluctuating component, substituting the split components into the Navier-Stokes equations, and performing an ensemble average on the equations. For single-component and incompressible flows, a Reynolds decomposition is applied so that any ensemble-variable quantity $f$ is decomposed as

$$f = \overline{f} + f' \tag{1.11}$$

with mean component $\overline{f}$ and fluctuating component $f'$. Here, the overline represents an ensemble average of the quantity in question. Because RTI flows include fluids of

varying density, a Favre decomposition [93] is typically used instead (Equation 1.12).

$$f = \tilde{f} + f'' \tag{1.12}$$

where $\tilde{f} = \overline{\rho f}/\overline{\rho}$. The application of Reynolds averaging results in second-order and higher correlations of the fluctuating terms, such as the Favre-averaged Reynolds stress $\tilde{R_{ij}} = \overline{\rho u_i'' u_j''}$. The attempt to satisfy these correlations in terms of the mean components is the closure problem of turbulence.

Two-equation models are some of the most used RANS closure models. These add evolution equations for the turbulent kinetic energy per unit mass, $k$ and one other variable, which is typically either a turbulent length scale $L$ [94] or the turbulent dissipation per unit mass $\epsilon$ [95]. These models contain a variety of model coefficients which must be set correctly in order to accurately predict real-world physics. A version of the $k-L$ model was developed by Dimonte and Tipton [96] with a corrected $k$ source term for variable-density flows. Model coefficients were found by assuming a self-similar RTI growth with bubble growth rate parameter $\alpha_b = 0.06$. Kokkinakis et al. [92] compared the performance of this model to implicit large eddy simulations performed by Youngs [97] at two different Atwood numbers and found good overall agreement after some modifications. $k-L$ models have also been used for the analysis of astrophysical flows [98] and ICF ablation targets [99, 100]. Despite successes, these two-equation models have inherent limitations. Most importantly, they treat the underlying turbulence as isotropic, whereas variable density instability flows are inhomogeneous and anisotropic. This causes inaccuracy at early instability times and at the interface of the mixing region [91].

### 1.4.3 The BHR model

On the surface, the model of Besnard, Harlow, and Rauenzhan (BHR) [101] is comparable to most standard RANS turbulence models. First, a Favre average of the

Navier-Stokes equations is performed, and equations for the higher-order correlation terms must be closed. The major achievement of this work is the recognition that most flows of interfacial instabilities are unsteady and multi-material. This requires that evolution equations be included for all second-order correlations [102].

The resulting model outlined in Besnard et al. [101] includes evolution equations for the Favre-averaged Reynolds stress, the turbulent length scale, turbulent mass flux, and density-specific volume correlation. The turbulent mass flux $a_i$ is defined as

$$a_i = \frac{\overline{\rho' u_i'}}{\overline{\rho}} \tag{1.13}$$

and the density-specific volume correlation $b$ as

$$b = -\overline{\rho' \left(\frac{1}{\rho}\right)'}. \tag{1.14}$$

Both of these terms have strong impact on the development of the flow, especially at Atwood number unity, and their experimental measurement is vital for the setting of BHR model coefficients.

Several national laboratories and organizations have implemented versions of the BHR model into in-house computer codes designed to simulate the hydrodynamics of ICF or astrophysical conditions, commonly called hydrocodes. As the use of the BHR model has evolved, certain naming conventions have been risen to differentiate the specific set of model equations and coefficients used from other iterations of the basic model.

BHR1 refers to the model first implemented on the Los Alamos National Laboratory (LANL) radiation adaptive grid Eulerian (RAGE) hydrocode [103]. In addition to the Favre-averaged Navier-Stokes equations, BHR1 includes evolution equations for $k$, $L$, and $a_i$. Instead of an evolution equation for $b$, an algebraic equation is used as an approximation. In some sense, BHR1 was a natural iteration to the widely

used $k - L$ turbulence models. Banerjee et al. [104] formulated a methodology for application of BHR1 to variable-density flows like fully turbulent RTI. By assuming approximate self-similar profiles and integrating the evolution equations across the mixing region, it was possible to find equations for the model constants in terms of the peak profile values obtained from experiments. The model coefficients were computed using the $\mathcal{A} = 0.04$ RTI experiments by Banerjee et al. [75], and RAGE computations using the model were compared with some canonical RTI, KHI, and Richtmyer-Meshkov instability (RMI) experiments and numerical simulations.

The next iteration of BHR in the LANL RAGE hydrocode was termed BHR2 and included an evolution equation for $b$ instead of an algebraic equation [105]. This fixed an issue in the BHR1 model that caused it to perform poorly in evaluating the turbulent kinetic energy and turbulent mass flux in homogenous variable-density turbulence. Another LANL hydrocode, FLAG, also implemented the BHR2 model [106], and used the same canonical test cases as Banerjee et al. [104] to set the model coefficients. Furthermore, Denissen et al. [107] showed that the BHR2 implementation in FLAG could accurately predict the results of the "Tilted-Rig" experiments of Smeeton and Youngs [59], a novel RTI experiment that is notably 2D. This was specifically important because of the previous failure of the buoyancy-drag models and two-equation RANS models in 2D variable-density turbulence analysis.

The first BHR implementation to include all of the evolution equations outlined by Besnard et al. [101] was performed by Schwarzkopf et al. [108] in LANL RAGE and called BHR3. In addition to the transport equations in BHR2, BHR3 included evolution equations for the Favre-averaged Reynolds stress terms $\tilde{R}_{ij}$. The inclusion of the Reynolds stress transport equations allowed for the anisotropy of the Reynolds stress to finally be accounted for, giving the model better behavior at near-interface conditions. Comparisons to both RTI and RMI experiments showed that BHR3 was capable of capturing the Reynolds stress anisotropy.

In comparisons with homogenous RTI numerical simulations at $\mathcal{A} = 0.25$, Schwarzkopf et al. [109] found that BHR3 grossly overestimated the turbulent statistics, even though the model correctly estimated the large scale mixing region growth rates. Upon inspection, it was realized that these errors came from using the length scale associated with turbulent transport to also describe the turbulent dissipation. To satisfy this problem, the authors developed the BHR two-length-scale model (TLSM). This model provided one length scale that described the large scale transport of turbulence, $L_T$, and another that described the decay rate of the turbulence, $L_D$. Transport equations for both length scales were included, and occurrences of the turbulent length scale $L$ in the other transport equations were replaced with either $L_T$ or $L_D$ as appropriate. The model coefficients for BHR TLSM were found by comparing to an array of RTI, KHI, and RMI experiments and simulations. The $\mathcal{A} = 0.5$ numerical simulation of Cabot and Cook [110] was the specific RTI simulation used for fitting the model coefficients for turbulent diffusion. However, there are still opportunities to see how the BHR TLSM performs in comparison to other Rayleigh-Taylor instability experiments in the turbulent regime.

## 1.5 Objectives

According to the framework of Dimotakis [49], RTI constitutes a "Level-2" mixing process in which the dynamics of the flow are affected by the mixing. As such, the proper experimental study of RTI requires the understanding of both the mixing and the dynamics, through the measurement of the density field and the velocity field simultaneously. As seen is Section 1.3, there have been a large number of RTI experiments which have studied the dynamics or the mixing, but few that have measured the two simultaneously. Among statistically stationary experiments, Ramaprabhu and Andrews [70] were the first to measure simultaneous density-velocity statistics using a technique called PIV-S in which PIV particles were seeded in different con-

centrations into the two streams of the flow. By averaging the intensity of the PIV particle scattering over a window, an estimate for the particle concentration, and thus the stream concentration could be found. However, these experiments were limited to very low Atwood number, $\mathcal{A} \approx 1 \times 10^{-3}$ and suffered from poor accuracy and resolution near the mixing interface. Kraft et al. [74] and Banerjee et al. [75] developed and tested a multi-position multi-overheat hotwire technique that was able to measure time-averaged density-velocity statistics at a point for Atwood number as large as $\mathcal{A} = 0.25$. They also developed a simultaneous cold-wire three-wire (SCW3W) technique which could be used to obtain density-velocity statistics for a flow in which the temperature of one of the streams was elevated. Akula and Ranjan [76] developed the SCW3W technique further and also incorporated an X-wire probe consisting of one thin wire and one thin film that could be used to measure the density of the flow directly. However, all of these hotwire techniques were limited to measurement at a single spatial location. Considering these past limitations and the wealth of information to be gained on RTI mixing through the simultaneous measurement of density and velocity, this work sets out to complete the following objectives:

1. **Capture simultaneous density-velocity field measurements of a statistically stationary Rayleigh-Taylor instability experiment using a combined particle image velocimetry (PIV) and laser induced fluorescence (LIF) technique.**

   The PIV and LIF diagnostics are developed as described in Section 2.2, while the specific RTI experiments to be performed are outlined in Section 3.1. From the PIV measurements, statistics of the velocity field can be found, including quantities describing the probability density functions of the fluctuating velocity components. By taking measurements at multiple Reynolds number, the hypothesis of self-similar collapse can be tested by applying an appropriate normalization factor to the velocity profiles. The RTI growth rate parameter, $\alpha$,

may also be computed from knowledge of the maximum velocity fluctuations. From the LIF measurements, the growth of the mixing height, $h$, and the growth rate parameter can be found.

Finally, for the first time, the combination of PIV and LIF simultaneously will provide field measurements of cross-correlations of density and velocity in a statistically stationary RTI flow. In adddition, measurements of the turbulent kinetic energy and Reynolds stresses can be collected. The sign of density and velocity fluctuations can be used to separate the relative impact of the bubble and spike and perform conditional sampling of the collected data.

2. **Examine measures of molecular mixing and describe the processes which lead to its evolution.**

   Both Type Ia supernovae and the ICF capsule implosion represent instances of a miscible Rayleigh-Taylor instability flow. As a result, the molecular mixing which occurs as a response to the bulk motion induced by the instability is important to understand. To quantify the molecular mixing, we find profiles of the degree of desegregation between the fluids, also called the molecular mixing parameter. Beyond just the quantification of mixing, the rate of mixing is also found through measurements of the scalar dissipation.

   The density-specific-volume correlation, $b$, is another important measure of mixing in variable density flows. Profiles of $b$ are presented, and an appropriate scale for $b$ across the mixing region is tested. The transport equation of $b$ is analyzed, and the relative importance of production, transport, and convection towards the evolution of the mixing field is examined.

3. **Quantify the transfer of energy in Rayleigh-Taylor instability flows.**

   One way of interpreting the growth of the RTI is to recognize it as an energy transfer process. Gravitational potential energy in the form of an inverted

density profile is released and converted into kinetic energy. Through the second law of thermodynamics, some energy is lost as heat through viscous dissipation during this conversion. It is traditionally understood that this dissipation begins to work at scales smaller than the Taylor microscale, $\lambda$. In this work, we present measures of the release of potential energy and growth of turbulent kinetic energy of the flow, as well as the overall dissipation in the flow. By computing the production, transport, and advection terms of the transport equation of $k$, the relative importance of these terms is determined. Estimates of the Taylor microscale using the velocity fluctuation gradient method are also found. Two measures of the energy dissipation are presented and compared.

# CHAPTER 2
# EXPERIMENTAL METHODOLOGY

## 2.1 Experimental Facility

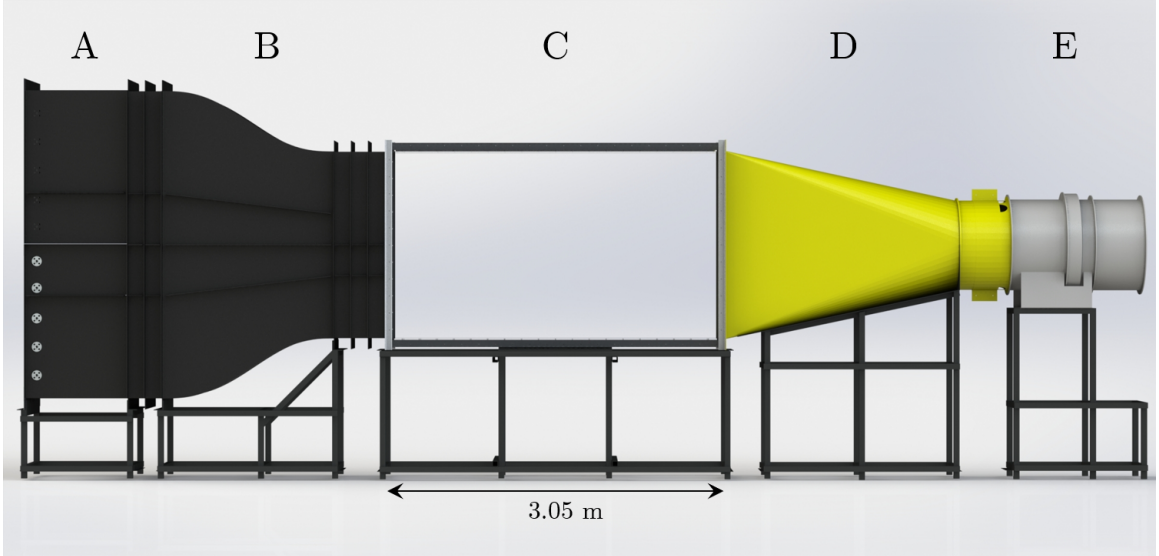


Figure 2.1: 3D render of the gas tunnel facility.

Experiments are performed in the gas tunnel facility, illustrated in Figure 2.1. The base of the facility is that used by Akula and Ranjan [76], but has been modified to capture combined density-velocity statistics using simultaneous PIV/LIF. Two fluid streams, one heavy and one light, flow separately through the tunnel operated by a suction fan. They remain separated until they pass the splitter plate dividing them and enter the test section, where they begin to mix with one another. They continue to mix as they convect across the test section. The major benefit of the gas tunnel facility is that it is statistically steady – at any location in the flow, time gradients of mean quantities are zero [65]. In this convective-type facility, Taylor's hypothesis [66] is used to transform the development time of the instability, $t$, to the stream-wise location, $x$, through the convective velocity, $U$, by $x = Ut$. As a result, higher

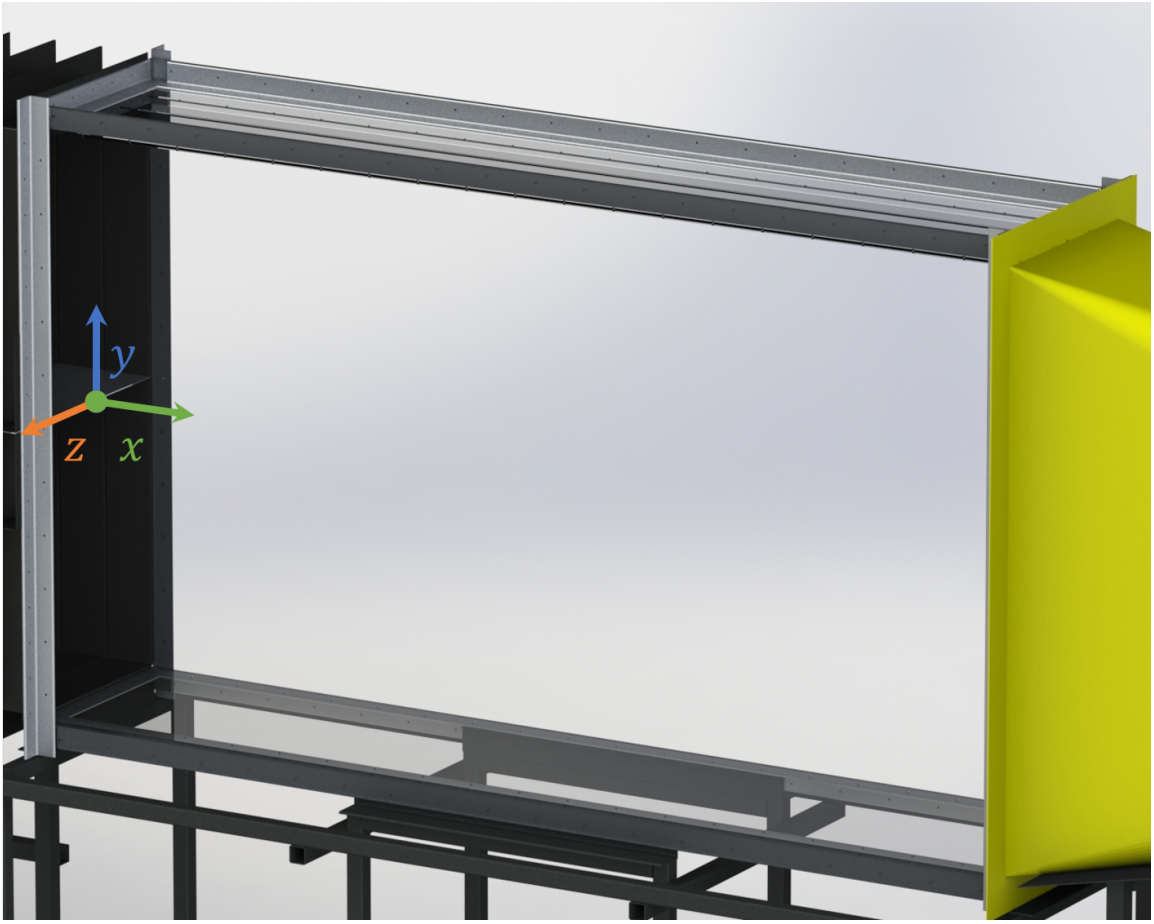


Figure 2.2: Coordinate system of the gas tunnel. $x$, $y$, and $z$ represent the stream-wise, cross-stream, and span-wise directions with respect to the flow, respectively. To illustrate the splitter plate location, the wire mesh grid has not been shown.

order moments, probability density functions, structure functions, and spectra can be measured at specific RTI mixing times by recording measurements at a single stream-wise location for a long period of time.

Being the section of primary interest, the origin of the system is defined as the center of the splitter plate knife-edge, where the fluids begin to mix with one another. The resulting coordinate system is illustrated in Figure 2.2. $x$ refers to the streamwise coordinate of the flow, $y$ to the cross-stream coordinate, and $z$ to the spanwise coordinate. This coordinate system allows Taylor's hypothesis to be used to transform the streamwise coordinate into the instability development time without any need for a coordinate offset.

For both fluid streams, air is drawn into the settling section (A) through a set of sliding grates in the back of the tunnel. A close-up of the grates is shown in Figure 2.3. By opening and closing the grates, the major pressure loss across each stream can be controlled and the velocity of each fluid stream may be changed. The heavy gas stream is composed primarily of air drawn in through the grates. The light gas stream is mostly a helium/nitrogen mixture, injected into the flow through the side port and uniformly diffused into the settling chamber through fine pore tube diffusers. Details about the light gas injection system can be found in Section 2.1.1.

In order to mix the light injected gas with the drawn air and PIV particles, eight 22 cm diameter fans are placed in the settling section. Figure 2.3 shows the arrangement and orientation of the fans. The injected gas first interacts with an array of four fans, oriented downwards, and placed in a $2 \times 2$ vertical grid. The other four fans are placed 45 cm downstream of the first array in a similar $2 \times 2$ vertical grid configuration, but pointing upwards. A combined PIV-LIF experiment in a shear case found that the fans had small influence on the turbulence intensity and mean velocity, but that their addition greatly improved the homogeneity of both acetone vapor and injected light fluid in the light gas stream. The velocity and concentration profiles are shown in Figure 2.4. By looking at the root-mean-square fluctuation of the concentration in the bottom stream, the addition of the fans reduced fluctuation in some locations by a factor of 8.

As the gases exit the settling section, they flow through a plastic honeycomb core formed of 6.35 mm diameter and 15.2 cm length straws packed in a hexagonal pattern which serve to mitigate the turbulent fluctuations caused by the injection and mixing processes. The gases enter the contraction section (B), which changes the cross-sectional area from 0.91 m $\times$ 1.37 m to 0.61 m $\times$ 0.83 m over a distance of 2.1 m, representing an area ratio of 2.5. This area ratio is smaller than that typically used for plane mixing layer experiments, but has not hugely influenced any conclusions being

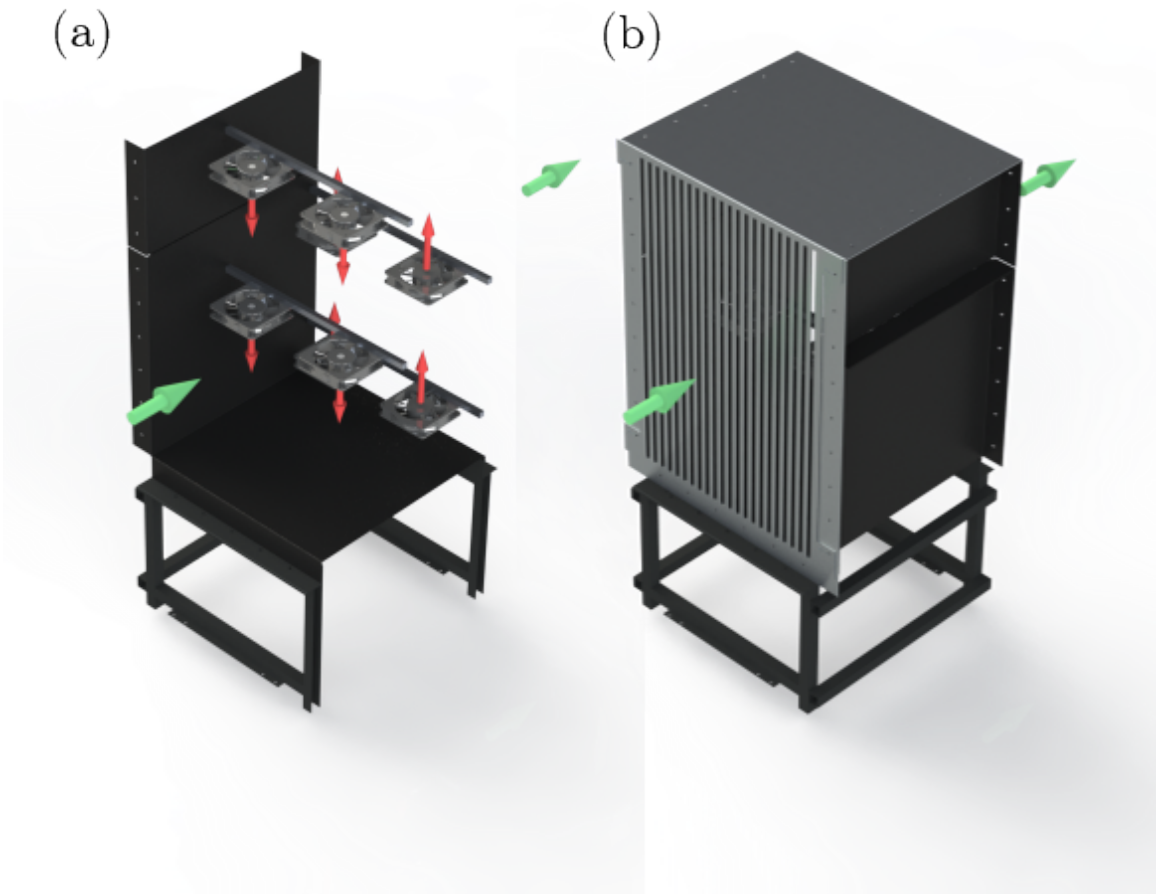


Figure 2.3: 3D renderings of the bottom half of the gas tunnel facility settling section. Green arrows represent the flow direction of gas into and out of the settling section. The gas injection and PIV injection setup have been removed for clarity. (a) A model illustrating the arrangement and orientation of mixing fans and support beams in the settling section, with red arrows representing the flow direction of each fan. (b) A model illustrating the sliding grates that can be used to increase the major pressure losses in the bottom stream.

drawn in the current work. A fifth-order polynomial ($Y = 6X^5 - 15X^4 + 10X^3$) is chosen for the contraction shape in the $y$ direction [111], while the reduction in the $z$ direction is linear. Following the contraction section, the gases pass through another plastic honeycomb core of identical geometric properties to the one in the settling section. Finally, the gases pass over the splitter plate, which has been ground down

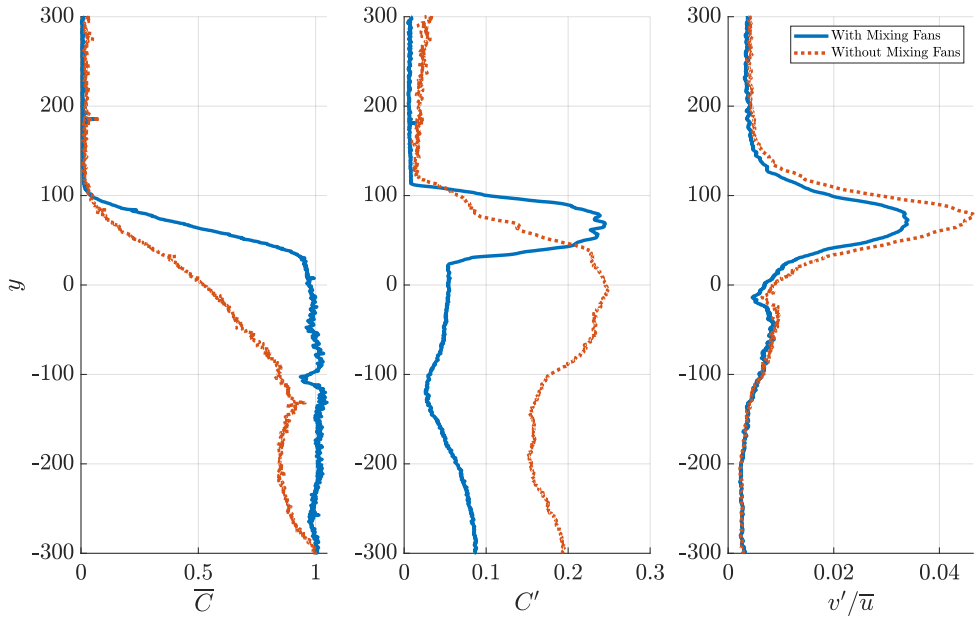


Figure 2.4: The impact of the addition of the mixing fans on the mean concentration profile $\overline{C}$, fluctuating concentration profile $C'$, and normalized fluctuating vertical velocity profile $v'/\overline{u}$. Measurements are taken at the $x = 1.25\,\text{m}$ location.

to a knife-edge to reduce the size of wakes off the trailing edge. After flowing over the knife-edge, the gases pass a mesh grid that conditions the turbulent characteristics of the flow. The mesh is composed of a grid of 0.58 mm diameter steel wire spaced 2.11 mm apart for an open area ratio of 52%. At the speeds present in the tunnel, the grid Reynolds number is approximately 90 and the pressure reduction factor is approximately 1.40 [112]. The wire diameter was selected to ensure the structural strength of the mesh material, so that it would not warp or deform when installed into the tunnel. Based on the properties of mesh generated turbulence described in literature, we expect that the mesh results in a 35% reduction in incoming free stream turbulence [113] and imparts turbulence with an integral scale on the order of the mesh wire diameter [112].

It is in the test section of the facility (C) that mixing between the streams begins and measurements are taken. The test section is made of 1.27 cm thick acrylic windows to create a rectangular prism 3.05 m long by 0.61 m wide by 1.67 m tall. The

entire section is supported using 7.6 cm wide aluminum angle irons to reinforce the structure and prevent flexing or tilting. The acrylic walls afford optical access, with acrylic having greater than 80% transmission in the visible wavelength. However, the acrylic walls also have less than 20% transmission at UV frequencies, which is the frequency of light necessary for LIF excitation. To solve this issue, a 1.9 cm wide and 2.7 m long slot is cut from the top of the test section, with the center of the slot at $z = 0$, and extending from $x = 0.15$ m to 2.89 m. A 1.9 cm by 30 cm UV fused silica window is machined to be placed at any location within the slot, and the remaining slot area is plugged by applying tape to the interior surface of the test section. UV fused silica has $\approx 92\%$ transmission at 266 nm, which is the excitation frequency used for LIF.

The fluid streams continue to mix until they convect out of the test section. Upon exiting the test section, flow enters the square-to-round exit section (D), which is fitted with an entrance door to allow easy access to the inside of the tunnel. The exit section transitions the flow from a 0.61 m wide by 1.67 m tall rectangular cross-section area to a 0.8 m diameter circular cross-section over a length of 2.74 m, resulting in a contraction angle of 9°. The exit duct of the exit section contains another plastic honeycomb core to prevent the upstream propagation of swirl effects from the fan. Finally, flow exits the facility through a 0.8 m diameter AeroVent variable pitch fan (E) with a motor controlled by a variable frequency drive. The fan is driven in a suction configuration and is capable of producing test section convective speeds up to $20\,\mathrm{m\,s^{-1}}$. By controlling both the rotational speed and fan blade pitch, we are able to control not only the convective speed, but also the free stream turbulence of the flow.

### 2.1.1 Light Gas Injection System

The density difference between the two fluid streams is achieved by injecting a "lighter-than-air" gas mixture into the bottom stream of the gas tunnel facility. In order to maintain a constant Atwood number during the experiment, it is necessary to precisely control the mass flow rate of the injected fluid. This is accomplished with the light gas injection system, modeled in Figure 2.5.

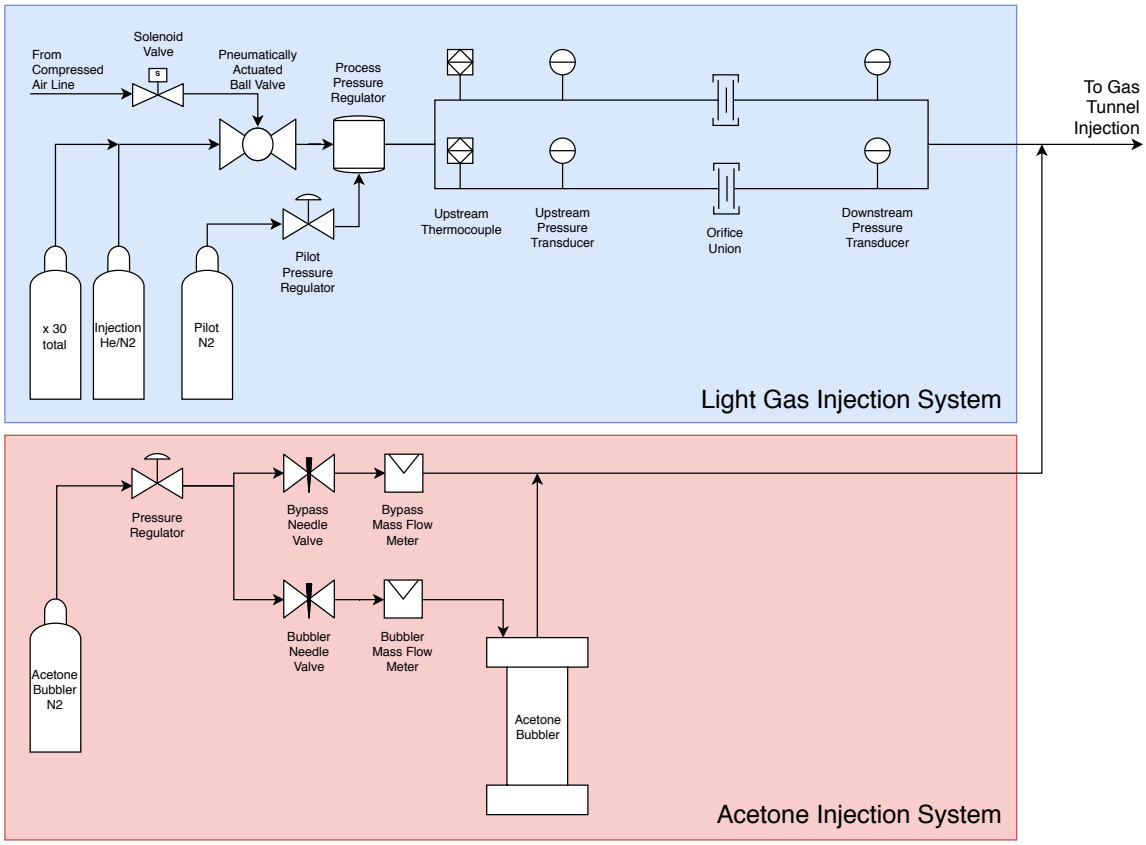


Figure 2.5: A schematic of the light gas injection system and acetone bubbler system before injection into the gas tunnel.

The light gas injection system begins with an array of thirty 300 size gas cylinders. The cylinders arrive at the facility with a mean gauge pressure of 18 MPa, and it is this high pressure which drives the system, with no need for compressors or pumps to drive the gas injection. Cylinders are either filled with industrial grade helium or nitrogen gas, and by changing the number of cylinders of each, the density of the

injected fluid stream can be controlled. A hose manifold connects all thirty bottles to a single gas line of 1.9 cm tube. Upon exiting the hose manifold, the gas first flows through a pneumatically actuated ball valve which is used to start and stop the gas injection process. The ball valve has a flow coefficient of $C_v = 13$ to minimize the pressure drop of the flow, and is actuated by a smaller solenoid valve connected to a compressed air line. This allows the ball valve to be opened by a digital computer pulse, with an opening time of approximately 1.7 s.

Once the ball valve is opened, the first device the light gas flows into is a Tescom 26-1221-2121 pressure regulator which serves as the process pressure regulator. This high-pressure high-flowrate regulator has $C_v = 3.3$ and is capable of controlling the downstream pressure of the regulator to between 1.3 and 4.1 MPa until the upstream pressure drops below 4.8 MPa. The low upstream pressure requirement is vital to the economical operation of the experiment. Because the light gas injection system is only driven by the pressure of the incoming cylinders, once the cylinder pressure drops below the upstream pressure requirement, it is no longer possible to set the correct pressure downstream of the regulator. Therefore, the smaller the upstream pressure requirement, the longer the experiment can run, and the larger the data set that can be acquired. The process pressure regulator is dome-loaded and piloted by a Tescom 26-2066D24S272 pilot pressure regulator which is used to set the overall pressure for the process. The pilot regulator is pressurized from a separate pilot nitrogen tank.

Following the flow through the pressure regulator, the light gas is diverted into two identical critical orifice subsystems. Each subsystem is composed of an orifice union of 2.54 cm diameter that clamps an orifice plate that has orifice size 0.72 cm and a thickness of 1.45 cm. Cunningham [114] explains that square edged orifices have unpredictable characteristics when the thickness of the orifice is less than two orifice diameters thick. The ratio of orifice thickness to diameter for the current setup is approximately 2, resulting in an orifice discharge coefficient of $C_D = 0.84$.

20 pipe diameters upstream of the orifice, the pipe is teed off with an Omega PX309 pressure transducer and 3.2 mm diameter K-type thermocouple which measure the upstream pressure and temperature of the flow entering the orifice. Likewise, 10 pipe diameters downstream of the orifice, another pressure transducer measures the downstream pressure. The pressure transducers have an operating range from 0 to 6.9 MPa with an accuracy of $\pm 1\%$ of the measurement, while the thermocouples have an accuracy of $\pm 1.5\,^{\circ}\mathrm{C}$. Based on the geometry of the pipe and orifice, the Mach number at the measurement location is approximately 0.03, meaning that the static pressure measurement at this location deviates by less than 0.1% from the total pressure measurement. The diameter of the orifice was specifically chosen to achieve this Mach number, since at larger Mach numbers, the deviation between static and total pressure measurements would have been too large, and at lower Mach numbers, the flow rate desired would have required a larger overall pipe diameter, increasing material costs and exceeding space constraints. This is also the reason why the flow was passed through two smaller orifices, rather than in a single larger orifice. The final equation determining the mass flow rate through the orifice is Equation 2.1

$$\dot{m} = C_D \rho_{th} a_{th} A_{th} \tag{2.1}$$

Where $C_D$ is the orifice discharge coefficient, $\rho_{th}$ is the density of the light gas at the orifice throat, $a_{th}$ is the sound speed through the orifice throat, and $A_{th}$ is the orifice area. Both $\rho_{th}$ and $a_{th}$ can be determined from the upstream temperature and pressure measurements and the isentropic nozzle flow assumptions. Overall, the pressure and temperature upstream of the orifice are the determining factors in setting the mass flow rate through the orifice and the resulting light gas injection rate into the bottom stream. Therefore, the accurate setting and monitoring of these quantities, along with careful measurement of the geometry of the orifice, is necessary for computing

the mass flow rate.

After flowing through the critical orifice subsystem, the gas streams are reconverged and the acetone injection line is teed in. This allows the acetone to thoroughly mix with the injected gas before entering the bottom stream. The design and details of the acetone bubbler were a significant engineering challenge, and are discussed separately in Section 2.2.3. The acetone is injected roughly 40 pipe diameters before it is injected into the tunnel. Finally, a 5 cm flange adapter is used to interface the light gas metering lines with the distribution manifold inside the wind tunnel.

The light gas distribution manifold is an array of nine 7.6 cm diameter, 61 cm long fine pore tube diffusers. These diffusers consist of a plastic pipe wrapped along the diameter with a rubber sheath that has been perforated with small holes. The large pressure drop coefficient for each of the small holes helps to reduce velocity fluctuations between different holes, resulting in a highly uniform gas injection, even if there are significant deviations in differential pressure across the holes. In general, these devices are not rated for the flow rates required for the current setup. To verify that they would work appropriately, a validation test was performed in which a single one of these diffusers was attached to a mass flow controller and a pressurized air line. It was found that the pressure drop necessary to achieve the desired flow rate was 410 kPa, and that the application of this pressure did not destroy the diffuser.

To correctly measure the density of the top and bottom streams, two more K-type thermocouples of 3.2 mm diameter are placed in the flow streams immediately after the converging section and before the test section. By assuming the pressure of the gas is near atmospheric pressure, we can calculate the density of the gas based solely on the temperature and the concentration of injected gas. The densities can then be used to calculate the Atwood number of the experiment over time.

All of the pressure and temperature measurements that occur during an experiment are captured at a rate of 20 Hz by a National Instruments LabVIEW virtual

instrument that controls several National Instruments data acquisition modules. The thermocouple measurements are captured by an NI-9210 temperature input module and the pressure transducer voltages are captured by an NI-9201 voltage input module.

## 2.2 Diagnostics

### 2.2.1 Scales for Imaging Diagnostics

Before considering the temporal and spatial resolution of our imaging techniques, it is imperative that we understand the length scales and time scales present in the flow. The results of Akula and Ranjan [76] help to provide first order estimates of these values. The outer scale of the flow, $L$, is on the order of the half mixing height, $h = 0.2\,\mathrm{m}$, and the fluctuating velocity scale is on the order of the total mixing height growth rate. To estimate this, we take the time derivative of the RTI self similar growth rate, Equation 1.7, to find that $\dot{h} = 2\alpha\mathcal{A}gt = \sqrt{4\alpha\mathcal{A}gh}$. With estimates of the growth rates, Atwood number, and gravitational acceleration of $\alpha = 0.06$, $\mathcal{A} = 0.1$, and $g = 9.8\,\mathrm{m\,s^{-2}}$, respectively, we arrive at an estimate for the growth rate as $\dot{h} = 0.22\,\mathrm{m\,s^{-1}}$ and the associated Reynolds number of the flow as $\mathrm{Re} = 5100$. $h$ and $\dot{h}$ provide us with appropriate outer scales, but turbulence is marked by the presence of a large range of scales. The smallest pertinent scales of the flow are those at which viscosity dissipates mechanical energy into heat, termed the Kolmogorov microscale, $\eta$. A dimensional argument can be used to find an estimate for $\eta$ in terms of the outer scale and Reynolds number, and is given by Equation 2.2 [115].

$$\eta/L = \mathrm{Re}^{-3/4} \tag{2.2}$$

From our estimates of outer Reynolds number and length scale, we find an estimate of the Kolmogorov microscale in the present facility as $\eta = 0.33\,\mathrm{mm}$. We can also

find estimates for the Kolmogorov time scale, $\tau_\eta$ from the assumption that $\mathrm{Re}_\nu = \eta u_\eta/\nu = 1$ and $\eta = u_\eta \tau_\eta$. The resulting estimate is $\tau_\eta = 6.4\,\mathrm{ms}$.

The experiments presented involve miscible fluids, so we expect that molecular diffusion will have an impact on the fluid mixing. In general, the strength of molecular diffusion is quantified by the Schmidt number $\mathrm{Sc} = \nu/D$, where $\nu$ is the kinematic viscosity of the fluid and $D$ is the molecular diffusivity. When $\mathrm{Sc} \ll 1$, molecular diffusion is much stronger than viscous diffusion, and the smallest turbulent scales in the flow can be dispersed by molecular diffusion instead of viscous dissipation. The scale at which diffusion takes place is termed the Batchelor scale, $\eta_B = \eta/\mathrm{Sc}^{1/2}$. The Schmidt number describing the diffusion of helium into air is approximately $\mathrm{Sc} = 0.22$, leading to a Batchelor scale in the present flow $\eta_B = 0.70\,\mathrm{mm}$, larger than the Kolmogorov microscale.

Another important scale in the flow is the smallest scale at which Kolmogorov's second hypothesis begins to break down and viscosity begins to have an effect on the dynamics of the energy cascade. In general, this scale is estimated by a scale termed the Taylor microscale, $\lambda$. Like $\eta$, dimensional arguments can be used to find an estimate for $\lambda$, in terms of outer scale and Reynolds number, and is provided in Equation 2.3 [115].

$$\lambda/L = \sqrt{10}\mathrm{Re}^{-1/2} \tag{2.3}$$

The estimate of the Taylor microscale in the present facility is $\lambda = 8.85\,\mathrm{mm}$. In addition, the Reynolds number based on the velocity fluctuation and Taylor microscale, $\mathrm{Re}_\lambda = u'\lambda_T/\nu = 113$. The measurement of the Taylor microscale in the flow is useful for the evaluation of transition to turbulence. Therefore, it is vital that our diagnostic imaging techniques have resolution at least as fine as half the Taylor microscale, to account for Nyquist sampling criterion.

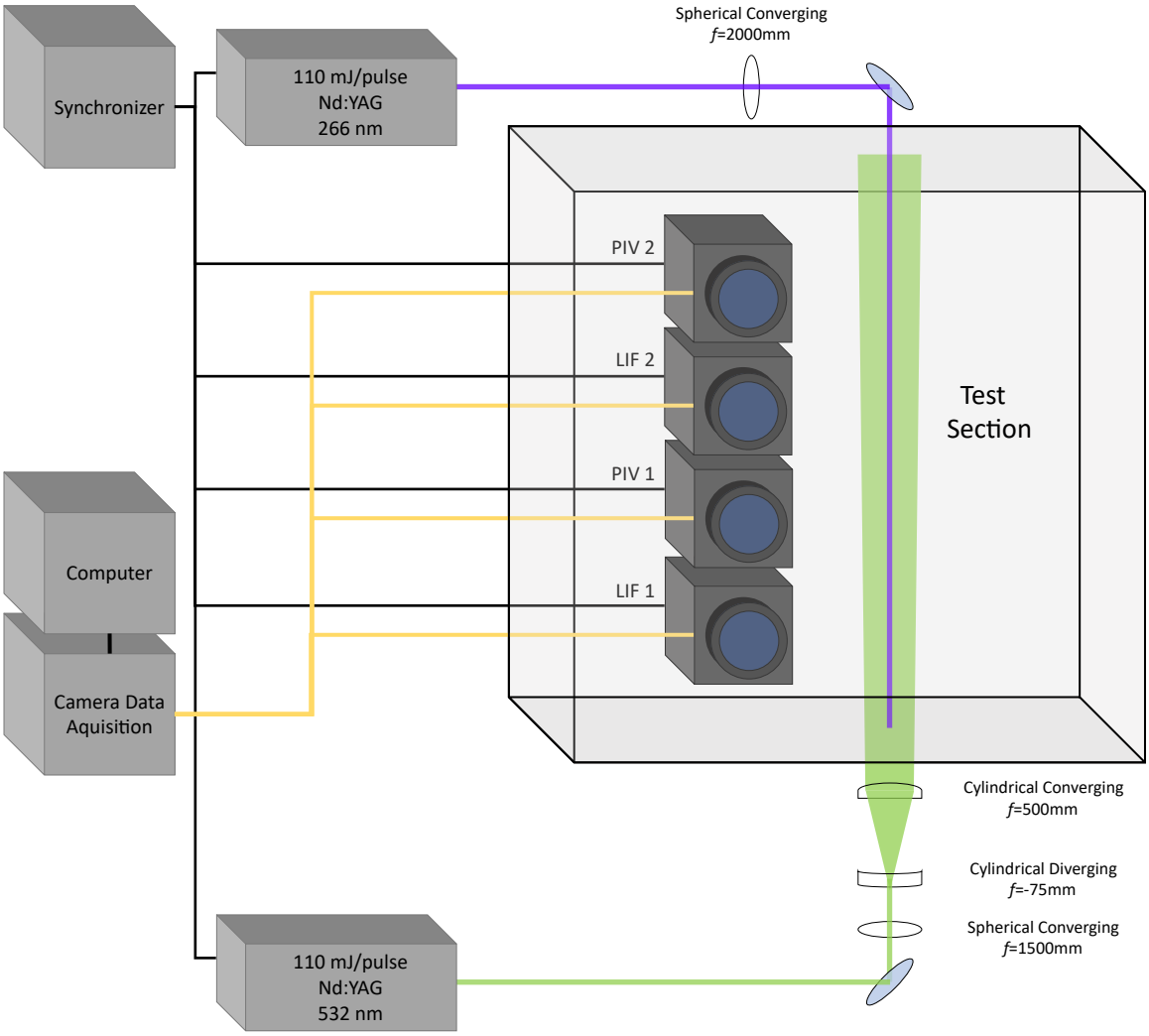


Figure 2.6: A simplified schematic showing the PIV and LIF laser, optics, and camera setups.

### 2.2.2 Particle Image Velocimetry

The dynamics of the instability are measured through particle image velocimetry (PIV). In this technique, small particles that are able to track the flow are seeded into the fluid. The particles are illuminated using a laser sheet and the scattered light is captured by a camera in two successive frames. The displacement of the particles between the frames and the interframe time spacing can be used to measure the velocity of the flow in the directions parallel to the plane.

For PIV seeding, a compressed air line is passed through an olive oil Laskin noz-

zle aerosol generator. The generated particles have a median size of 1 µm [116] and density of 800 kg m$^{-3}$, giving them a Stokes response time of 10 µs [117]. On observation of the particle response time, we find that this timescale is about 3 orders of magnitude smaller than the predicted Kolmogorov time scale, giving confidence that the particles accurately track the smallest fluctuations in the flow. The Laskin nozzle setup was found to be an economical and efficient way to produce a controllable number of particles. Four Laskin nozzles are operated simultaneously, and the output of each one independently flows into a 0.9 m tall Dyson bladeless fan. Two fans are placed in the top stream, and two in the bottom stream, and the fans are staggered and stacked on top of one another to create a uniform injection of particles. In addition, power is delivered independently to each fan, allowing us to control the concentration of particles in each stream.

The particles are illuminated by a laser sheet generated by diverging the beam of a Litron NanoPIV 532 nm Nd:YAG laser, capable of emitting 110 mJ per pulse. To generate the light sheet, the laser first passes through a 1.5 m focal length converging spherical lens that converges the beam so that the beam waist is close to the $y$ origin. This controls the width of the laser sheet so that it is $\approx 1$ mm in thickness at the beam waist. The beam then passes through a $-75$ mm focal length diverging cylindrical lens that spreads the beam into a sheet, followed by a 500 mm converging cylindrical lens that serves to nearly recollimate the sheet to a width of $\approx 5$ cm. The sheet enters into the gas tunnel through the bottom acrylic window and illuminates the region of interest in the $x$-$y$ plane.

The light sheet is scattered by the olive oil aerosol and the illumination is acquired by two TSI PowerView 29MP CCD cameras, fitted with Nikon 50 mm $f/1.8$ lenses. To increase the frame rate of the acquisition, the cameras are operated in $2 \times 2$ binning mode and 12-bit dynamic range, resulting in a PIV image resolution of 3300 px $\times$ 2200 px and a camera frame rate of 1.25 Hz. A Berkley Nucleonics Corp Model 575

delay generator synchronizer controls the timing of the laser and the camera.

PIV correlation maps and vectors are calculated using LaVision DaVis 8.4 software. Before processing occurs, images are rotated and dewarped based on previously captured calibration images. The calibration target used to acquire the calibration images is an in-house manufactured 6.35 mm thick aluminum plate that is 91.4 cm tall and 30.5 cm wide that has been painted matte black and laser engraved with 2 mm diameter dots spaced 10 mm apart. This allows for the plate to fill nearly the full field of view of all of the PIV/LIF cameras at once, allowing a highly accurate calibration between all cameras. Following deformation, the images go through neighborhood median filtering to remove noise, and through a window normalization to improve particle contrast. In addition, because the laser sheet does not pass through the entire field of view, a masking procedure is applied to only apply processing in regions where there is particle intensity. To process PIV images, a recursive Nyquist grid is used to prescribe interrogation windows. The intial interrogation window size is 96 px $\times$ 96 px, and the final interrogation window size is 16 px $\times$ 16 px with 50% window overlap. Windows use Gaussian weighting to emphasize the importance of particles near the center of the window. After every iteration of the recursive Nyquist grid vector calculation, a universal median test is used to remove outliers in the field. Secondary and tertiary peaks are considered for failed vectors, and are used to replace the vector if they successfully pass universal median filtering. Finally, images from different cameras are stitched together based on the calibration images. Vectors in the overlap region between two cameras are averaged with a weighting proportional to the distance from the center of the image.

The final result is an Eulerian description of the $x$-direction velocity $u$ and $y$-direction velocity $v$, in the $x$-$y$ plane. The final field of view imaged is approximately 5 cm in $x$ extent and 80 cm in $y$ extent, with a vector spacing of $\approx 1.1$ mm/vec.

### 2.2.3 Laser Induced Fluorescence

To complement the velocity measurements captured by PIV, laser induced fluorescence (LIF) measurements are captured to analyze the density field. LIF is accomplished by seeding the light gas with acetone vapor, which fluoresces under excitation by 266 nm light.

*Design of the LIF Acetone Bubbler*

The primary challenge of implementing LIF in the gas tunnel was providing a large enough flow rate of acetone vapor into the bottom stream. On first glance, if the bottom stream was to be seeded to 3% acetone vapor by volume, a value typical of many concurrent variable-density mixing experiments [82, 118, 119], and convected at a $1\,\mathrm{m^3\,s^{-1}}$ volumetric flow rate, the acetone usage rate would need to be an astonishing $1.84\,\mathrm{L\,min^{-1}}$ of liquid acetone. Clearly then, the volume concentration of acetone vapor would need to be reduced, without sacrificing too much fluorescent intensity.

To test the minimum required acetone concentration, validation experiments were performed in the adjacent inclined shock tube facility [119, 120]. In this facility, a 266 nm wavelength laser pulse is formed into a sheet and passes through a carbon dioxide/nitrogen gas interface. The nitrogen gas is seeded with vapor acetone, and to control the concentration of acetone, the injected nitrogen is diverged and passed through two mass flow controllers. One mass flow controller is a bypass that flows directly into the inclined shock tube. The other mass flow controller passes nitrogen into an acetone bubbler operated at 22 °C and close to atmospheric pressure. The ratio of acetone vapor pressure to atmospheric pressure at this temperature is 0.27. Our testing in the shock tube began by forming the shock tube interface with nitrogen injected with a ratio of bubbler mass flow rate to bypass mass flow rate of 1 : 15 and capturing images. This is the close to the typical ratio of operation for the shock tube facility. Then, the bubbler to bypass ratio was halved, decreasing the acetone

concentration, and more images were captured. This process was continued until the signal to noise ratio of the acetone fluorescence was approximately 10. The bubbler to bypass ratio at which this occurred was 1 : 480. This corresponds to an acetone volume fraction of 0.05%. This is still too large a volume flow rate of acetone vapor to be safely injected into the gas tunnel. However, this value was attained with a laser sheet of 10 cm width. If the laser sheet width were to be reduced to 2 cm, the increase in laser energy flux would allow for an acetone volume fraction of 0.01% to be sufficient for a signal to noise ratio of 10. After including a safety factor of 2, we aim to build an acetone bubbler capable of delivering $V_{f,acetone} = 0.02\%$ into the bottom stream. The second challenge to tackle is the size of the bubbler necessary to accomplish this task. The shock tube bubbler has a volume of 5.6 L and is capable of safely delivering $0.54\,\mathrm{L\,min^{-1}}$ of acetone vapor into the shock tube. At the previously determined $V_{f,acetone} = 0.02\%$ acetone concentration, and the approximately $1\,\mathrm{m^3\,s^{-1}}$ volumetric flow rate of the bottom tunnel stream, this corresponds to $12\,\mathrm{L\,min^{-1}}$ of acetone vapor flow rate necessary, a 24-fold increase, requiring a 144 L bubbler, an infeasible size. Instead of building such a large bubbler, we leverage our ability to increase the vapor pressure of acetone by increasing the temperature of the liquid, therefore increasing the volume fraction of carried acetone for the same amount of injected nitrogen. The vapor pressures of acetone at 20 °C and 50 °C are 0.24 atm and 0.80 atm, respectively. Therefore, if the acetone temperature is raised to 50 °C, the vapor volume fraction should increase by a factor of 3.33 for a given flow rate of nitrogen, allowing the design of a smaller bubbler. The final bubbler size that should be required is 43.2 L, with a capability of operating at 50 °C or higher.

All of the above calculations assume that the acetone bubbler operates with 100% efficiency, or in other words, that the volumetric flow rate of acetone which is emitted by the bubbler is exactly equal to the theoretical psychrometric flow rate, found by multiplying the volumetric flow rate of the injected gas by the ratio of the vapor

pressure to the gas pressure, which is assumed to be atmospheric. In reality, the efficiency of the bubbler could be much smaller, reducing the overall acetone flow rate and making LIF measurements impractical. To test the bubble efficiency, a smaller 10 L bubbler was built and operated for one hour continuously at 50 °C. The level of liquid acetone in the bubbler was measured before and after operation to determine the volume of liquid acetone used. At the end of one hour, the bubbler had used 0.28 L of liquid acetone, compared to the theoretical usage at this temperature and flow rate, 0.33 L. Thus, the bubbler efficiency was found to be $\epsilon_{bubbler} = 85\%$. This final confirmation of the bubbler characteristics prompted the design and manufacturing of the final gas tunnel acetone bubbler.

Figure 2.7: A 3D model of the acetone bubbler with cross-section cutout

A schematic of the final acetone bubbler is provided in Figure 2.7. The bubbler

is a flanged pipe 20.3 cm in inner diameter and 152 cm in length which is sealed with PTFE gaskets and flange caps at both ends, allowing it to hold up to 49.2 L of acetone liquid. Pressurized nitrogen gas is injected into the bubbler through 4 brass pipes 9.5 mm in diameter which release the gas 21 cm above the bottom flange. As the gas bubbles rise through the acetone bath, acetone vapor is evaporated into the bubble, and continues to travel with the gas as it exits the bubbler. It is then mixed with a bypass line of nitrogen gas to prevent condensation, and the combined stream of acetone vapor seeded nitrogen gas is injected into the gas tunnel through the light gas diffuser (described in Section 2.1.1). The acetone vapor flow rate is controlled by changing two parameters: the temperature of the acetone liquid and the mass flow rate of the nitrogen gas. To control the acetone liquid temperature, a 313 W tape heater is wrapped around the acetone bubbler and surrounded by fiberglass insulation. A T-type thermocouple is inserted into the acetone bath to monitor the liquid temperature. An Omega Inc. CN142 temperature controller with integrated PID control reads the temperature from the thermocouple and cycles the heater on and off until the desired temperature is met. Temperatures as high as 56 °C can be achieved in this way, with larger temperature resulting in larger acetone vapor saturation pressure and subsequently larger vapor concentration in the carrier nitrogen. 56 °C is the boiling point of acetone at atmospheric pressure. The mass flow rate of the nitrogen gas injected into the bubbler is controlled by a King Instument Company acrylic flowmeter, which controls the volumetric flow rate between 4.7 L $\mathrm{min}^{-1}$ to 47 L $\mathrm{min}^{-1}$. A similar flowmeter controls the flow rate of the bypass line. Larger nitrogen gas flow rates generally result in larger acetone vapor concentration, but when the flow rate exceeds 50 L $\mathrm{min}^{-1}$ the vigorous injection results in acetone liquid being ejected from the bubbler and entering into the light gas diffuser. Overall, the volumetric flow rate of acetone seeded nitrogen and bypass nitrogen into the tunnel never exceeds 100 L $\mathrm{min}^{-1}$. Considering the 0.51 $\mathrm{m}^2$ area of the test section, this flow rate results

in a $0.003\,\mathrm{m\,s^{-1}}$ increase in the test section convective velocity, making the acetone seeding negligible in the calculation of the experiment Atwood number and light gas injection flow rate.

*LIF Image Acquisition and Processing*

A Litron laser capable of producing 110 mJ per pulse at 266 nm wavelength is used as the energy source for LIF. The emitted beam is focused by the use of a 2000 mm focal length converging spherical lens and oriented in the test section vertically. The beam is not perfectly collimated, but varies from a waist diameter about 0.8 mm at the vertical origin of the test section to a diameter of 1.4 mm at the edges of the field of view. While the original plan was to excite the acetone with a laser sheet of 2 cm width, tests showed that the laser power of the diverged sheet was not sufficient to acquire clear LIF images.

Similar to the PIV setup, two TSI PowerView 29MP CCD cameras with Nikon 50 mm $f/1.2$ lenses are used to capture the fluorescence signal. To prevent the scattering from PIV particles from appearing in the image, a 532 nm wavelength notch filter is added to the lenses. To maximize the signal response and frame rate, the cameras are operated in 8 px $\times$ 8 px binning mode and with 14 bit resolution. This allows data to be captured at a rate of 1.25 Hz. In order to ensure that the LIF fluorescence and the PIV scattering do not appear in the same images, the LIF laser pulse is fired 200 µs before the first PIV laser pulse.

The images captured undergo significant correction to extract the quantitative concentrations of the heavy and light gas, $f_1$ and $f_2$, respectively, across the $y$-axis. When coupled with the density information of the incoming streams, these concentrations can be used to determine the density field, $\rho$.

The steps taken in processing the LIF raw images are illustrated consecutively in Figures 2.8, 2.9, and 2.10. The LIF images do not just capture intensity from the acetone fluorescence, but also some intensity from glare and reflections off of the background material and acrylic window. To remove these, a background image is generated from the LIF data set. First, the line representing the LIF signal is masked from every image in the data set. Next, the images with the line removed are averaged to generate an average background intensity map. Finally, an interpolated filling process is used to estimate the magnitude of the background intensity in the region of the LIF signal. The first step in LIF processing is to subtract the background content from each LIF image.

After the LIF images are background subtracted, they are deformed into real-world coordinates based on a previously captured calibration image using a $3^{\text{rd}}$ order polynomial fit. Following deformation to world coordinates, the images are masked to only contain the beam region.

At this point, we begin the process of stitching the results from the two camera

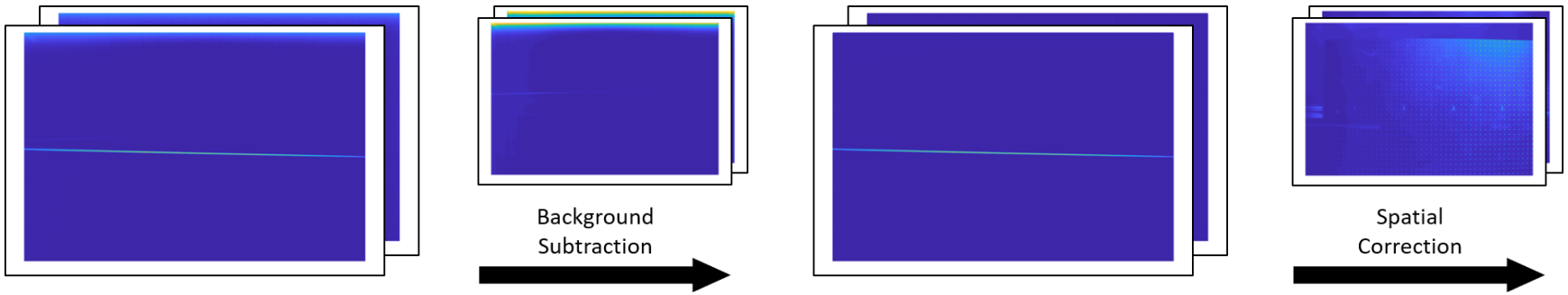


Figure 2.8: Images showing the methodology for processing the LIF images (1/3). Raw images first go through background subtraction, and are then transformed to world coordinates through the use of previously acquired calibration images.

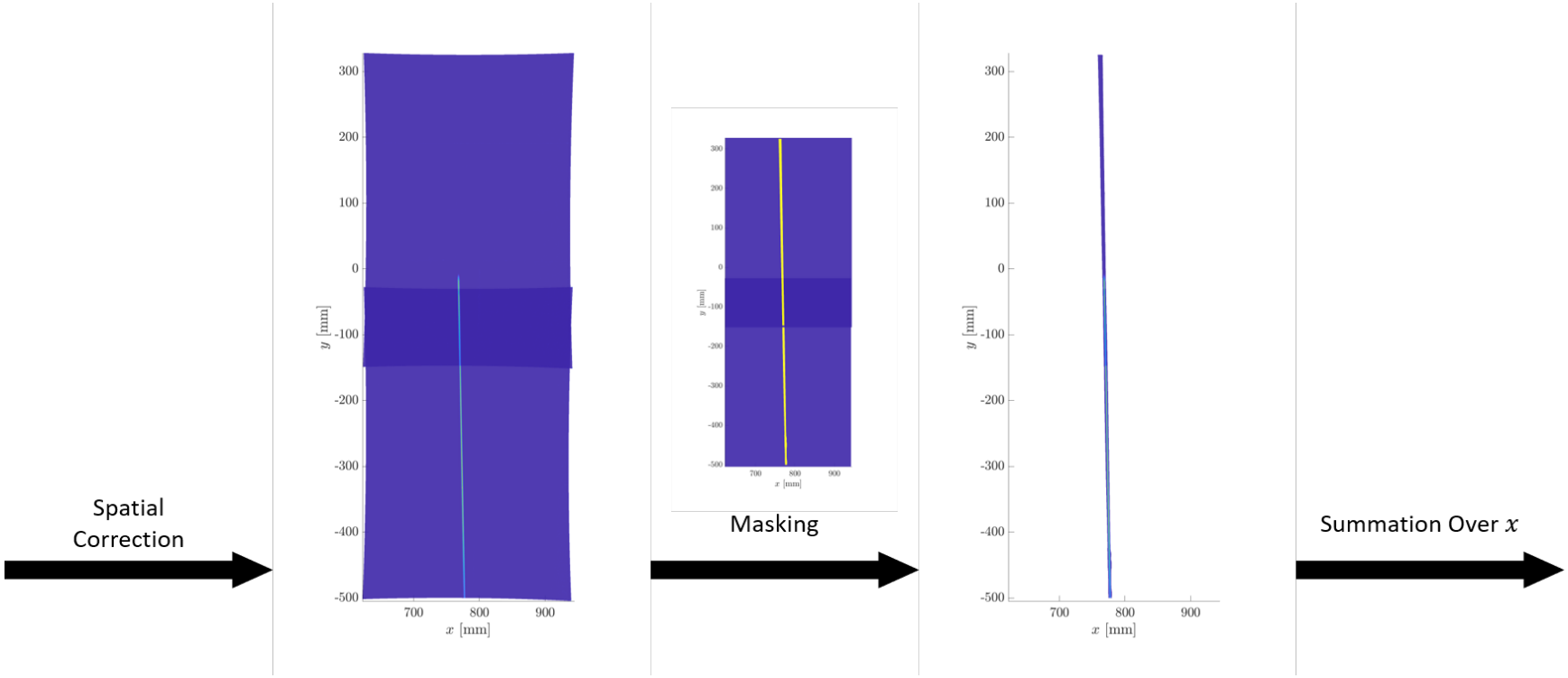


Figure 2.9: Images showing the methodology for processing the LIF images (2/3). Coordinate transformed images are masked, and pixel intensity is summed across $x$ to obtain the variation in line intensity along the beam path

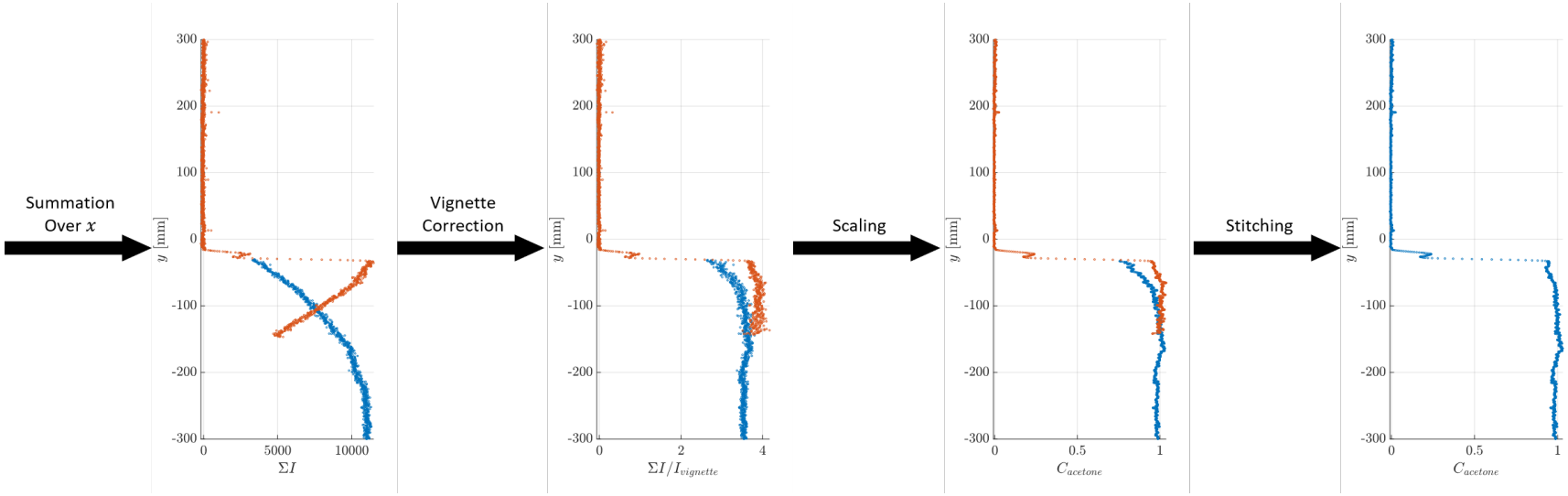


Figure 2.10: Images showing the methodology for processing the LIF images (3/3). Raw line intensities are vignette corrected, filtered, scaled to the appropriate concentrations, and stitched to form the final concentration profile.

frames together. The image frames from both cameras have already been transformed into world coordinates, but do not sit on the same grid due to small misalignments in the camera positioning. To correct this, we begin by defining an overall world coordinate grid with the resolution of the least-resolved camera. We then perform a 2D linear interpolation of each image frame onto the overall world coordinate grid so that the image frames have identical grids.

Because the LIF signal exists only on a narrow line, it is infeasible to try to calculate variations in the intensity across $x$ locations. Instead, we reduce the image into a measurement of intensity at each $y$ location along the laser line. We do this by summing the image intensity along $x$ for every $y$ position in the image. Assuming the fluorescence signal is linear to the laser excitation and the concentration of acetone, it serves to assume that the summed image intensity at every $y$ position should also be proportional to the summed laser excitation at that $y$ position and the average concentration of acetone at that $y$ position. Because the attenuation of the laser excitation is very weak, the summation of the laser intensity along $x$ for every $y$ position remains constant along the laser line. Thus, the summed intensity at each $y$ location is only a function of the average concentration in that region. In this sense, we are interrogating a cylindrical cross-section of the laser beam to find the average concentration of the cross-section. The beam is not perfectly parallel to the $y$ axis, and so, in addition, the central $x$ location of the beam is selected and saved at each $y$ location.

Because of this summation process, the resolution of the interrogation of the beam in the $y$ direction (approximately 0.28 mm) is much finer than the width of the beam ($\approx$1 mm). To correct this issue, we apply a Gaussian filter to the LIF data with width equal to the width of the beam. This filter was selected because the beam profile itself is Gaussian.

Next, a flat-field correction is applied to the filtered intensity line to remove the

impact of camera vignetting. Because the LIF signal is weak, the aperture of the camera is opened to an $f$-stop of 1.2. At such open apertures, vignette effects become commonplace, leading to images which are brighter near the center and darker at the edges. To normalize the captured images to a flat-field, we capture a series of 120 images of an unmarked matte white poster board that is diffusely illuminated from behind. The illumination technique results in an image object which reflects light diffusely and evenly. The average of these images shows the clear vignette effect, with more intensity at the center of the image. We apply the same mask to the average flat-field image as the one applied to the LIF images, and perform a summation over $x$ at every $y$ position to obtain a curve representing the overall deviation from the flat-field at every $y$ position on the line. The LIF intensity is divided by the masked averaged flat-field image to obtain the flat-field corrected LIF signal.

Lastly, the two intensity lines must be scaled to represent concentration and stitched together. Because the bottom image contains the pure seeded fluid, this image data is corrected first. A region in the image is selected to represent the area of pure seeded fluid with with $f_2 = 1$, and the entire intensity line is scaled by the mean intensity in that region. Next, a region in the overlap between the cameras is selected to scale the top image data. The mean $f_2$ in the bottom camera data in this region is selected to represent the mean $f_2$ in the top camera data in the same region. The entire intensity line in the top image data is then scaled by the mean intensity and $f_2$ in the overlap region. The image lines are stitched using a weighting based on distance from the center of their respective image. Finally, a data threshold is applied so that the volume fraction data solely lies between $0 \leq f_2 \leq 1$.

The final result is a LIF data table of $x$, $y$, and $f_2$ measurements along the path length of the beam. The overall field of view captured by the LIF cameras is a narrow line approximately 80 cm in $y$ extent, with a resolution of $\approx 0.28$ mm/px. The concentrations along the beam path have been filtered by a Gaussian filter with

half-width $\approx 1\,\text{mm}$, which corresponds to $\approx 4\,\text{px}$.

The primary achievement of the combined PIV/LIF technique is the simultaneous measurement of density and velocity, and therefore the ability to describe how the dynamics and mixing in the RTI flow are linked. However, the PIV and LIF data must be registered onto the same grid so that combined velocity-density statistics can be computed. To accomplish this process, for every LIF data table, we linearly interpolate the associated PIV vector field to find the value of horizontal and vertical velocity at each $x$ and $y$ location along the path length of the LIF beam. Because the resolution of the LIF measurement is finer than that for PIV, this results in oversampling of the PIV data field. However, we take care to not make any measurement of structure or scale from this oversampled PIV vector field, and for any independent statistics which can be measured solely from the PIV field, we only use the PIV vector field in its original resolution.

### 2.2.4 Uncertainty Quantification

PIV velocity vectors are subject to two main sources of uncertainty: systematic and instantaneous. Systematic uncertainty derives from limitations in the PIV setup, whereas instantaneous uncertainty comes from uncertainty in the PIV vector correlation method.

There are many causes of systematic uncertainty in PIV measurements. One of these is poor particle seeding, the result of either too many or not enough particles in each interrogation window. Keane and Adrian [121] found that the number of spurious PIV vectors reduced dramatically as the number of particles per interrogation window approached 10. To ensure this in our experiments, we fitted a nozzle valve to the compressed air line driving the Laskin nozzle olive oil aerosol generators. The nozzle valve could be modulated to change the overall seeding density until 10-15 particles could be found in each interrogation volume. Another limitation to PIV can be

pixel locking due to insufficient camera resolution or small particle size [122]. In this situation, particles in the PIV field are not large enough to scatter light onto more than a single pixel, and as a result, the correlation algorithm is locked to specifying velocities only at multiples of the pixel size. One of the largest sources of systematic error in PIV measurements is the impact of out-of-plane particle displacement. Movement of particles in the out-of-plane component can be interpreted as motion in the plane due to perspective effects, or can affect the location of the correlation peak because of the presence of particles which seem to be "frozen" in the flow [123]. In flows that are mostly two-dimensional, these errors can be minimized with an appropriate selection of inter-frame delay. However, in flows that are distinctly three-dimensional, it has been shown that this error can increase to up to 15% of the mean flow velocity [123]. In the current experiment, the flow is primarily two dimensional, with in-plane velocities $u \approx U_c = 1.47\,\mathrm{m\,s^{-1}}$, and $v \approx v'_{max} = 0.15\,\mathrm{m\,s^{-1}}$, and out-of-plane velocity $w \approx u'_{max} = 0.07\,\mathrm{m\,s^{-1}}$.

Instantaneous PIV uncertainties are calculated using a correlation statistics method by LaVision DaVis 8.4 [124]. This method calculates the uncertainty of the displacement correlation peak based on its shape and asymmetry. This uncertainty method accounts for many types of systematic error as well, such as out-of-plane motion, seeding density, background intensity noise, and variation in particle size. One question that may arise is whether the uncertainty in the velocity measurement attained from PIV varies as the RTI mixing width grows or at different locations in the mixing width. To answer this, we show representative instances of the PIV uncertainty for both $u$ and $v$ at the three mixing locations at which PIV is measured in Figure 2.11. The first thing to note is the large uncertainty at the edges of the PIV sheet due to particles which are entering or exiting the illuminated field of view. In these regions, the PIV algorithm cannot accurately compute a displacement from the correlation map because particles are "disappearing" from the field of view. As such, this re-

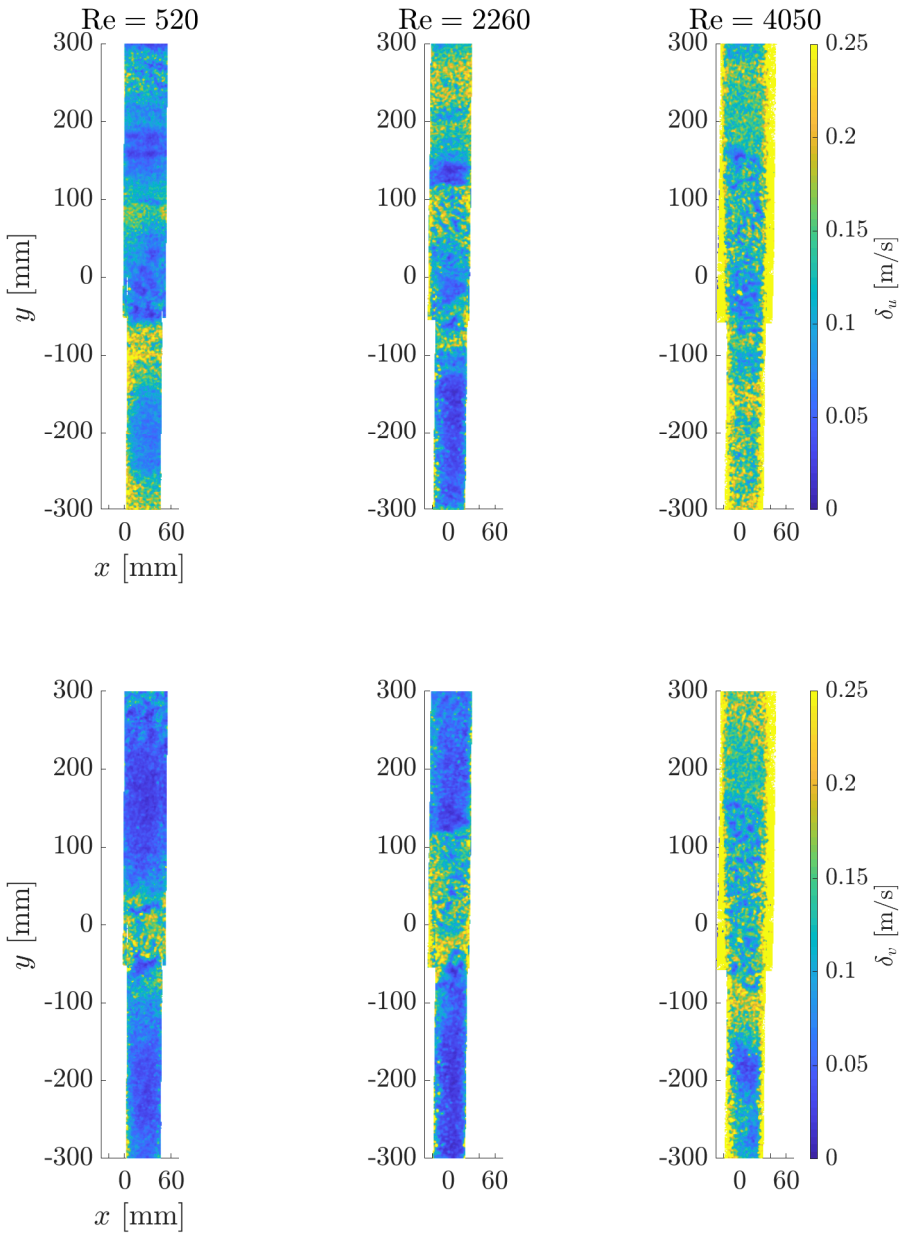


Figure 2.11: Examples of the relative PIV uncertainty fields for both $u$ and $v$, measured at the three mixing Reynolds numbers.

gion cannot be used for accurate measurements. In the core of the PIV sheet, there are clear trends in the $\delta_u$ and $\delta_v$ fields as the mixing region centered around $y = 0$ grows. $\delta_v$ tends to peak at the core of the mixing region, whereas $\delta_u$ has maximum value near the interface between the mixing region and the free-stream. In general, the uncertainty in the mixing region is larger than that in the free-stream, so as the mixing region grows, the region of larger uncertainty also grows. Despite this, it does not seem that the uncertainty in the free-stream itself grows significantly between different $x$ locations.

Uncertainty in the LIF measurement can be affected by the dynamic range of the camera, vignette effects, signal-to-noise ratio, attenuation in laser irradiation due to absorption, and non-uniformity in the acetone vapor seeding. The cameras used for LIF measurement have a maximum dynamic range of 14-bits, meaning that measurements of count on each pixel is evaluated as an integer between 0 and $2^{14}-1 = 16383$. In practice, the maximum intensity of any image is closer to $\approx 1100$ counts in every image. Because of the vignette effect described in Section 2.2.3, this maximum is even smaller near the edges of the image, where it is closer to $\approx 250$ counts. Limiting things further is the noise resulting from the background intensity, which is $\approx 30$ counts across the image, reducing the effective dynamic range to $\approx 1070$ in the center of the image and $\approx 220$ at the edges. The corresponding effective signal-to-noise ratios in the center of the image and edge of the image are approximately 30 and 7, respectively.

Most other LIF experiments discuss applying a Beer-Lambert attenuation correction to correct the loss of laser irradiation as the laser passes through the fluorescent medium [43, 82, 118, 119]. These experiments find an estimate for the attenuation length scale by locating a region of fluid which contains pure seeded fluid and fitting an exponential curve to describe the decay in fluorescent intensity along the beam path in this region. However, on analysis of our data, we find that intensities do not

decay strongly in the pure-fluid region. Instead, the LIF intensity is nearly constant through the entire pure-fluid region. In other words, it seems that the test section is "optically thin" in regards to the absorption of the laser excitation. This is no surprise considering the low concentration of fluorescent acetone vapor that is being used in this experiment. The length scale of the acetone attenuation can be predicted using the fluorescent properties of acetone at atmospheric conditions in air recorded by Thurber [125]. If we assume that the fluorescent cross-section is $\sigma = 4.4 \times 10^{-20}\,\mathrm{cm}^2$, the number density of the flow is that for an ideal gas at standard temperature and pressure, $n = 0.025 \times 10^{21}\,\mathrm{cm}^{-3}$, and the acetone concentration is the maximum producible by the acetone bubbler, $V_{f,acetone} = 0.01\%$, then the attenuation length scale, $L = 1/\sigma n V_{f,acetone} = 90.8\,\mathrm{m}$. In other words, over the 1.6 m path length of the beam through the gas tunnel test section, attenuation can at most reduce the fluorescence by 1.7%. This small amount of attenuation justifies our assumption of an "optically thin" test section. Because of the small impact, we choose not to apply Beer-Lambert attenuation correction to any of the images processed. Instead, we account for this 1.7% variation as part of the experimental uncertainty of the LIF measurement.

The most significant source of uncertainty in the LIF measurement is due to inhomogeneity of acetone concentration in the seeded stream. Usually, if the fluorescent marker is well mixed with the seeded fluid, then the strength of fluorescence can be correlated to the concentration of fluorescent marker and therefore to the seeded fluid. If the fluorescent marker is not well mixed, then the concentration of fluorescent marker is not necessarily correlated to that of seeded fluid, and the strength of fluorescence fails to properly capture the concentration of the underlying mixing. To measure the extent of the related uncertainty due to inhomogenous acetone concentration, we look at the LIF data in a region of "pure" acetone seeded fluid far away from the mixing width and calculate the variation in the concentration measurement across all images. Specifically, we evaluate the LIF data measured at $x = 75\,\mathrm{cm}$ in

the region where $y < 15\,\text{cm}$. We find that the standard deviation of the measured concentration in this region is 0.038. This serves as an estimate for the variance in volume fraction taken from the LIF measurement as a result of inhomogenous acetone concentration.

In addition to instantaneous and systematic measures of uncertainty of our velocity and density measurements from PIV/LIF, we must also estimate the uncertainty in statistical moments of velocity and density. The central limit theorem implies that as the number of sample measurements $N$ of a population measure $\hat{\phi}$ increases, the accuracy of the measure increases at the rate of $\sqrt{N}$ and is proportional to the uncertainty of the measure estimate $\phi$ [126]. In other words,

$$\sigma_{\hat{\phi}} = \frac{\sigma_\phi}{\sqrt{N}} \tag{2.4}$$

where $\sigma_{\hat{\phi}}$ and $\sigma_\phi$ are the standard deviation of the measure and the estimator, respectively. Sciacchitano and Wieneke [127] has applied the central limit theorem to a variety of PIV/LIF statistical moments and provided equations for the uncertainty of these quantities. Given a set of $N$ sample measurements of $\phi = \{\phi_1, \phi_2, ..., \phi_N\}$ with mean $\overline{\phi}$, and standard deviation $\sigma_\phi$ then we can find the uncertainty of the population mean as

$$\delta_{\overline{\phi}} = \frac{\sigma_\phi}{\sqrt{N}} \tag{2.5}$$

and the uncertainty of the population standard deviation as

$$\delta_{\sigma_\phi} = \frac{\sigma_\phi}{\sqrt{2(N-1)}}. \tag{2.6}$$

If a second sample measurement of a different quantity $\psi = \{\psi_1, \psi_2, ..., \psi_N\}$ is also measured, then we can also obtain the uncertainty of the covariance between $\phi$ and

$\psi$ as

$$\delta_{\sigma^2_{\phi\psi}} = \sigma_\phi \sigma_\psi \sqrt{\frac{1 + R^2_{\phi\psi}}{N-1}} \tag{2.7}$$

where $R_{\phi\psi} = \mathrm{cov}(\phi, \psi)/\sigma_\phi \sigma_\psi$ is the cross-correlation coefficient between $\phi$ and $\psi$.

The above equations can be used to find uncertainty profiles for the mean and fluctuating components of velocity and density, as well as combined correlations of these quantities. However, they do not take into account the instantaneous uncertainty associated with each individual sample measurement. To take this into account, Sciacchitano and Wieneke [127] suggests decomposing the variance of each statistical quantity into two components,

$$\sigma^2_\phi = \sigma^2_{\phi,fluct} + \overline{\delta^2_{\phi,inst}} \tag{2.8}$$

where $\sigma^2_{\phi,fluct}$ is the measured variance of the sample not taking into account instantaneous uncertainty, and $\overline{\delta^2_{\phi,inst}}$ is the mean square of the instantaneous uncertainty.

All together, equations 2.5, 2.6, and 2.7 along with equation 2.8 can be used to find uncertainty estimates for important quantities in the flow. The described methodology is that used to compute the uncertainties presented in the results section.

# CHAPTER 3
# SIMULTANEOUS DENSITY-VELOCITY MEASUREMENTS OF THE RAYLEIGH-TAYLOR INSTABILITY

The following Chapters 3, 4, and 5 present the results obtained from three experiments performed in the gas tunnel facility. This chapter begins with an outline of the experimental campaign and the details of the three experiments performed. In the remainder of this chapter, some typical statistical quantities and profiles frequently discussed in the RTI community are presented based on the simultaneous density-velocity measurements captured by our PIV/LIF technique. Comparisons are made to RTI experiments at larger Atwood number [76] and large Schmidt number [71], as well as RANS simulations [109] and DNS [110]. Conditional sampling techniques are used to separate the relative impact of the bubble and the spike on the statistics. The results shown in this chapter are then used to quantify measures of the molecular mixing in Chapter 4. Finally, in Chapter 5, by using the combined PIV/LIF data and the assumption of self-similarity at large Reynolds number, we will consider the transfer of energy in the RTI flow from its release as gravitational potential energy, to the production of turbulent kinetic energy, and eventually to its dissipation into heat through viscous effects.

## 3.1 Outline of Experimental Campaign

In order to achieve the objectives laid out in Section 1.5, an experimental campaign was designed which would provide simultaneous density-velocity measurements of the Rayleigh-Taylor instability.

The selection of Atwood number balanced two important criteria in the operation of the gas tunnel facility. At small $\mathcal{A} \approx 0.01$, the sensitivity of the gas stream

densities to small variations in temperature can lead to large uncertainties in the experimental Atwood number, and therefore large uncertainty in scaling parameters and density calculations. Meanwhile, to operate the gas tunnel at large $\mathcal{A} \approx 0.7$, the large injection flow rates results in the helium storage tanks being emptied quickly. As a result, the experimental time is short and insufficient to acquire large experimental data sets. Considering this balance, $\mathcal{A} = 0.1$ was selected as an appropriate Atwood number for this experimental campaign.

After selection of the Atwood number, the selection of convective velocity can be made by assuming the growth rate of the instability follows the quadratic form of equation 1.7 and choosing a convective velocity that would result in the instability reaching a particular mixing height by a certain convective location in the tunnel. For this experiment, we desired that the total mixing width would reach 0.8 m, approximately half the total height of the tunnel, by the time the flow reached the $x = 1.75\,\mathrm{m}$. This would allow the flow at this location to remain encapsulated within the field of view of the diagnostics, while also staying away from the furthest downstream locations in the test section where certain undesirable upstream swirl and compression effects were noticed to be affecting the flow. To accomplish this criteria, the convective velocity of the tunnel would need to be set to $U_c = 1.45\,\mathrm{m\,s^{-1}}$.

As the flow convects through the tunnel and the mixing height grows, the Reynolds number based on mixing height and mixing height growth rate increases. Many previous RTI experiments, such as Ramaprabhu and Andrews [71] and Akula and Ranjan [76] showed that a transition to a self-similar state occured at Re $> 1000$. Therefore, two Reynolds numbers past this state were selected in order to test if self-similarity was achieved. In addition, one Reynolds number below this criteria was selected to point out differences between the flow conditions before and after the transition to self-similarity. All together, three Reynolds numbers were chosen for the experimental campaign: Re $\approx$ 500, 2000, and 4000, which occur respectively in the

flow at downstream locations of $x \approx 0.75\,\mathrm{m}$, $1.25\,\mathrm{m}$, and $1.75\,\mathrm{m}$.

Table 3.1: Outline of experimental settings for the simultaneous PIV/LIF campaign.

| Target Re | Re | $x$ [m] | $\mathcal{A}$ | $\rho_1$ [kg m$^{-3}$] | $\rho_2$ [kg m$^{-3}$] | $U_c$ [m s$^{-1}$] | $\nu$ [m$^2$ s$^{-1}$] |
|---|---|---|---|---|---|---|---|
| 500 | 520 | 0.75 | 0.098 | 1.176 | 0.966 | 1.42 | $1.687 \times 10^{-5}$ |
| 2000 | 2260 | 1.25 | 0.092 | 1.171 | 0.973 | 1.53 | $1.677 \times 10^{-5}$ |
| 4000 | 4050 | 1.75 | 0.096 | 1.167 | 0.963 | 1.48 | $1.684 \times 10^{-5}$ |

Table 3.1 lists the settings for the three experiments conducted in this campaign. The true Reynolds number, calculated later in Section 3.3 is based on the mixing height found from LIF data and the fluctuating velocity components found from PIV. The gas densities and Atwood numbers are found from the pressure and temperature measurement devices equipped on the light gas injection line and in the gas tunnel streams. These densities and the associated fluid concentrations are used to compute the gas mixture viscosity, using the method of Wilke [128]. The convective velocities are found from PIV, and used to compute the instability development time by applying Taylor's hypothesis, together with the streamwise location.

Because of adiabatic cooling, the gas in the light gas injection system gas cylinders drops in temperature as it moves from high pressure to low pressure. As a result, the density of the injected gas and the resulting Atwood number changes in time. Figure 3.1 shows this Atwood number variation with experimental time, along with the 95 % confidience interval uncertainty. As the temperature of the injected gas decreases, the density of the lower stream rises to be closer to that of the upper stream. This results in a gradual decrease in Atwood number over time. To reduce this effect, all experiments were operated in two separate runs, the first operated over 180 s of experimental time, and the second over 60 s. Between runs, the gas cylinders were left untouched over the course of 3 h to 4 h to allow their temperature to normalize back to room temperature. The beginning of each experiment is met with a period of approximately 10 s in which the flow is developing into a statistically stationary

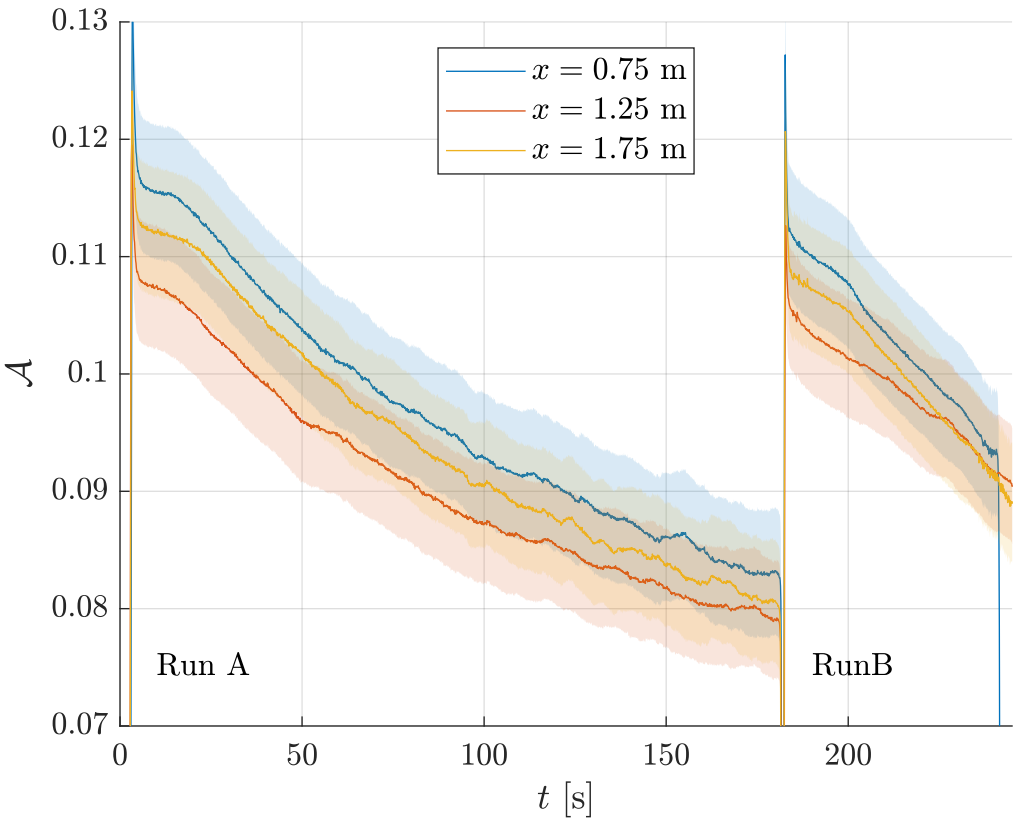


Figure 3.1: The variation of experimental Atwood number and associated uncertainty (95 % confidence interval) over time for all six total experimental runs, comprising three Reynolds number experiments.

state. Data from this observation period is not used. This leaves approximately 220 s total of usable experimental time for each downstream location which, at the 1.25 Hz capture frequency of the PIV/LIF cameras, results in 275 image captures per experiment.

## 3.2 LIF Results

### 3.2.1 Volume Fraction and Mixing Width

Processing a single acquired LIF image provides an instantaneous measure of the volumetric concentration of fluorescent acetone marker $C_{\text{acetone}}$ at each $y$ location along the path of the excitation laser beam. The density of the flow can then be

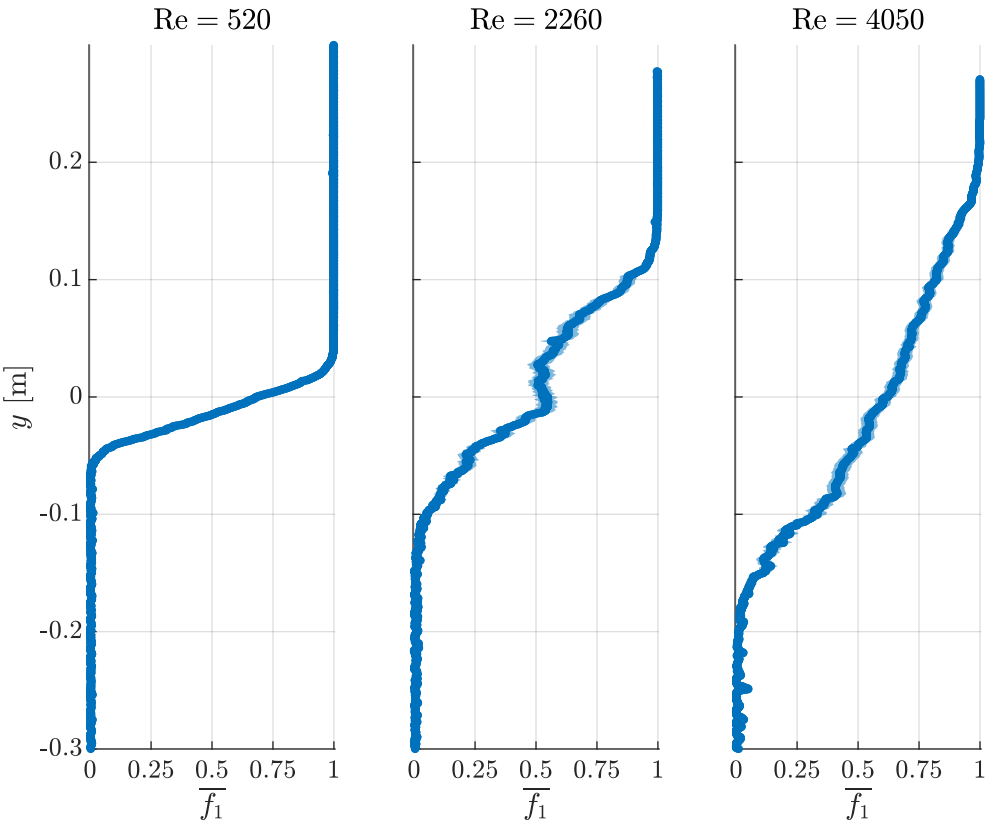


Figure 3.2: Profiles of the mean volume fraction of the heavy gas stream, $\overline{f_1}$, at the three Reynolds numbers tested.

found with the assumption that the acetone concentration is a perfect marker of the volumetric concentration of the bottom stream. The resulting equation for density, $\rho = \rho_1(1 - C_{\text{acetone}}) + \rho_2 C_{\text{acetone}}$ is applied to each instantaneous LIF capture to obtain the instantaneous density profile. A measure for the instantaneous volume fraction of fluid 1 (the fluid of larger density), $f_1$, can then be found as $f_1 = (\rho - \rho_2)/(\rho_1 - \rho_2)$, and the corresponding instantaneous volume fraction of fluid 2, $f_2$, as $f_2 = 1 - f_1$.

Because the gas tunnel facility is statistically stationary, ensemble averages of instantaneous measurements are equivalent to temporal averages (although at a small temporal resolution of 1.25 Hz). In this work, we show the ensemble averages of a set of instantaneous measures $\{\phi_1(x,y), \phi_2(x,y), ..., \phi_N(x,y)\}$ as $\overline{\phi}(x,y) = \frac{1}{N}\sum_{i=1}^{N}\phi_i(x,y)$. The fluctuating components, $\phi_i'$ are then found by subtracting the ensemble mean

Table 3.2: Measures of the bubble and spike heights, the half-width of the mixing region, and the mixing centerline for the three Reynolds numbers investigated.

| Re | Spatial Widths [cm] | | | | |
|---|---|---|---|---|---|
| | $h_b$ | $h_s$ | $h$ | $y_0$ | $h_f$ |
| 520 | 2.08 | -4.82 | 3.45 | -1.37 | 8.69 |
| 2260 | 11.12 | -10.09 | 10.60 | 0.51 | 27.48 |
| 4050 | 16.26 | -16.34 | 16.30 | 0.04 | 38.41 |

from the instantaneous measurement, $\phi_i' = \phi_i - \overline{\phi}$.

The profiles of $\overline{f_1}$ for the three Reynolds numbers considered is shown in Figure 3.2, together with bands representing the uncertainty in the mean. The volume fraction profiles transition gradually from one pure fluid region to another. The $y$ location at which $f_1 = 0.5$ is not coincident with the splitter plate location, $y = 0$ for most of the experiments considered. This may be due to a slight angle relative to the normal in the test section, or small errors in the positioning of the camera calibration plate origin. In addition, small differences in the velocity in the top and bottom stream might lead to preferential spreading of the mixing region into the top or bottom stream [129] in a way that may not be consistent between different experimental runs.

Measures for the bubble height, $h_b$, and spike height, $h_s$, are found from the profiles of $\overline{f_1}$ by finding the $y$ locations at which $\overline{f_1} = 95\,\%$ and $5\,\%$, respectively. The centerline of the mixing region, $y_0$, is then defined as the average between $h_b$ and $h_s$, $y_0 = (h_b + h_s)/2$, and the half-width of the mixing region, $h$, is defined as half the distance between $h_b$ and $h_s$, $h = (h_b - h_s)/2$. The values of these measures are presented in Table 3.2.

The measurements of $h$ and $y_0$ can be used to normalize the $y$ coordinate into a self-similar vertical spatial coordinate, $Y = (y - y_0)/h$. This non-dimensionalization will be used frequently to compare profiles between experiments at different Reynolds numbers. The self-similar profiles of the mean volume fraction are shown in Figure 3.3, superimposed with an error function profile which generally describes the shape of

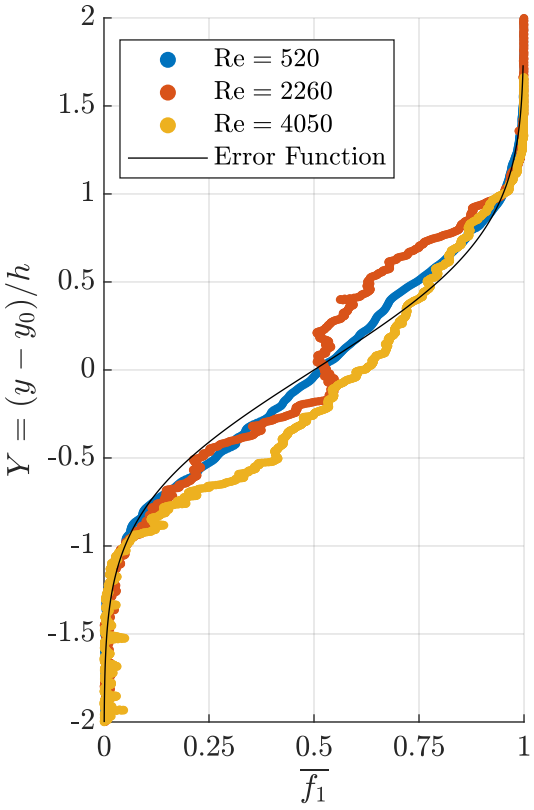


Figure 3.3: Normalized profiles of the mean volume fraction of the heavy gas, $\overline{f_1}$ for the three Reynolds numbers tested. Superimposed is an error function profile of equal width.

the profile. This function describing this error function fit, $f_{\text{erf}}(Y)$, has been selected such that $f_{\text{erf}}(1) = 0.95$ and $f_{\text{erf}}(-1) = 0.05$ to match with the definitions of the mixing width used above. There is good collapse of the profile shape, even for the small Reynolds number case.

Andrews and Spalding [39] outlined another method for calculating the mixing width based on the assumption that the volume fraction $f_1$ profile is linear through the mixing region and transitions sharply to a constant of unity at the top edge of the mixing region and a constant of zero at the bottom edge. The total mixing height, $h_f$, can then be found by performing an integral over the domain of the two volume

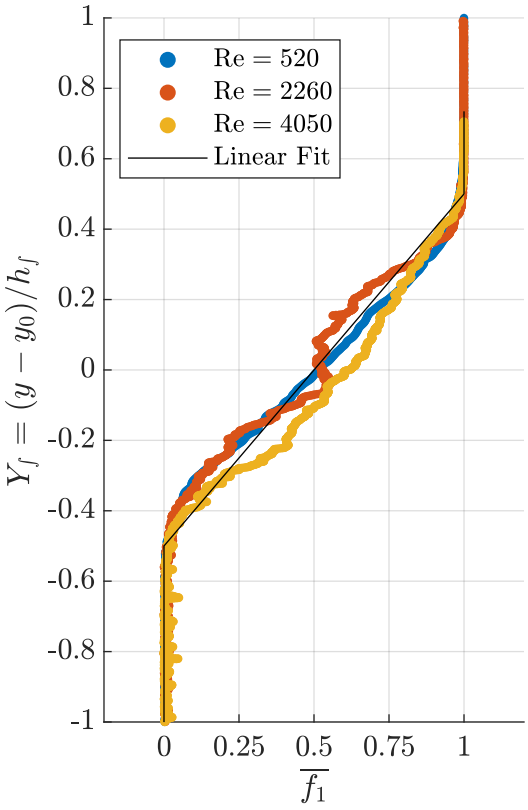


Figure 3.4: Normalized profiles of the mean volume fraction of the heavy gas, $\overline{f_1}$ for the three Reynolds numbers tested, but with the spatial coordinate normalized by $h_f$ instead of $h$. Superimposed is the linear volume fraction profile assumed by Andrews and Spalding [39].

fractions,

$$h_f = 6 \int_{-\infty}^{\infty} \overline{f_1} \left(1 - \overline{f_1}\right) dy, \tag{3.1}$$

where the factor of six comes from the assumption that the RTI concentration profile is linear through the mixing region. $h_f$ can be used to construct a non-dimensional spatial parameter, $Y_f = (y - y_0)/h_f$, similar to the way that we previously used the mixing width $h$ to construct $Y$. The measures of $h_f$ for the three experiments performed are presented as a separate column in Table 3.2, and the profiles of the mean volume fraction normalized against $h_f$ are presented in Figure 3.4. Good collapse is shown in the profile shape again, as it appears that the linear profile better es-

timates the gradients of the volume fraction through the core of the mixing region, only showing deviation from the measured data at the edges of the mixing region.

There is significant interest in the community in the measurement of the RTI growth rate parameter, $\alpha$. Most methods for the computation of $\alpha$, like the virtual origin method [65] or the self-similar growth rate method of Ristorcelli and Clark [34] require the continuous measurement of $h$ at many instability development times, $t$. We are limited in the current experiment with only three measurements. However, Livescu et al. [130] outlines a method for calculating $\alpha$ based on only a few measurements taken in the self-similar regime. If $h(t_1)$ and $h(t_2)$ represent two measurements of $h$ taken at different instability development times in the self-similar regime, then

$$\alpha = \left( \frac{h(t_2)^{1/2} - h(t_1)^{1/2}}{(\mathcal{A}g)^{1/2}(t_2 - t_1)} \right)^2 . \tag{3.2}$$

This equation can be found by integrating the self-similar growth rate equation over time. We can apply this methodology using the results from the two largest Reynolds number experiments to find an estimate of the growth rate parameter and its uncertainty:

$$\boxed{\alpha = 0.049 \pm 0.009}. \tag{3.3}$$

This value is similar to that found in other experimental works [58, 71, 76].

Finally, Figure 3.5 shows the root-mean-square fluctuations of the density for the three Reynolds numbers tested. Interestingly, while the density fluctuations remain at a similar value at the edges of the mixing layer, there is a trend towards smaller core fluctuation values as the Reynolds number increases. This suggests that as the flow develops and molecular mixing begins to occur, the inhomogeneity of material in the core of the mixing region decreases.

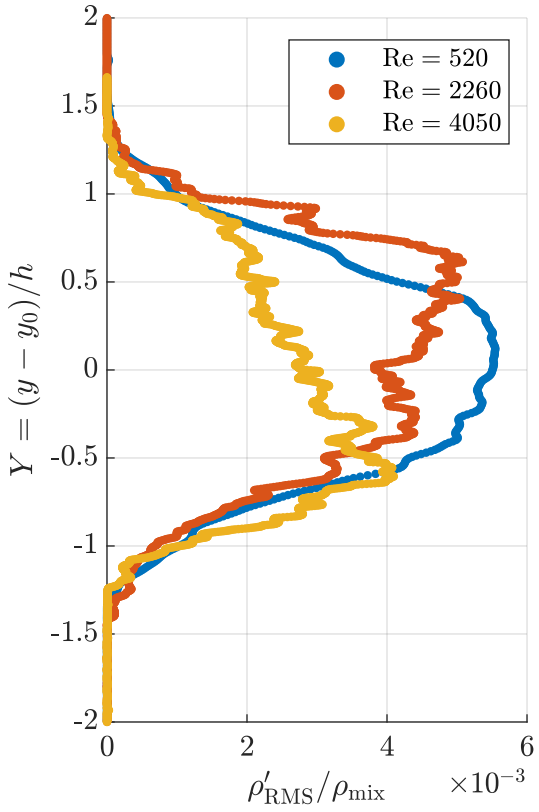


Figure 3.5: Normalized profiles of the root-mean-square density fluctuation for the three Reynolds numbers tested.

### 3.2.2 Volume Fraction Probability Density Function

When studying statistical quantities, it is often useful to consider the probability density function (PDF) of the quantity of interest. For a continuous random variable, X, the probability density function of X, PDF(X) is defined such that the probability of finding a value of X between $a$ and $b$ can be found as $\mathrm{P}\{a \leq \mathrm{X} \leq b\} = \int_a^b \mathrm{PDF(X)}$. For a finite set of continuous data, the PDF can be estimated by binning the data into a histogram and normalizing the bin counts so that the area under the histogram curve is unity. The PDF estimates for $f_1$ at five different normalized coordinate $Y$ locations for the three Reynolds numbers tested is presented in Figure 3.6. Here, the histograms were computed with a bin width of 0.05. The edges of the mixing region, $Y = \pm 1$, are characterized by the presence of only pure fluid with $f_1 = 0$ or

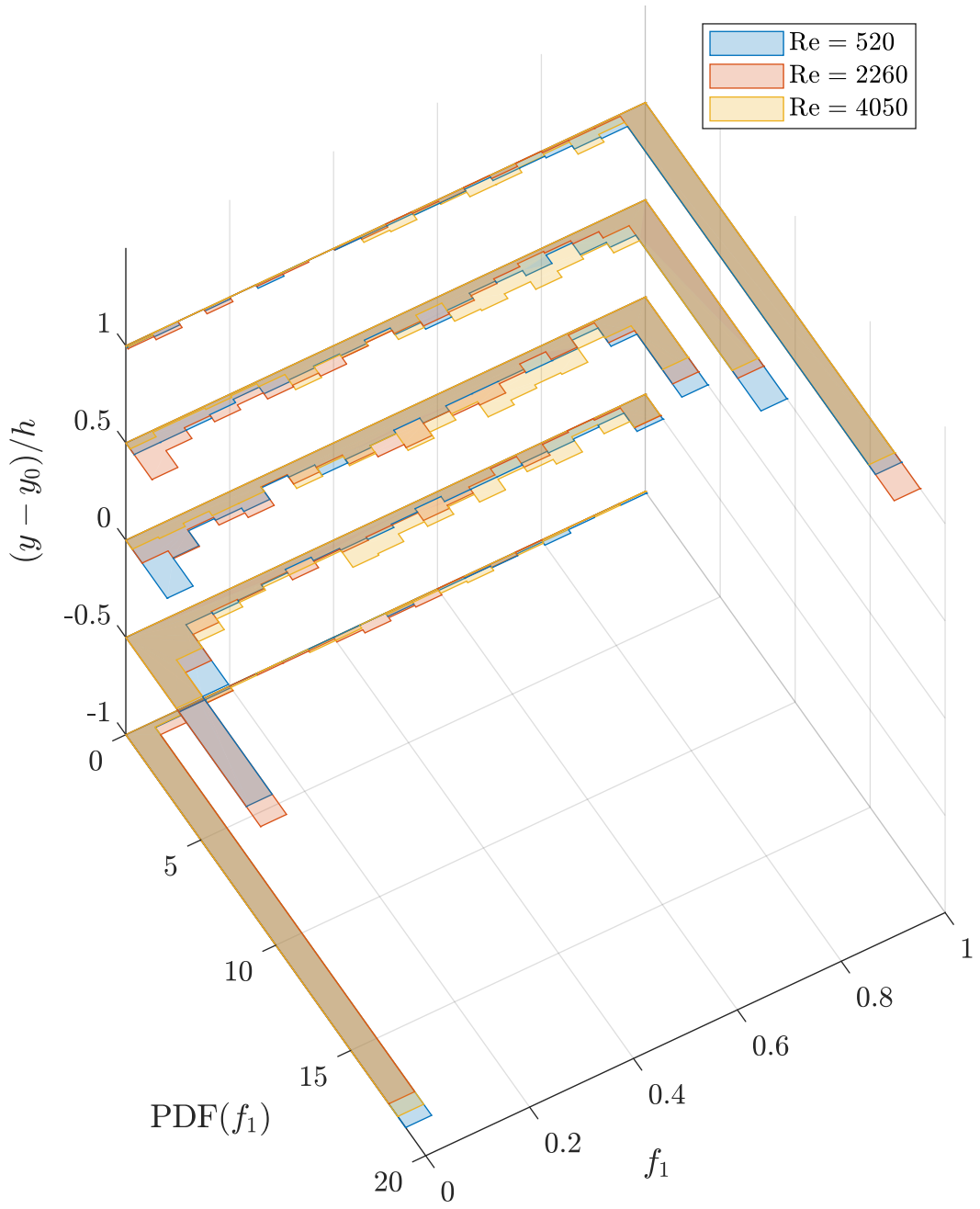


Figure 3.6: Probability density functions of the volume fraction of the heavy gas, $f_1$, for the three Reynolds numbers tested at 5 normalized $y$-coordinate locations.

Table 3.3: Calculations of the Richardson number for the three Reynolds number experiments performed.

| Re | Ri |
|---|---|
| 520 | 18.7 |
| 2260 | 9.5 |
| 4050 | 26.9 |

1, regardless of Reynolds number. However, as we move into the core of the mixing region, the PDFs show fewer counts corresponding to pure fluid, and a somewhat uniform distribution of fluid with $0.2 \leq f_1 \leq 0.8$. In the core of the flow, the counts of pure fluid decrease with increasing Reynolds number, indicating a greater degree of mixedness and fewer packets of pure fluid as the instability development time increases.

### 3.3 PIV Results

In this section, we present the results of the PIV measurements. As discussed in Section 2.2, the resolution of the PIV diagnostic is approximately four times coarser than the LIF diagnostic. For combined PIV/LIF results, we interpolate the computed PIV vectors onto the LIF grid. However, in this section, we present the PIV results at their original resolution, with no interpolation or filtering.

The mean $x$-direction and $y$-direction velocities, $\overline{u}$ and $\overline{v}$, respectively for the three Reynolds numbers tested are presented in Figure 3.7 along with the associated uncertainty bands. As seen in the figure, the experiments conducted were not completely free from shear between the upper and lower streams. To quantify the relative strength of this shear when compared to the strength of the buoyant forces, it is customary to compute the Richardson number, Ri, of the flow, where

$$\mathrm{Ri} = \frac{g}{\rho} \frac{(d\rho/dy)}{(du/dy)^2}. \tag{3.4}$$

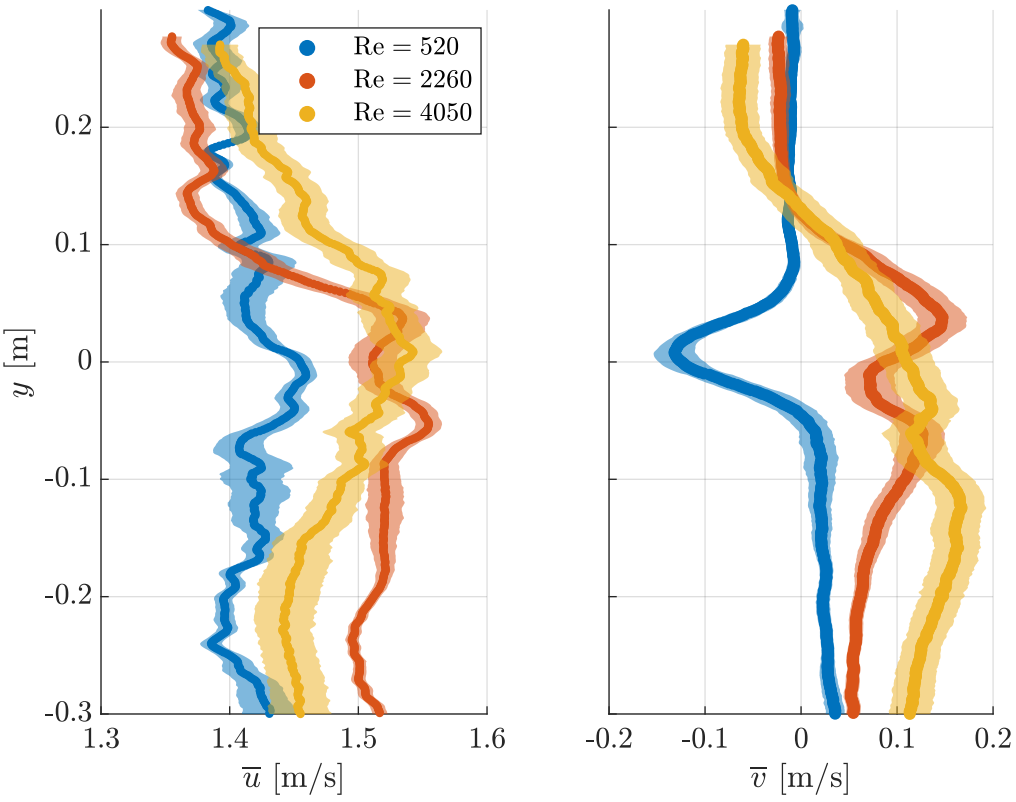


Figure 3.7: Profiles of the mean horizontal and vertical velocity, $u$ and $v$, respectively, together with the associated uncertainty.

Ri is the ratio of the strength of buoyant forces to shear forces in the flow. For Ri $\geq 1$, it is generally understood that the flow is dominated by buoyant forces and that shear has little impact on the development of the flow. In other RTI experiments [77], the above definition for Ri has been discretized in terms of the mixing width of the instability, the Atwood number, and shear velocity difference, $\Delta U$, to arrive at the definition

$$\text{Ri} \approx \frac{2g\mathcal{A}h}{(\Delta U)^2}. \tag{3.5}$$

The evaluation of this discretized Richardson number for the three experiments performed is presented in Table 3.3. Ri is found to be on the order of 10 or greater for all three experiments, leading us to believe that shear had negligible impact on the development of the flow.

### 3.3.1 Root Mean Square of Velocity Fluctuations

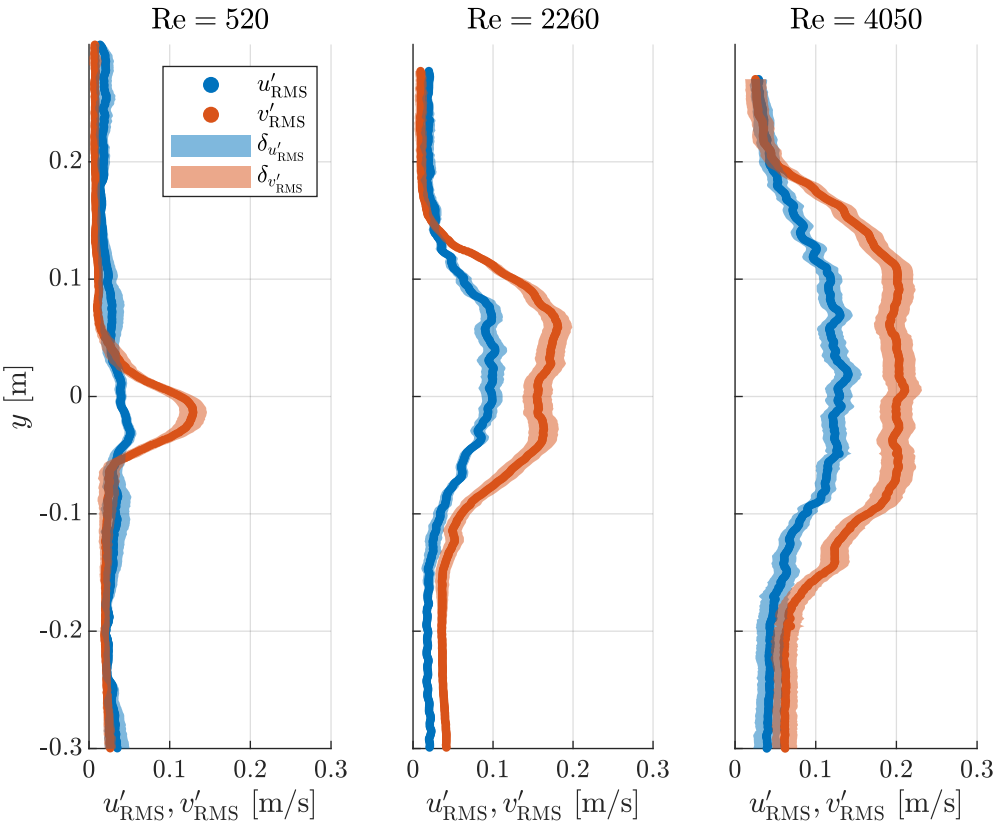


Figure 3.8: Profiles of the root mean square of the fluctuation of the horizontal and vertical velocity components, $u'_{\mathrm{RMS}}$ and $v'_{\mathrm{RMS}}$, together with the associated uncertainty in the statistic.

One of the most important measures of the strength of the underlying turbulence is the root mean square (RMS) of the fluctuating velocity components, $u'_{\mathrm{RMS}} = \overline{u'u'}^{1/2}$. The RMS horizontal and vertical velocity profiles are presented in Figure 3.8, together with the uncertainty bands for the statistic. In general, $u'_{\mathrm{RMS}}$ and $v'_{\mathrm{RMS}}$ have profiles which are Gaussian-like, peaking near the center of the mixing region and gradually declining towards zero at the edges. However, they differ from a Gaussian profile in the fact that they are flat through the core of the mixing region. This seems to imply that the turbulence is of unvarying strength through the majority of the mixing region, except at the edges. In general, the strength of vertical velocity fluctuations is double

that of horizontal ones. The exception is for Re = 520, where the horizontal velocity fluctuations are so small as to not be distinguishable from the velocity fluctuations of the free-stream. Lastly, it should be noted that the velocity fluctuations of the free-stream in the bottom-stream show significant anisotropy, with $u'_{\mathrm{RMS}} \neq v'_{\mathrm{RMS}}$. This may be a residual impact of the buoyancy-driven mixing that occurs in the settling section of the gas tunnel when the light-gas is injected into the flow.

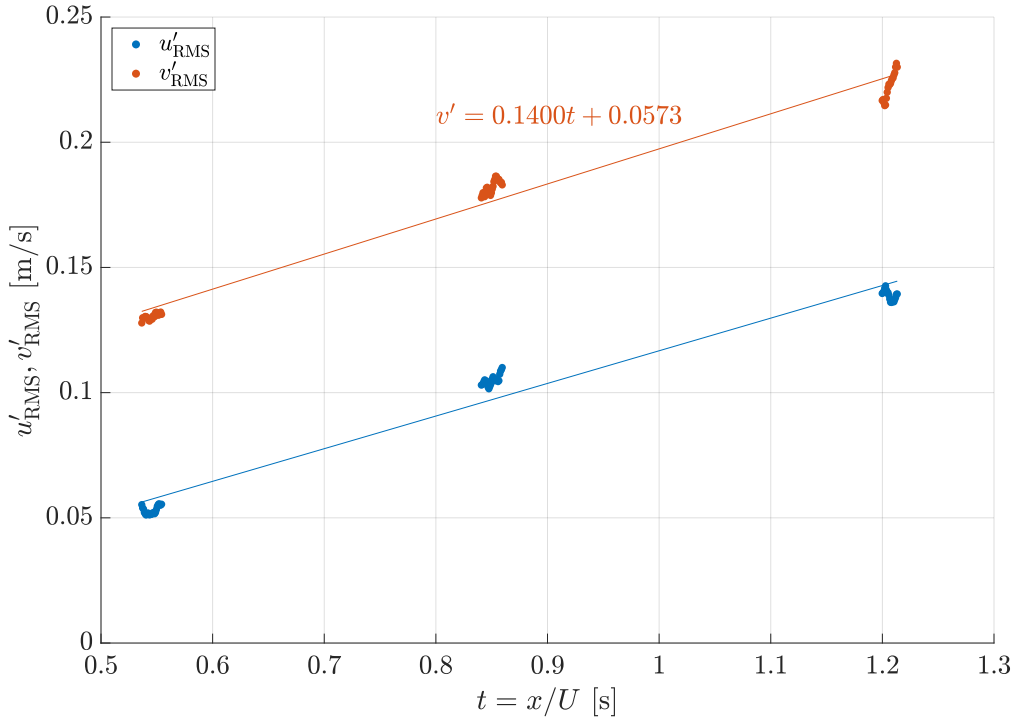


Figure 3.9: The maximum $u'_{\mathrm{RMS}}$ and $v'_{\mathrm{RMS}}$ at each downstream location $x$ measured, against the instability development time for that $x$ location, $t$. The line through the $v'_{\mathrm{RMS}}$ points describes the least-square linear fit.

In the fully-turbulent regime, the maximum fluctuations of velocity in the vertical direction are the leading contributor to the mixing growth rate. As a result, the community frequently considers their equivalence, so that $v'_{\mathrm{RMS}} = \frac{\mathrm{d}h}{\mathrm{d}t}$. By substituting the equation for the self-similar growth rate, equation 1.7 in for $h$, a linear equation

for $v'_{\mathrm{RMS}}$ in terms of the instability development time can be formed as

$$v'_{\mathrm{RMS}} = 2\alpha \mathcal{A} g t. \tag{3.6}$$

Figure 3.9 displays the maximum horizontal and vertical RMS velocity at the three Reynolds numbers, and hence, three instability development times studied. A least-squares linear fit has been applied to $v'_{\mathrm{RMS}}$ to show the approximately linear growth of this quantity with time, and the linear equation is displayed on the figure. As a result of equation 3.6, the slope of this line should be equal to $2\alpha \mathcal{A} g$. If the Atwood number is selected to be the average Atwood number of the three experiments performed, we arrive at an estimate for the growth rate parameter, $\alpha = 0.071$.

Because the vertical RMS velocity fluctuation can be used to replace the instability growth rate, it is also used to compute the Reynolds number of the flow. In equation 1.8, the length-scale of the flow is chosen to be the total extent of the mixing width, $2h$, and the velocity scale is chosen to be the vertical RMS velocity fluctuation $v'_{\mathrm{RMS}}$. Together with the mixture viscosity, $\nu$, this creates an equation for the Reynolds number, equation 3.7. This is the equation for Reynolds number that is used to derive the Reynolds numbers presented throughout this work.

$$\mathrm{Re} = \mathrm{Re}_{v'_{\mathrm{RMS}}} = \frac{2h v'_{\mathrm{RMS}}}{\nu} \tag{3.7}$$

### 3.3.2 Self-Similarity of the Velocity Profiles

One of the primary tests to determine if a flow has entered into a fully-turbulent state is to determine if it displays self-similarity in profiles of the velocity and density statistics. In order to verify this, we follow the technique of Ramaprabhu and Andrews [71] and Akula and Ranjan [76] by normalizing the profiles of the RMS horizontal and vertical velocity fluctuations with the terminal bubble velocity, $v_\infty$. As was

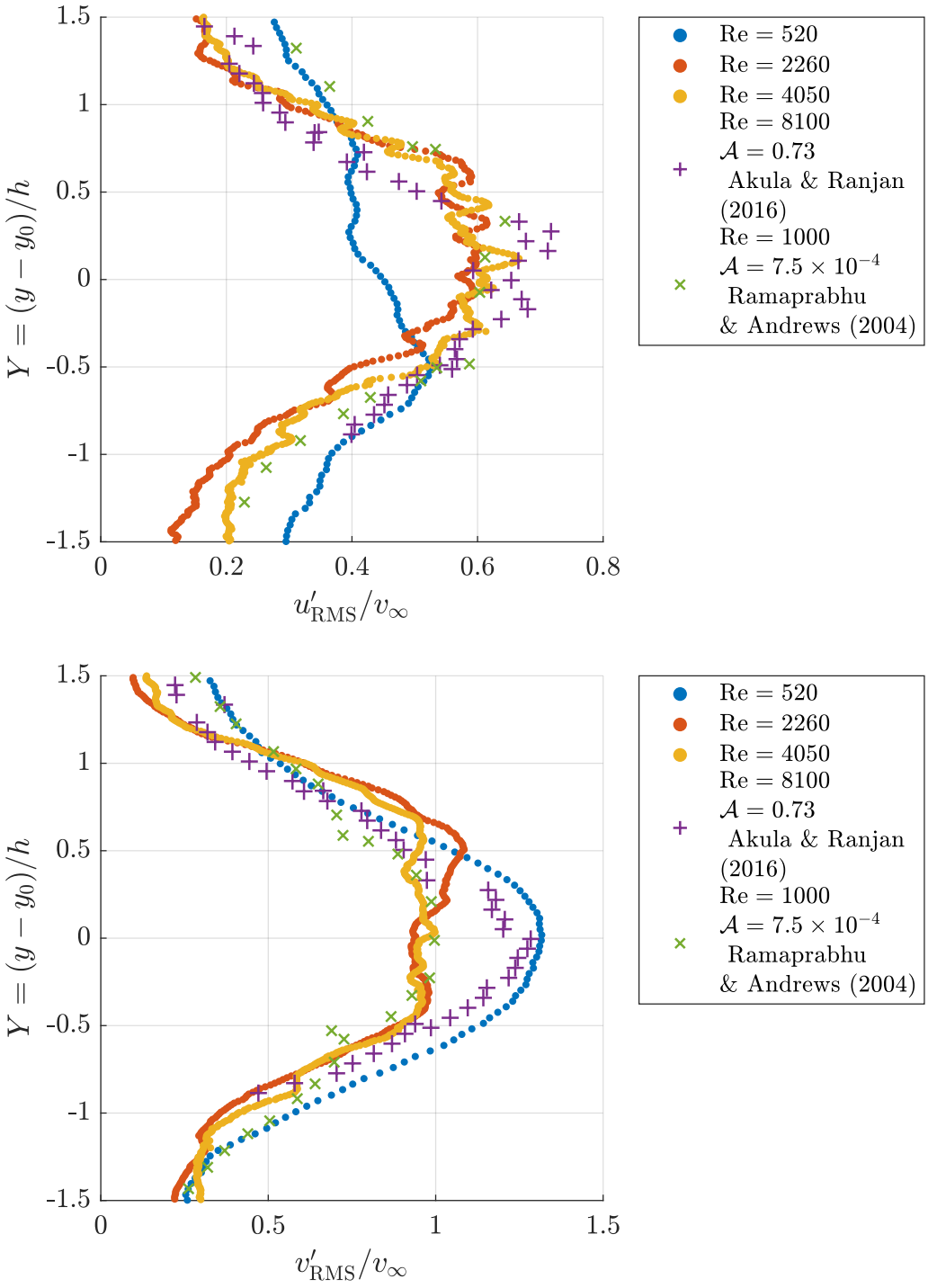


Figure 3.10: Profiles of the RMS horizontal and vertical velocity fluctuations, normalized by the Goncharov bubble velocity. For comparison, the normalized profiles from Ramaprabhu and Andrews [71] and Akula and Ranjan [76] are also presented.

discussed in Section 1.4.1, many models for the terminal bubble velocity have been found and applied to compare RTI experiments. However, we choose to use the model of Goncharov [28], which was the first to seriously consider the effect of variable Atwood number on the dynamics of the bubble. The equation for the bubble velocity is given in equation 1.9. In order to use this model, the wavelength of the instability must be known. In the fully-turbulent regime, memory of the initial conditions is lost and the only length-scale that persists is the mixing width of the instability. In order to use equation 1.9, we make the assumption that the instability wavelength is equal to the half-width of the mixing region so that $\lambda = h$.

Figure 3.10 shows the profiles of the RMS horizontal and vertical velocity fluctuations when normalized by the Goncharov terminal bubble velocity. The figure shows good self-similar collapse for the Re = 2260 and Re = 4050 cases. The Re = 520 still has not reached the fully-turbulent state, and fails to collapse as a result. The plots show that $v'_{\mathrm{RMS}}/v_\infty$ has a peak of unity, suggesting that the terminal bubble velocity is an excellent scaling for this velocity. In addition, $u'_{\mathrm{RMS}}/v_\infty$ has a peak of around 0.6, illustrating the anisotropic nature of the flow in the core of the mixing region. In order to further validate this scaling, we superimpose the normalized results of Ramaprabhu and Andrews [71], which were performed at lower Atwood number and much larger Schmidt number than the current experiment. The good agreement between the two data sets implies that this scaling is insensitive to the strength of molecular diffusion and to Atwood number in the case of Boussinesq flows. To compare to a non-Boussinesq flow, we also superimpose the normalized results of Akula and Ranjan [76]. This experiment shows good collapse for the $u'_{\mathrm{RMS}}$ scaling, but not for the $v'_{\mathrm{RMS}}$ scaling. Akula and Ranjan [76] had similarly found that vertical velocity fluctuations were larger than the terminal bubble velocity at large Atwood numbers, potentially resulting from the large velocity of the spike, which is asymmetric relative to the bubble at larger Atwood number. Goncharov [28] also cited himself the

limitations of his model to correctly quantify the velocity of the falling spike.

### 3.3.3 Skewness and Kurtosis

The study of the PDFs of the velocity fluctuations can be useful in describing the behavior of the flow. Two statistical quantities that are frequently used to describe the shape and behavior of a PDF are the skewness, $S$, and kurtosis, $K$, defined by equations 3.8 and 3.9.

$$S_\phi = \frac{\overline{\phi'^3}}{\sigma_\phi^3} \tag{3.8}$$

$$K_\phi = \frac{\overline{\phi'^4}}{\sigma_\phi^4} \tag{3.9}$$

where $\phi'$ are the fluctuations of $\phi$ from the mean and $\sigma_\phi$ is the standard deviation of the sample set of $\phi$. Skewness is a measure of the bias in the PDF to one side. Positive skew indicates that the PDF exhibits a long and fat tail towards values that are greater than the mean, whereas negative skew indicates that the PDF exhibits a long and fat tail towards values that are lesser than the mean. For a symmetric PDF, such as the PDF of the normal distribution, the skewness is zero. Kurtosis is frequently described as a measure of the "peakedness" of the PDF, though it more accurately represents the "tailed-ness" of the distribution or the number of outliers. Small values of kurtosis typically represent a PDF that is flatter and is short-tailed, such as the uniform distribution. Larger values of kurtosis represent a PDF that exhibits a strong peak and long tails. The kurtosis of any univariate normal distribution is 3, which often serves as a comparison benchmark for other PDFs.

Figure 3.11 shows the profiles of the skewness and kurtosis for the horizontal and vertical velocity fluctuations for the three experiments tested. The skewness profile shows that the PDF of $u'$ remains mostly symmetrical across the entire mixing layer for all of the Reynolds numbers tested, but that $v'$ exhibits strong skewness near the

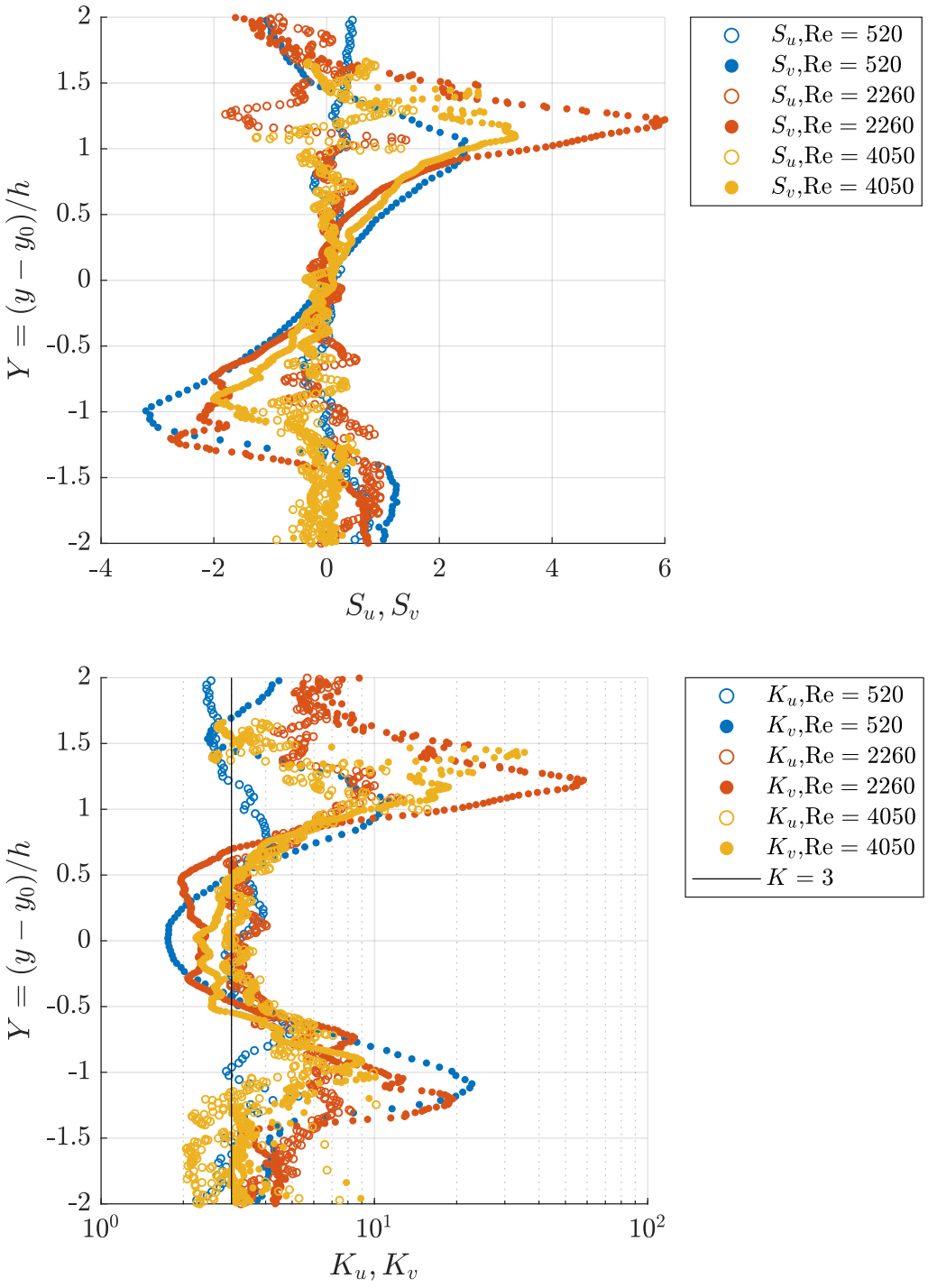


Figure 3.11: Profiles of the skewness and kurtosis of the horizontal and vertical velocity fluctuations for the three Reynolds numbers tested.

edges of the mixing width. Specifically, $v'$ shows positive skew on the bubble side and negative skew on the spike side. This indicates that, on the bubble side, there is a

larger tail of positive velocities than negative velocities. Because positive velocities correspond to the rising bubbles, this indicates that there is a greater variation in possible bubble velocities in this region, but a uniform variation of spike velocities. The opposite applies to the spike side.

The kurtosis profile shows that there is significant difference in the PDF shape between the core of the mixing region and the edges. In the core of the mixing region, $u'$ has kurtosis equal to 3 for all Reynolds numbers tested, showing that it has a strongly Gaussian distribution. However, $v'$ has a kurtosis much smaller than 3, indicating that the PDF is mostly flat and contains small weight in the outlier regions. This implies a uniform probability distribution over a narrow range of possible $v'$. At the edges of the mixing region, both $u'$ and $v'$ have kurtosis much greater than 3, suggesting that there is a greater degree of outliers in these regions. This may be because of the presence of the interface in this region, causing for there to be a wide range of possible values for both the horizontal and vertical velocities.

### 3.3.4 Anisotropy Tensor

Some of the most integral theories concerning turbulence, proposed by Kolmogorov [131] assume that the turbulence is locally isotropic: in other words, that at the smallest scales of the flow, the flow has no recognition of the large scale boundary conditions and therefore, has no preference of direction. Many turbulent flows are anisotropic, with even the smallest scales of the flow showing a directional preference. A measure frequently used to describe the degree of anisotropy is the anisotropy tensor, $b_{ij}$, which is defined by equation 3.10.

$$b_{ij} = \frac{\overline{u_i' u_j'}}{\overline{u_k' u_k'}} - \frac{\delta_{ij}}{3} \tag{3.10}$$

where $u_i'$ is the velocity fluctuation vector, $\delta_{ij}$ is the Kronecker delta, and repeated subscripts imply Einstein summation convention. $b_{ij}$ may vary from a minimum value of $-1/3$, indicating that none of the energy of the turbulence is contained in that fluctuating component, to a maximum value of $2/3$, indicating that all of the energy of the turbulence is contained in that fluctuating component. In an isotropic flow, all of the components of the anisotropy tensor are zero. For the planar two-component PIV measurement recorded here, we do not have the ability to measure velocities in the plane normal direction, $w$. To replace this term in equation 3.10, we utilize an assumption frequently made in turbulent flows that $w' \approx u'$ [42, 71]. This assumption is only valid at large Reynolds numbers.

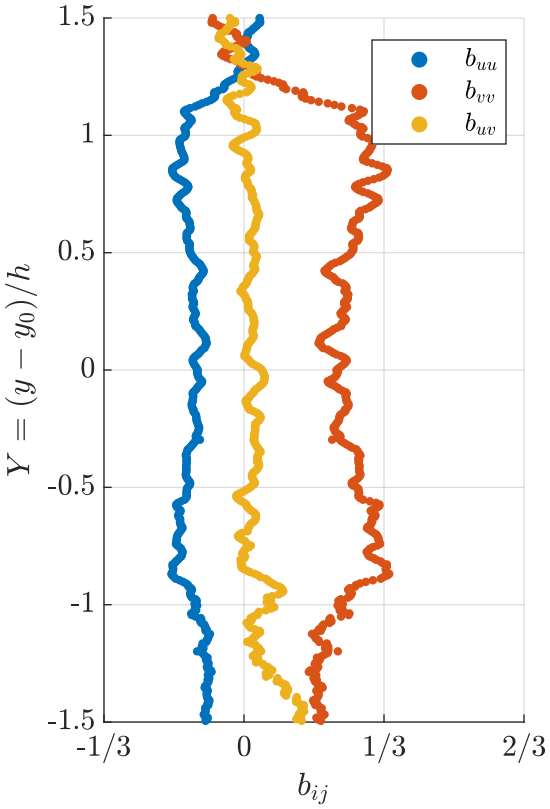


Figure 3.12: Profiles of the components of the anisotropy tensor, $b_{ij}$, for the Re = 4050 experimental case.

Figure 3.12 shows the profiles of the anisotropy tensor components $b_{uu}$, $b_{vv}$, and

$b_{uv}$ for the Re = 4050 experiment. The profile shows that there is nearly no energy in the cross-correlation component, $b_{uv}$ over the entire mixing width, indicating that the horizontal and vertical velocity fluctuations are mostly uncorrelated. Overall, both $b_{uu}$ and $b_{vv}$ are nearly constant across the entire mixing region, with $b_{uu} \approx -1/6$ and $b_{vv} \approx 1/3$. This indicates that the flow displays a strong, but nearly constant anisotropy throughout the entire mixing region.

## 3.4 Simultaneous PIV/LIF Results

### 3.4.1 Turbulent Mass Flux

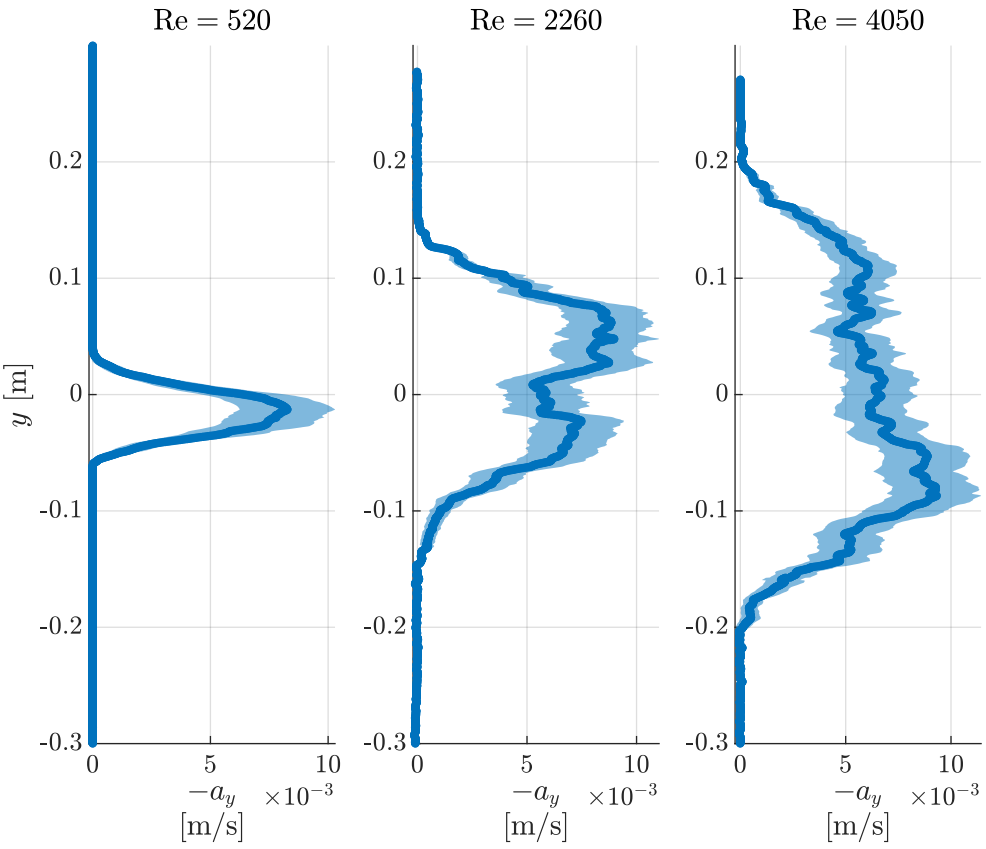


Figure 3.13: Profiles of the negative vertical turbulent mass flux, $a_y$, together with the associated uncertainty in the statistic.

By utilizing the simultaneous results of our PIV/LIF diagnostic, we are able to provide field measurements of cross-correlations of the density and velocity. This

is necessary for the computation of the turbulent mass flux, $a_i$. $a_i$ is one of the quantities modeled with a transport equation in the BHR model, as well a component of the production term in the variable-density turbulent kinetic energy equation, so its accurate computation is vital to the development of accurate predictive models. It has dimensions of Length/Time, so it is often normalized with velocity scalings. The profiles for $a_y = \overline{\rho' v'}/\overline{\rho}$ for the three Reynolds numbers tested are shown in Figure 3.13, along with the associated uncertainty in the statistic. The profile of $a_y$ grows in width at a similar rate to the velocity flucutations. At Re = 520 and Re = 2260, the profile is roughly symmetric around the centerline of the flow. However, at Re = 4050, a clear asymmetry is seen between the spike side and bubble side, with the spike side having greater turbulent mass flux. Even though the Atwood number of the current experiment is small, and the flow should be relatively Boussinesq, it is possible that there is some asymmetry developing in the shape of the spike, resulting in an increase in turbulent mass flux on the spike side. Through conditional statistics, separating the impact of the bubble and the spike, Akula and Ranjan [76] also found that, at large Atwood numbers, asymmetry led to the increased contribution of the spike to the development of turbulent mass flux.

To further understand the turbulent mass flux, the PDF of the density-velocity correlation, $\rho' v'$ is presented in Figure 3.14. There is good collapse in the PDF between the two Reynolds numbers shown. Both PDFs show a significant peak at zero, with only a small probability of positive correlation. They exhibit long tails which gradually descend into negative correlation values. When compared to the results of Akula and Ranjan [76] at larger Atwood number, the slope of the negative correlation tail is more gradual and extends to more negative values. Beyond these discrepancies, there is good agreement between the PDF at both Atwood numbers.

Ristorcelli and Clark [34] suggest an appropriate velocity scale for RTI flows in the self-similar regime is $U_{RC} = \sqrt{\mathcal{A}gh}$. This velocity can be derived from dimensional

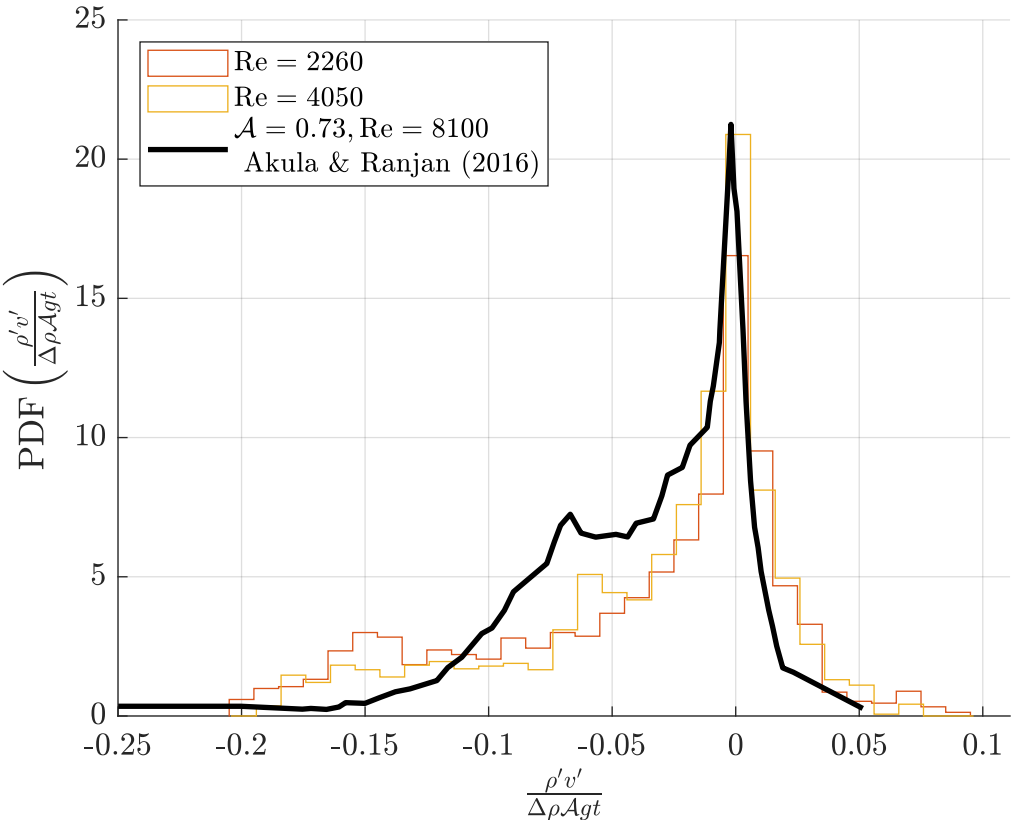


Figure 3.14: The probability density function of the density-velocity correlation, $\rho' v'$, after normalization for the Re = 2260 and Re = 4050 cases, evaluated at $Y = 0$. To compare, the density-velocity correlation using the same normalization presented by Akula and Ranjan [76] is shown

analysis, recognizing that in the self-similar regime, the memory of the initial condition of the flow has been lost and the only remaining length scale is the mixing width, $h$. In order to compare results between RANS models and DNS, Schwarzkopf et al. [109] has frequently used $U_{RC}$ as a normalization parameter for velocity, but using the integral mixing width, $h_f$, instead of the mixing half-width, $h$ as the pertinent length scale. This results in a velocity scale in terms of the integral mixing width, $U_{h_f} = \sqrt{\mathcal{A} g h_f}$.

Profiles of the turbulent mass flux, normalized against $U_{h_f}$ are presented in Figure 3.15. There seems to be an acceptable degree of collapse in the $a_y$ profile at large Reynolds number, except for a large deviation in the Re = 2260 profile between

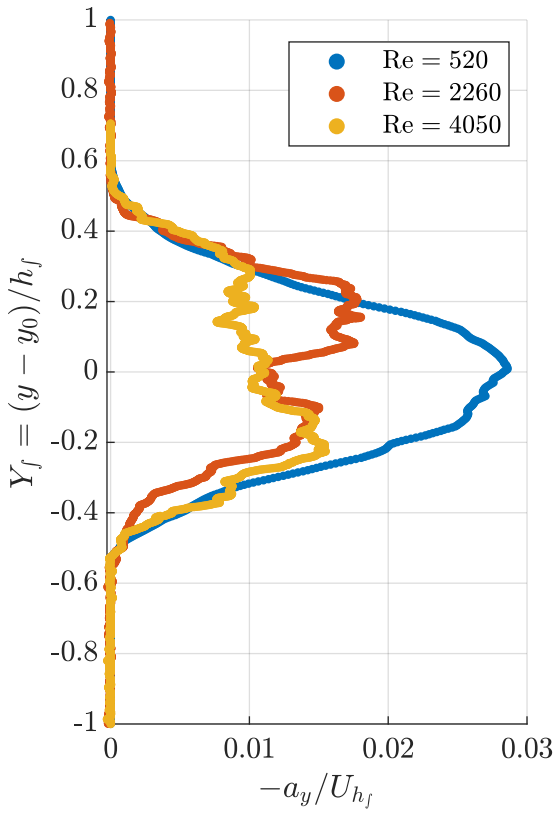


Figure 3.15: Profiles of the negative vertical turbulent mass flux, $a_y$, normalized by the self-similar velocity scale, $U_{h_f}^2$.

$0 \leq Y_f \leq 0.3$. This may be due to the deviations in the overall volume fraction profile at this Reynolds number in the same spatial region. The peak for both large Reynolds number profiles occurs at a value of $a_y/U_{h_f} \approx 0.015$ to 0.02. This is much smaller than the value of $a_y/U_{h_f} \approx 0.05$ to 0.06 found using BHR TLSM RANS simulations by Schwarzkopf et al. [109], or the similar values found using DNS by Cabot and Cook [110]. Both of these simulations took place at larger Atwood number, $\mathcal{A} = 0.5$, compared to the present experiment. Similarly to how the profiles of the RMS velocity fluctuations did not collapse appropriately using the data of Akula and Ranjan [76] at $\mathcal{A} = 0.73$, it could be that the scaling used here is also inadequate at capturing variations in the peak value of the $a_y$ profile between Boussinesq and non-Boussinesq cases.

### 3.4.2 Reynolds Stress

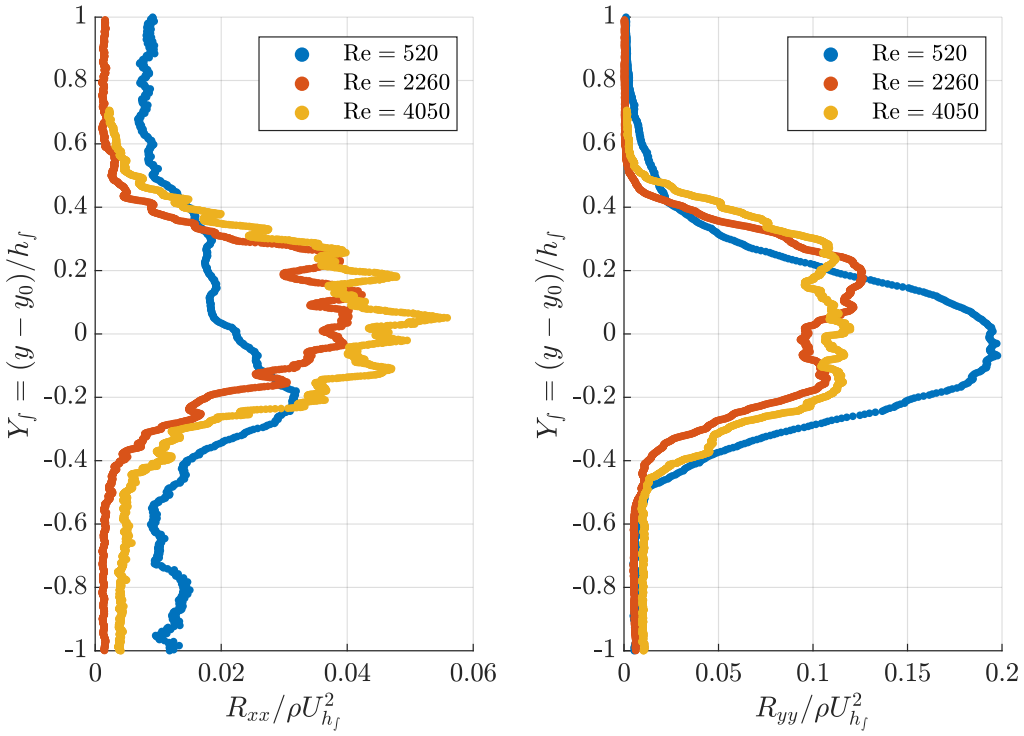


Figure 3.16: Profiles of the Reynolds stress components, $R_{xx}$ and $R_{yy}$, normalized by the mean density profile and the self-similar velocity, $U_{h_f}$, for the three Reynolds numbers tested

In addition to the turbulent mass flux, we are able to compute the Reynolds Stress components for the compressible RTI flow, $R_{ij} = \overline{\rho u_i'' u_j''}$, where $u_i'' = u_i - \frac{\overline{\rho u_i}}{\overline{\rho}}$ is the Favre-average fluctuating component. Figure 3.16 shows the profiles of $R_{xx}$ and $R_{yy}$, normalized by the mean density profile and $U_{h_f}^2$. Overall, the profiles show good collapse, with the peak values of $R_{xx}/\rho U_{h_f}^2 \approx 0.05$ and $R_{yy}/\rho U_{h_f}^2 \approx 0.12$. When compared to the peaks of the normalized Reynolds stress profiles presented by Schwarzkopf et al. [109] of $R_{xx}/\rho U_{h_f}^2 \approx 0.025$ and $R_{yy}/\rho U_{h_f}^2 \approx 0.075$, we find that the Reynolds stresses are significantly higher, especially for $R_{xx}$. Because $R_{xx}$ is primarily linked to horizontal velocity fluctuations in the flow, this may be an indicator of the impact of free-stream turbulence and small variations in the mean convective velocity

of the gas tunnel facility leading to an increase in $u'$.

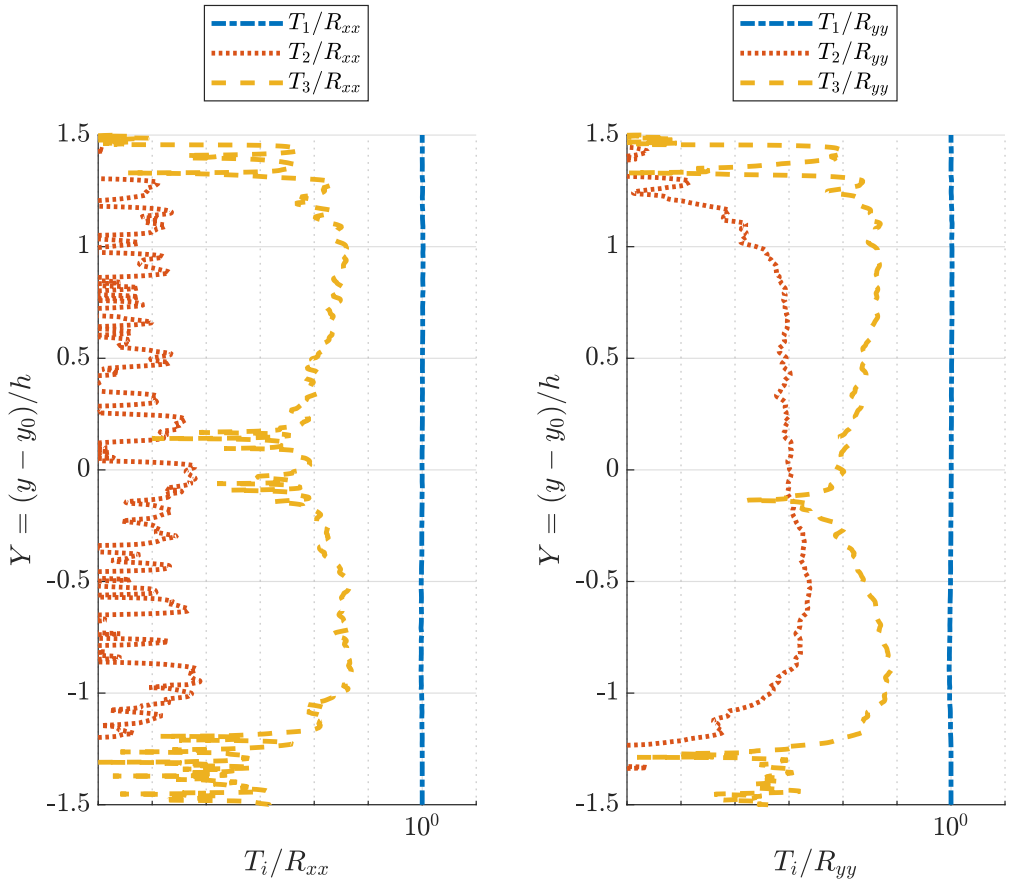


Figure 3.17: Profiles of the relative contribution of terms in the Reynolds Stress decomposition, T1, T2, and T3, normalized by the total Reynolds stress, $R_{ij}$ for both $R_{xx}$ and $R_{yy}$. Profiles are presented from the Re = 4050 case.

Observation of the definition for Reynolds stress reveals that it is a triple correlation of density and velocity fluctuations, which can be challenging to handle in turbulence modeling. However, $R_{ij}$ can be decomposed into a set of three terms,

$$R_{ij} = \underbrace{\overline{\rho}\,\overline{u_i'u_j'}}_{\text{T1}} - \underbrace{\overline{\rho}\,\overline{a_i}\,\overline{a_j}}_{\text{T2}} + \underbrace{\overline{\rho' u_i' u_j'}}_{\text{T3}} \tag{3.11}$$

where only the final term, T3, involves a triple correlation. If it can be shown that T1 and T2 in equation 3.11 are the dominant terms in finding $R_{ij}$, then this can help

simplify models. Figure 3.17 shows profiles of the terms T1, T2, and T3 for both $R_{xx}$ and $R_{yy}$ at the largest Reynolds number tested. It is shown that T1 dominates, being at least one and a half orders of magnitude greater than any other terms. For $R_{xx}$, because of the small correlation between $\rho$ and $u$, Term T2, which is primarily dependent on the velocity-density correlation term, $a_x$, is nearly zero everywhere, and only T3 contributes significantly. For $R_{yy}$, Term T2 is more significant, being around three orders of magnitude smaller than the main component and one and a half orders of magnitude smaller than T3. At the edges of the mixing region where the density is mostly homogeneous, both T2 and T3 are completely negligible.

### 3.4.3 Turbulent Kinetic Energy

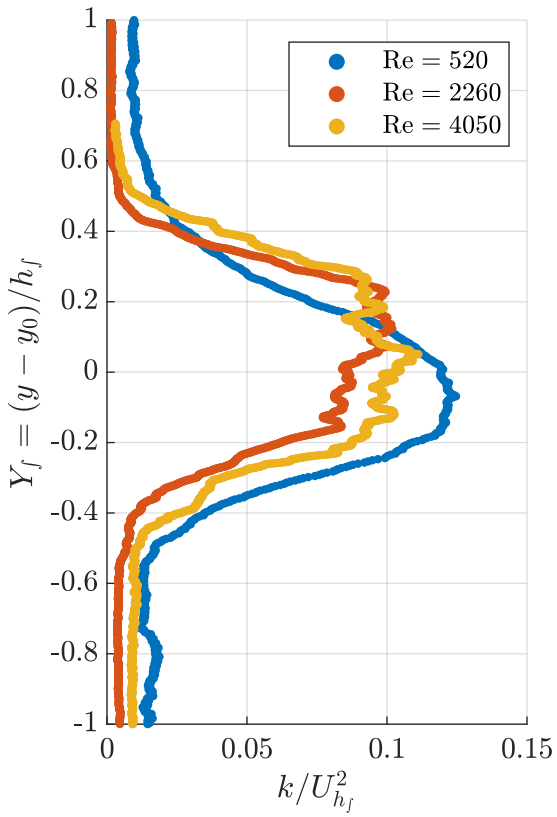


Figure 3.18: Profiles of the turbulent kinetic energy, $k$, normalized by the self-similar velocity scale, $U_{h_f}$.

From the Reynolds Stress tensor components, the turbulent kinetic energy can be computed by dividing half the trace of the tensor by the mean density, so that $k = \frac{1}{2\overline{\rho}}(R_{xx} + R_{yy} + R_{zz})$. We apply the same assumption here as was applied to the anisotropy tensor, that $R_{zz} = R_{xx}$ in the present flow. Figure 3.18 shows the profiles of the turbulent kinetic energy for the three Reynolds numbers tested, normalized by the square of the self-similar velocity scale, $U_{h_f}^2$. Again, reasonable collapse is found, with a peak normalized value of approximately $k/U_{h_f}^2 = 0.1$. However, there is again discrepancy between this peak value and that found by Schwarzkopf et al. [109] and by Cabot and Cook [110] ($k/U_{h_f}^2 = 0.06$).

### 3.4.4 Conditional Statistics

The simultaneous measurement of density and velocity allow us to obtain conditional statistics of the data to separate the relative impact of the bubble and spike structures. Antonia [132] describes the main methods of conditional sampling for shear-dominated turbulent flows and periodic flows. However, following the work of Banerjee et al. [75] and Akula and Ranjan [76], we apply a different type of conditional sampling that is focused on the density measurements.

Conditional statistics are evaluated for the largest Reynolds number tested, Re = 4050, at the mixing centerline, $Y = 0$. At this location, the mean density of the flow, $\overline{\rho}_{\text{mix}}$, is computed and the density fluctuation, $\rho'$, is found by subtracting $\overline{\rho}_{\text{mix}}$ from the instantaneous density measurements. At the mixing centerline, the mean density of the flow is approximately the average of the stream densities so that there are nearly equal components of both stream 1 and stream 2. This being the case, fluid which has a density fluctuation $\rho' > 0$ must have a density greater than $\overline{\rho}_{\text{mix}}$, and is comprised primarily of heavy spike fluid. The opposite must be true of fluid with a density fluctuation $\rho' < 0$. This fact allows us to use the sign of $\rho'$ as a condition to separate data associated with the bubble and the spike.

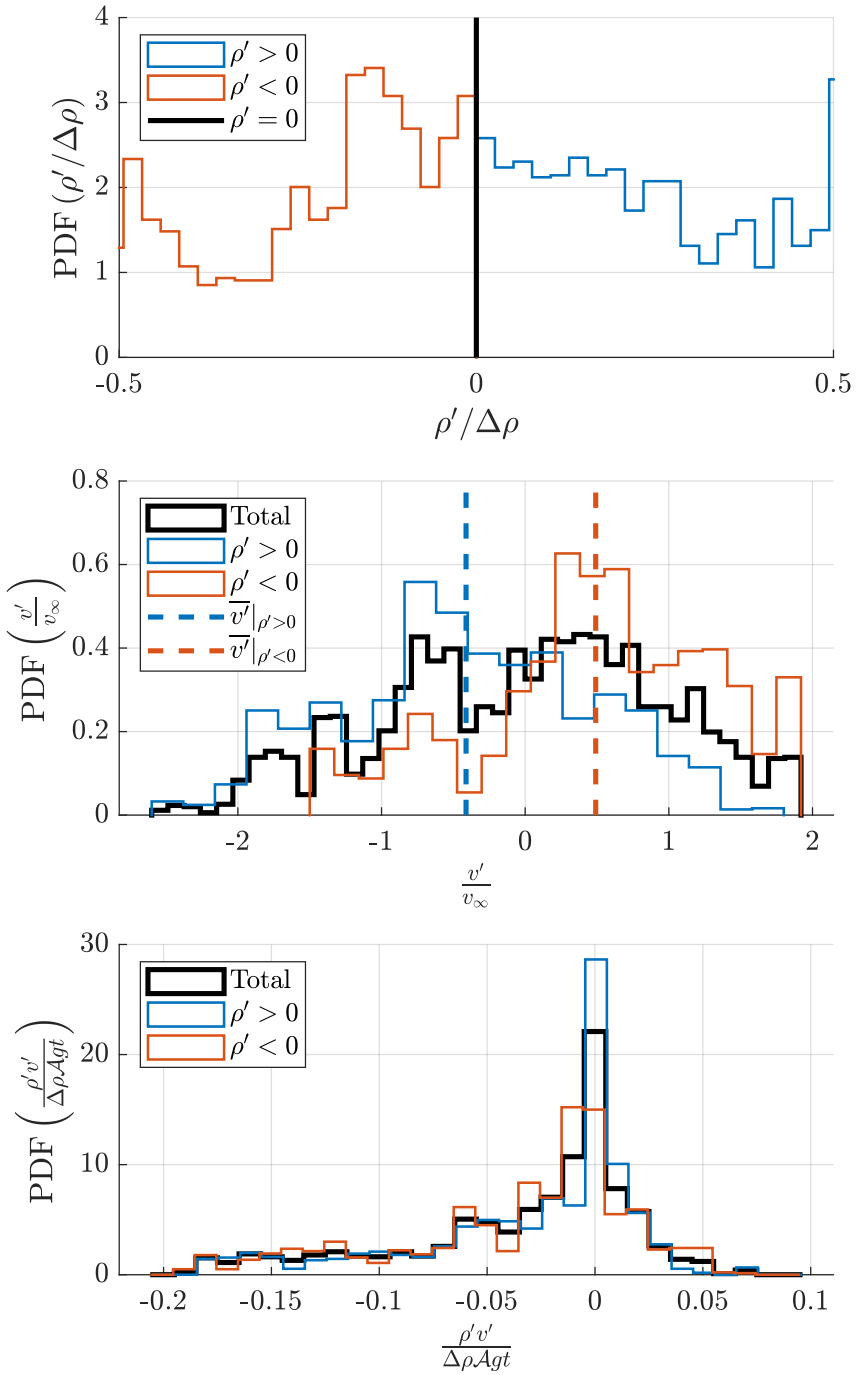


Figure 3.19: Probability density functions of the normalized density, velocity, and density-velocity correlation for the sampling conditions $\rho' < 0$ and $\rho' > 0$.

To illustrate the conditional averaging technique, Figure 3.19 presents the PDF of $\rho'$ with a dividing line separating $\rho' < 0$ and $\rho' > 0$. These conditions can be used to separate the vertical velocity fluctuations, $v'$, between the bubble and spike

contributions. The PDF of $v'$ normalized by the Goncharov bubble velocity is also presented in Figure 3.19. It is found that fluid associated with the spike, $\rho' > 0$ primarily has negative velocity fluctuations, with a mean velocity fluctuation being approximately half the bubble velocity. The opposite is true for bubble fluid, $\rho' < 0$. These results agree with the phenomenological view of RTI as the interpenetration of rising and falling fluid, where the direction of the fluid motion is inverse to its relative density. However, it is also clear from these PDFs that there is not one-to-one correspondence between positive density fluctuations and negative velocity fluctuations, nor the opposite for negative density fluctuations. The explanation given by Banerjee et al. [75] is that this is the result of spike fluid being entrained in vortical roll-ups by shear as the bubble and spike move past each other. This entrainment causes the spike fluid to rise with $v' > 0$. The same occurs for the low density bubbles. From observation of the shape of the velocity fluctuation PDF, we also see that the PDF is similar in shape between the two conditions tested. This symmetric nature is expected for this type of low Atwood number flow. To further illustrate the symmetry between the bubble and spike, the PDF of the density-velocity correlation, $\rho' v'$ after conditional separation is also shown in Figure 3.19. Again, both PDFs are shown to be nearly identical to each other and similar to the shape of the PDF found using conventional averaging techniques.

While the $\rho' < 0$ and $\rho' > 0$ conditions were useful in separating out the impact of the rising bubbles and falling spikes, it was clear that not all bubble fluid was associated with rising motion, nor spike fluid with falling motion. It may then be useful to condition the flow to separate the impact of rising and falling fluid. This can be accomplished by applying $v' > 0$ and $v' < 0$ as the conditional sampling criteria. Figure 3.20 shows the PDFs of $v'$, $\rho'$ and $\rho' v'$ when conditioned by the sign of the velocity fluctuation. The PDF of $\rho'$ shown in Figure 3.20 explains more clearly the impact of entrainment on modulating the velocity fluctuations of fluid of

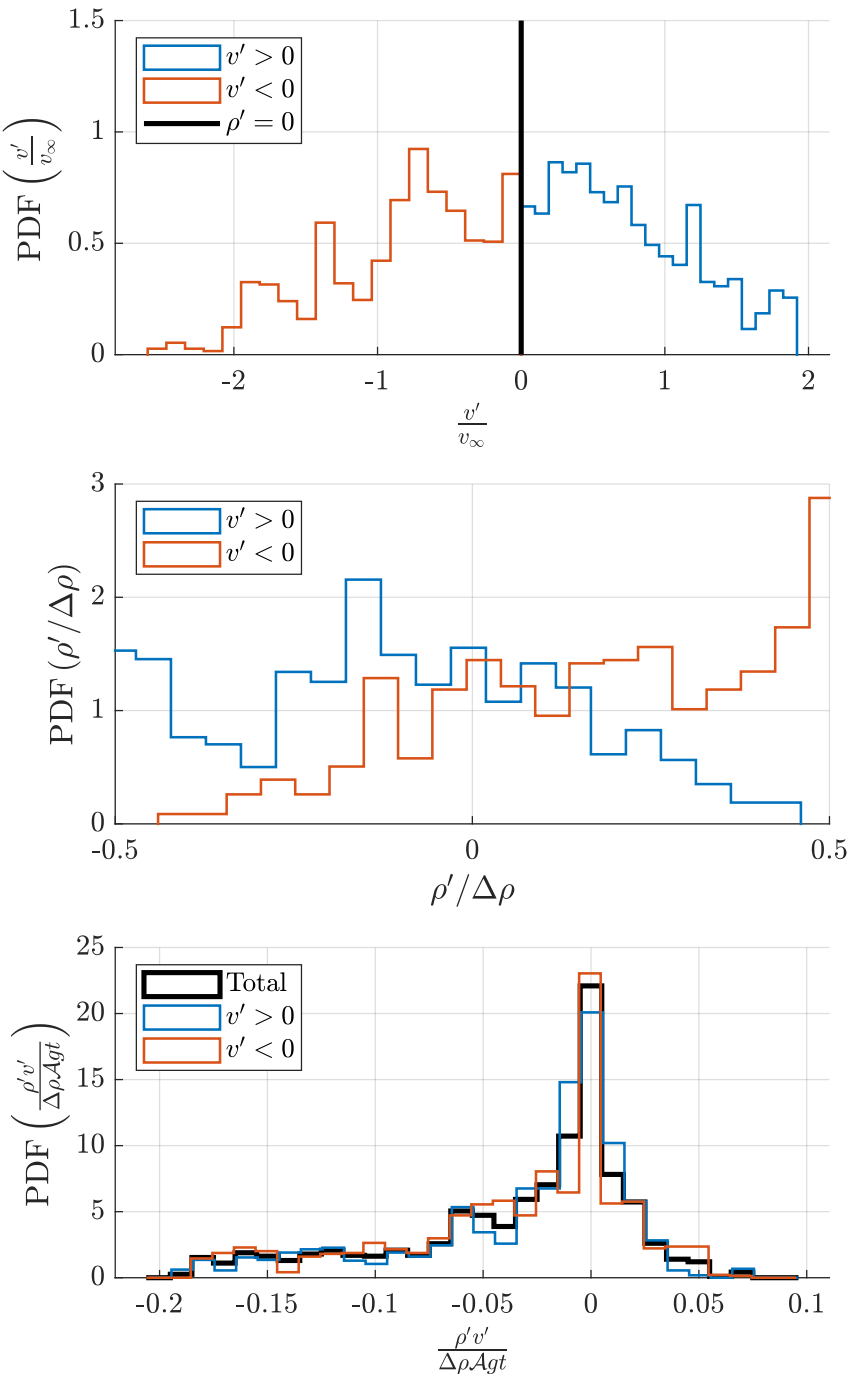


Figure 3.20: Probability density functions of the normalized velocity, density, and density-velocity correlation for the sampling conditions $v' < 0$ and $v' > 0$.

different densities. Both positive and negative velocity fluctuations can carry heavy and light fluid, but the probability of finding heavy fluid moving with positive velocity fluctuation decreases gradually as the density increases. The PDF of $\rho' v'$ in Figure

Table 3.4: Conditional statistics evaluated for the Re = 4050 case at $Y = 0$

| | $\rho' > 0$ | $\rho' < 0$ | $v' < 0$ | $v' > 0$ | Conventional |
|---|---|---|---|---|---|
| $\overline{f_1}$ | 0.7654 | 0.3056 | 0.6894 | 0.3952 | 0.5333 |
| $\overline{\rho}\,[\mathrm{kg\,m^{-3}}]$ | 1.1191 | 1.0255 | 1.1036 | 1.0437 | 1.0718 |
| $\overline{u'}\,[\mathrm{m\,s^{-1}}]$ | -0.0152 | 0.0149 | -0.0073 | 0.0065 | 0.0000 |
| $\overline{v'}\,[\mathrm{m\,s^{-1}}]$ | -0.0919 | 0.0902 | -0.1785 | 0.1580 | 0.0000 |
| $\rho'_{\mathrm{RMS}}\,[\mathrm{kg\,m^{-3}}]$ | 0.0558 | 0.0566 | 0.0567 | 0.0558 | 0.0562 |
| $u'_{\mathrm{RMS}}\,[\mathrm{m\,s^{-1}}]$ | 0.1279 | 0.1165 | 0.1368 | 0.1078 | 0.1223 |
| $v'_{\mathrm{RMS}}\,[\mathrm{m\,s^{-1}}]$ | 0.2074 | 0.1969 | 0.2155 | 0.1895 | 0.2022 |
| $\overline{\rho'v'}/\Delta\rho\mathcal{A}gt$ | -0.0332 | -0.0324 | -0.0349 | -0.0309 | -0.0328 |
| $a_y = \overline{\rho'v'}/\overline{\rho}\,[\mathrm{m\,s^{-1}}]$ | -0.0068 | -0.0072 | -0.0072 | -0.0067 | -0.0070 |
| $R_{xx} = \overline{\rho u''u''}\,[\mathrm{kg\,m^{-1}\,s^{-2}}]$ | 0.0183 | 0.0141 | 0.0206 | 0.0123 | 0.0162 |
| $R_{yy} = \overline{\rho v''v''}\,[\mathrm{kg\,m^{-1}\,s^{-2}}]$ | 0.0474 | 0.0404 | 0.0495 | 0.0388 | 0.0438 |
| $k\,[\mathrm{m^2\,s^{-2}}]$ | 0.0375 | 0.0334 | 0.0411 | 0.0303 | 0.0355 |

3.20 again shows the symmetric nature of this flow, with the PDFs looking nearly identical to the PDF of the total data set.

Finally, many of the statistics already presented in this work, such as Reynolds stress, turbulent mass flux, and others can be recalculated for the conditionally sampled data sets. Table 3.4 shows a summary of the measured statistics evaluated using conventional averaging methods, as well as with all four of the conditional sampling techniques that have been described. The general trend of comparison between opposite sampling methods, such as $\rho' > 0$ and $\rho' < 0$, is that the statistics are nearly equal, or else of equal magnitude and opposite sign. This again speaks to the symmetric nature of the bubbles and spikes in this low Atwood number flow. In comparing the conditional sampling techniques between the use of $\rho'$ and $v'$, the values of $\overline{f_1}$ show that the $v'$ sampling method results in fluid that is more homogeneous, with density closer to the mean density of the flow.

# CHAPTER 4
# MEASURES OF MOLECULAR MIXING

Many RTI phenomena involve miscible fluids which are able to mix at the molecular level at any volume fraction level. In these cases, as the RTI bubble and spike move past one another, unmixed fluid is entrained in the KHI rollups and other complex features that develop at the interface. The vorticity developed at the interface and the large scale motion of the instability then serves to stir the packets of unmixed fluid together, leading to an increase in the surface-area of the interface separating disparate fluids. The increasing surface-area strengthens the impact of diffusion across the interface, eventually leading to molecular mixing. In this chapter, we seek to provide measures of the molecular mixing in RTI flows. In addition, we quantify the rate of mixing and analyze the processes which lead to the increase of molecular mixing at different locations in the flow.

## 4.1 Molecular Mixing Parameter

Danckwerts [133] quantified molecular mixing as the degree of desegregation of the materials, $\theta$, defined by

$$\theta = 1 - \frac{B_0}{B_2} \tag{4.1}$$

$$B_0 = \lim_{T\to\infty} \frac{1}{T} \int_0^T \frac{(\rho - \overline{\rho})^2}{(\Delta\rho)^2} dt \tag{4.2}$$

$$B_2 = \overline{f_1}\,\overline{f_2}. \tag{4.3}$$

$\theta$ may take on a value between zero and unity, with zero representing unmixed fluids, and unity representing fluids that are completely molecularly mixed. This technique

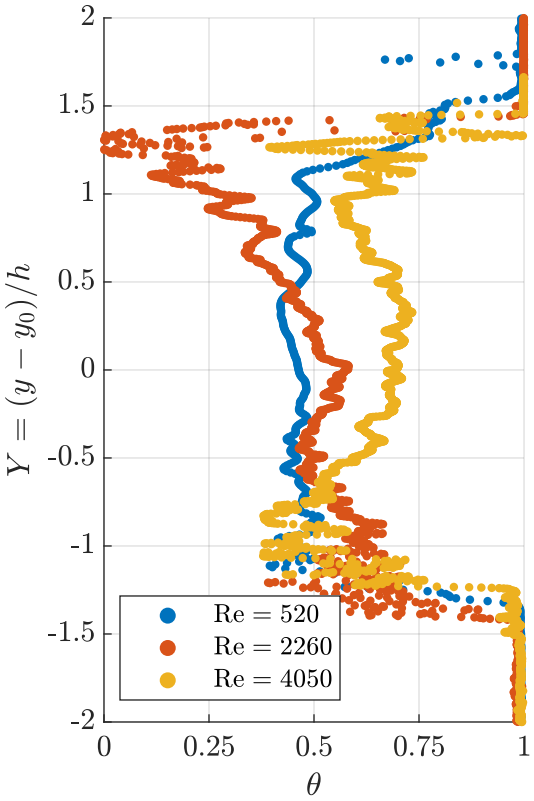


Figure 4.1: Profiles of the molecular mixing parameter, $\theta$, for the three Reynolds numbers tested.

was first used to study RTI mixing in simulations by Youngs [44], and the general trend found in experiments is that $\theta \to 0.75$ in the self-similar regime [40, 71, 75, 76].

The results of our LIF diagnostic equip us with measurements of the volume fraction and density across the mixing region, allowing us to easily compute $B_0$, $B_2$, and $\theta$. Figure 4.1 shows the profiles of mixing parameter, $\theta$, across the normalized $y$ coordinate for the three Reynolds numbers tested. The mixing parameter is seen to equal to approximately 0.5 at the edges of the mixing region for all experiments tested except for the bubble edge for the Re = 2260 experiment. This may be because of the re-acceleration of the bubble that is occurring at this Reynolds number, before mixing begins to break up the bubble shape. In the core of the mixing region, $\theta$ proceeds from a value of around 0.45 at the lowest Reynolds number to around 0.7

at the largest Reynolds number. This shows that the degree of desegregation in the core of the flow is approaching the expected asymptote of 0.75.

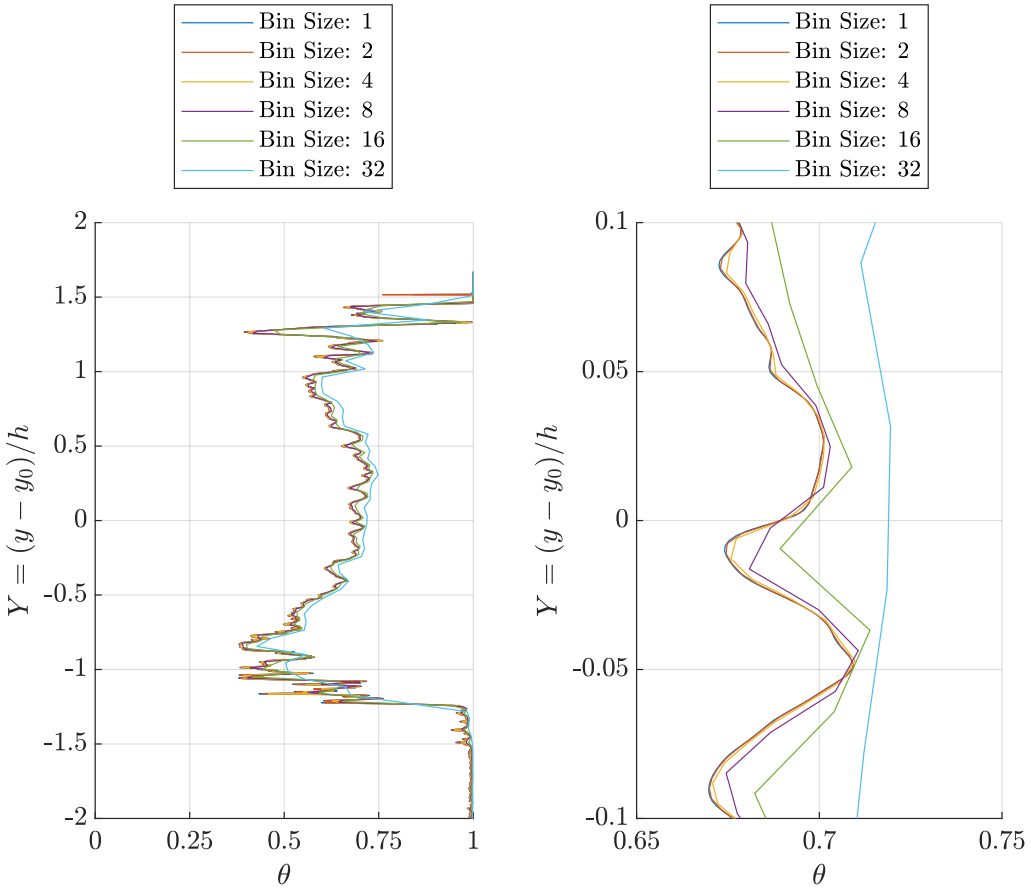


Figure 4.2: The profiles of the mixing parameter, $\theta$, for the largest Reynolds number tested, Re = 4050, at progressively larger bin size coarsening. The right image is zoomed to focus on the region near the mixing centerline.

One challenge always faced when analyzing LIF measurements is the limitation present in the camera resolution. At coarser resolutions, it can become unclear whether the signal obtained by a single pixel represents true molecular mixing, or represents small-scale entrainment or stirring that is at a scale smaller than what the camera can recognize. To address this concern, we applied a resolution study to the captured LIF data at Re = 4050. To perform this analysis, for each instantaneous volume fraction profile obtained from our LIF measurement, we subdivided the spatial

domain into bins ranging from one pixel in size (representing the original resolution of the LIF measurement), up to 32 bins. Each bin was then assigned a value equal to the mean volume fraction of pixels in that bin. Essentially, this artificially reduced the resolution of the volume fraction measurement. We then recalculated the mixing parameter, $\theta$, using the reduced resolution results.

Figure 4.2 shows the profiles of the mixing parameter for the Re = 4050 experimental set with progressively larger bin size coarsening. From a global perspective, it seems that the coarsening has negligible impact on the shape of the profile, with the core of the flow showing larger $\theta$ values than near the edges. On a local scale, however, the resolution does have an effect on the $\theta$ value. As one starts from a bin size of 32 and begins to increase the resolution, a halving of the bin size results in significant changes to the value of the mixing parameter. Nevertheless, when the bin size is smaller than around 4 pixels, halving the bin size begins to have very small impact on the mixing parameter. These results seem to suggest that further refinement of the LIF resolution would have only small impact on the ability to distinguish small-scale entrainment from molecular mixing. As a result, we can assume that the LIF results at the current resolution provide us with adequate measurements of the true molecular mixing.

## 4.2 Scalar Dissipation and Total Mixing Rate

Molecular mixing can be described by Fick's laws of diffusion. In the absence of macroscopic velocity, the diffusion flux, $J$, of a passive scalar, $C$, can be described in terms of the diffusion coefficient, $D$, and the gradient of the passive scalar, so that

$$J = -D\boldsymbol{\nabla}C. \tag{4.4}$$

In other words, as concentration gradients increase, the flux that causes concentration to spread out and mix also increases. The instantaneous scalar dissipation rate, $\chi \equiv D(\boldsymbol{\nabla} C \cdot \boldsymbol{\nabla} C)$ serves as a quantitative measure of the molecular mixing rate. For the current flow, we desire to describe the mixing rate of $f_1$ treated as a scalar mixing quantity. Because the LIF technique only provides the variation of $f_1$ along the path length of the excitation laser beam, we are limited in our capability to fully capture its gradient. However, we can still generate a qualitative estimate of the scalar dissipation rate by finding the gradient in the $y$-direction. $D$ is chosen to be the molecular diffusion coefficient of helium into air, $D = 1.386\,\mathrm{cm^2\,s^{-1}}$. This leaves us with an estimate for the scalar dissipation rate of $\chi = D(\frac{\mathrm{d}f_1}{\mathrm{d}y})^2$.

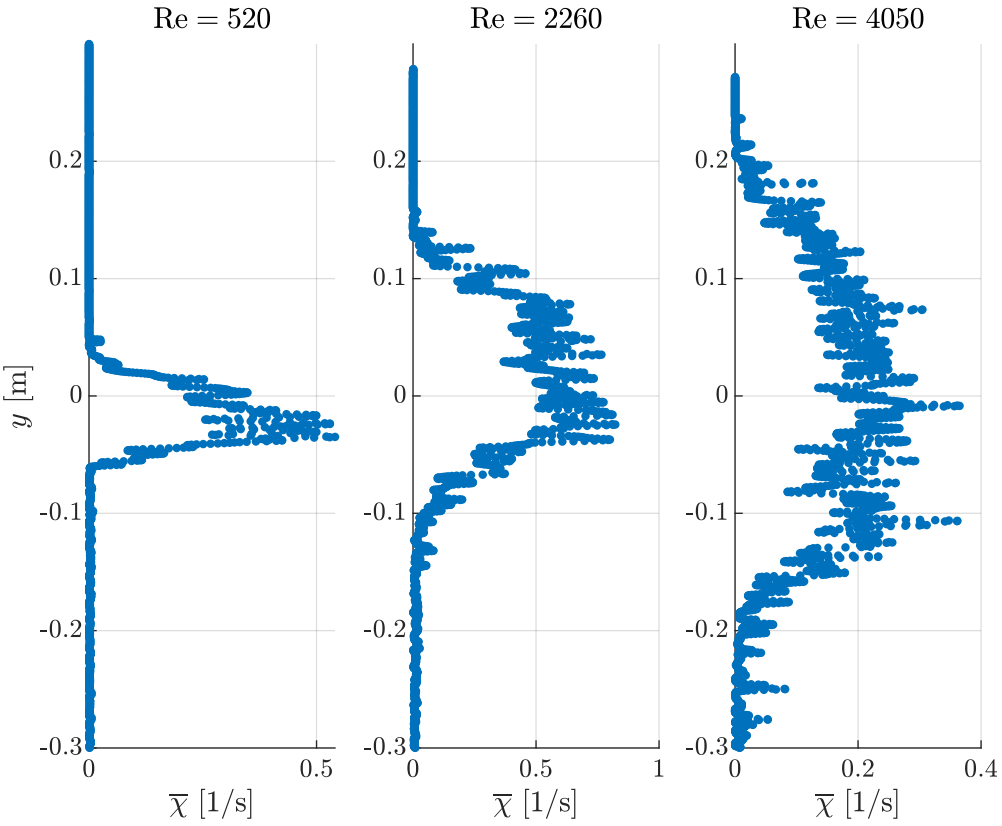


Figure 4.3: Profiles of the mean scalar dissipation, $\overline{\chi}$, for the three Reynolds numbers tested.

Figure 4.3 shows the profiles of the mean scalar dissipation rate estimate, $\overline{\chi}$, at

the three Reynolds numbers tested. As the flow moves from Re = 520 to Re = 2260, the peak of the profile increases slightly, suggesting that density gradients have sharpened. At the largest Reynolds number, molecular mixing has diffused these gradients, leaving a scalar dissipation rate peak that is significantly lower. Overall, the mixing rate in the core of the flow does not vary significantly, but transitions to zero gradually at the edges of the mixing region.

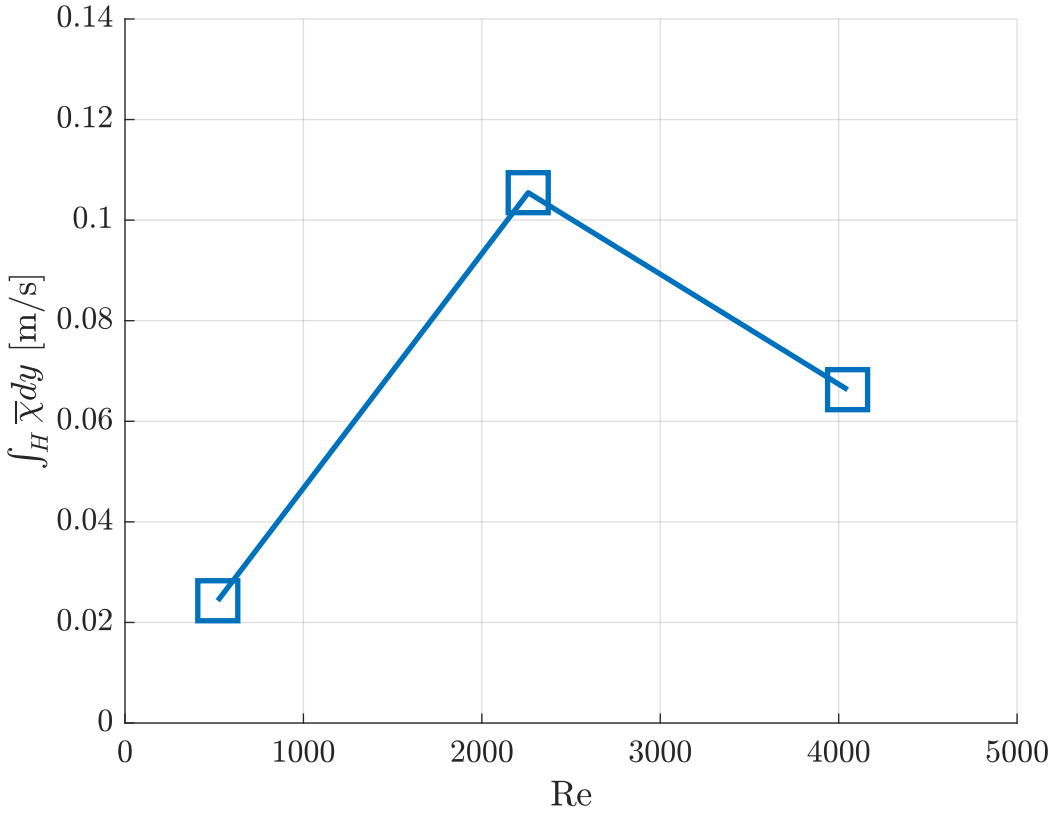


Figure 4.4: The integral of the scalar dissipation over the domain, also known as the total mixing rate of the flow, at each Reynolds number tested.

The total mixing rate of the flow, $\int \overline{\chi}$, is the spatial integration of the mean scalar dissipation rate over the entire domain. For the current flow, this corresponds to the integration of $\overline{\chi}$ in the $y$-direction at each $x$ location in the flow. This gives a measure for the total mixing rate at different Reynolds numbers in units of velocity, $\mathrm{m\,s^{-1}}$. The results are presented in Figure 4.4. The total mixing rate peaks at Re = 2260

before falling back to a value of $0.066\,\mathrm{m\,s^{-1}}$ at the largest Reynolds number. Tomkins et al. [134] showed that the normalized total mixing rate for a shock-driven instability also exhibited a strong peak at intermediate Reynolds number before reducing to a smaller asymptotic value. It is uncertain whether this trend is present in the current flow, as additional experiments in the self-similar regime would need to be conducted to find the asymptotic trend.

### 4.3 Density-Specific-Volume Correlation

Finally, an important mixing measurement that is used frequently in turbulence modeling is the density-specific-volume correlation, $b = -\overline{\rho' \left(\frac{1}{\rho}\right)'}$. $b$ can be thought of as a measure of potential for future mixing and varies from a value of 0, representing a perfect mixture, to $b_{\max} = \overline{f_1}\,\overline{f_2}\frac{(\rho_1-\rho_2)^2}{\rho_1\rho_2}$, representing completely unmixed fluids. The dependence of $b_{\max}$ on $\overline{f_1}$ and $\overline{f_2}$ suggests that it is not a constant over the width of the mixing region. Also notice that $b$ is inherently dimensionless. The definition of $b$ shown is the simplest to describe, but it can be algebraically manipulated to be described in alternative ways. One of these most useful alternatives is the recognition that $b = \overline{(\rho'\rho')/\rho\overline{\rho}}$, showing that $b$ is closely related to the mean square of the density fluctuation.

Figure 4.5 shows the profiles of $b$ at the three Reynolds numbers tested, along with bands representing the uncertainty in the statistic. At all three locations, the peak of the $b$ profile sits around $4 \times 10^{-3}$. For the Re = 520 and Re = 2260 cases, $b$ is roughly constant and symmetrical through the core of the mixing region and drops off steeply to zero at the edges of the mixing region. However, for Re = 4050, there is a clear asymmetry between bubble and spike with $b$ peaking on the spike side. This may be the result of greater noise in the density measurement in the spike side, leading to larger density and specific volume fluctuations, and therefore, to a greater covariance between them. As we will see in the following section, this explanation

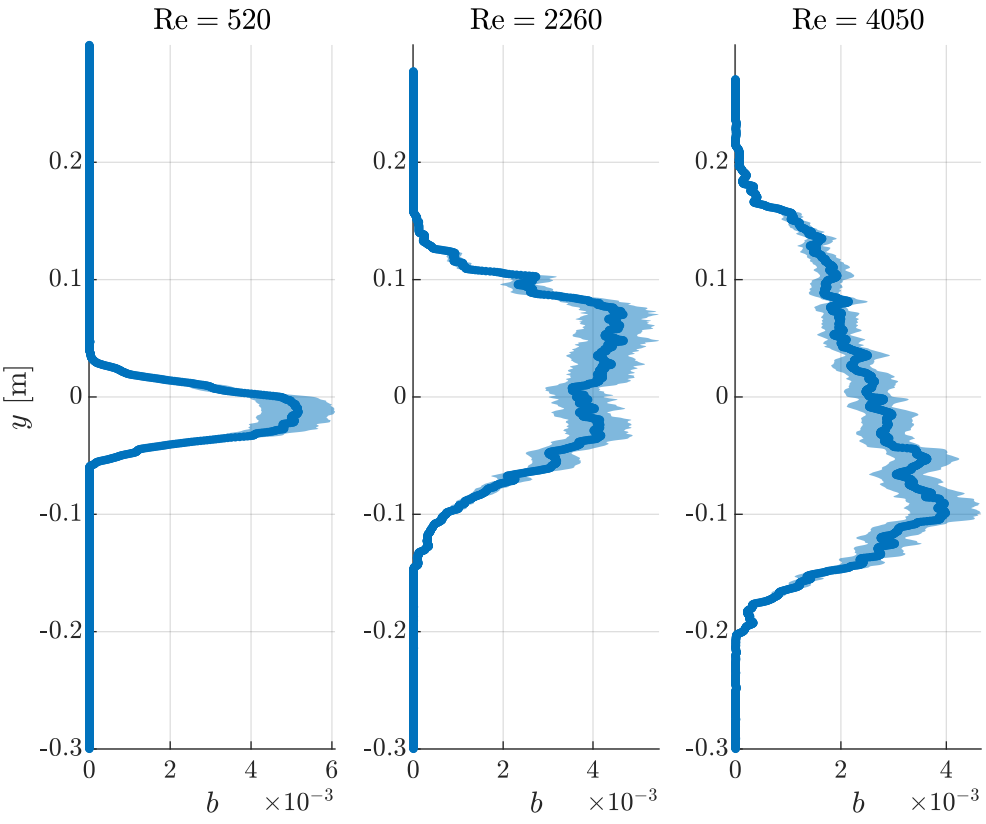


Figure 4.5: Profiles of the density-specfic-volume correlation, $b$, for the three Reynolds numbers tested, along with the associated error in the statistic.

may not capture the whole story.

Figure 4.6 shows the normalized profiles of $b$ based on normalization by $b_{\max}$. The normalization results in a $b$ profile that is nearly constant through the entire mixing region, with only moderate peaks near the edges of the mixing region. It also shows that $b/b_{\max}$ approaches a value of 0.3 at the center of the mixing region. This normalized $b$ profile changes the perspective of how the potential for mixing varies across the mixing region. Rather than viewing the potential for mixing as being maximized at the mixing centerline, it is more consistent with the results to view it as being nearly constant throughout the entire mixing region, and being mostly limited by the relative concentrations of the fluids being mixed.

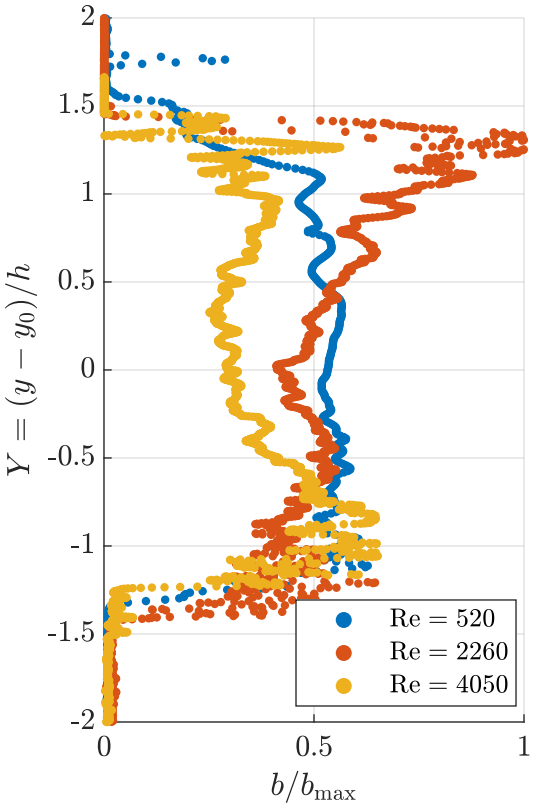


Figure 4.6: Profiles of the density-specific-volume correlation, $b$, normalized against the maximum possible value of $b$ given the volume fractions present at the spatial location, $b_{\max}$

## 4.4 Density-Specific-Volume Correlation Evolution Equation Budget

By manipulating the Reynolds-averaged continuity equation, it is possible to arrive at the transport equation for $b$, such as in the analysis technique of Besnard et al. [101]. One form of the transport equation is equation 4.5.

$$\frac{\partial b}{\partial t} + \underbrace{\tilde{u_j}\frac{\partial b}{\partial x_j}}_{\text{T1. Advection}} = \underbrace{2a_j\frac{\partial b}{\partial x_j}}_{\text{T2. Convection}} \underbrace{- 2a_j\frac{1+b}{\overline{\rho}}\frac{\partial \overline{\rho}}{\partial x_j}}_{\text{T3. Production}} \underbrace{+ \overline{\rho}\frac{\partial}{\partial x_j}\left[\frac{\overline{u_j'\rho'(1/\rho)'}}{\overline{\rho}}\right]}_{\text{T4. Transport}} \underbrace{+ 2\overline{\rho}\overline{\left(\frac{1}{\rho}\right)'\frac{\partial u_j'}{\partial x_j}}}_{\text{T5. Decay}} \tag{4.5}$$

where repeated subscripts indicated Einstein summation notation. In the current statistically stationary flow, the unsteady term, $\frac{\partial b}{\partial t}$ is zero. This leaves Term T1, the advection of $b$, as the only term on the left hand side. For this "convective-type" facility, it can be shown that the $x$ gradient of the advection term is exactly equal to the unsteady term in an equivalent "box-type" facility with homogeneous initial condition through the application of Taylor's hypothesis.

On the right hand side of equation 4.5, Term T5 is related to the decay of $b$ due to diffusion and is generally small for subsonic flows [101]. This leaves the important terms describing the convection, production, and transport of $b$, Terms T2, T3, and T4 as being the primary terms determining the budget of $b$. For the conditions of the current flow, $a_x \approx a_z \approx 0$, leading to a significant simplification for Terms T2 and T3. The evaluation of Term T4 unfortunately requires us to compute the $x$-direction gradient, which is unavailable with the current LIF diagnostic limitations, but it is reasonable to assume that gradients in the $x$ direction will be small relative to the gradients across the mixing region. These assumptions allow us to measure the budget of $b$ across the mixing region, a measurement first performed by Tomkins et al. [134].

Figure 4.7 shows the profiles of the terms in the $b$ evolution equation budget for the $\mathrm{Re} = 4050$ case. The budget shows a relatively small contribution from convection over the entire mixing width. Production is found to be asymmetric, being primarily centered in the spike. This helps to answer the question of why the $b$ profile seems to be asymmetric across the mixing region, with increased values of $b$ in the spike region; It is clear that $b$ is being produced at a greater rate in this region of the flow. Generally, production of $b$ is found to be the primary contributor to the $b$ budget, being nearly equal to the advected $b$ everywhere except at the edges of the mixing region.

The transport term changes sign as it varies from the edges of the mixing region,

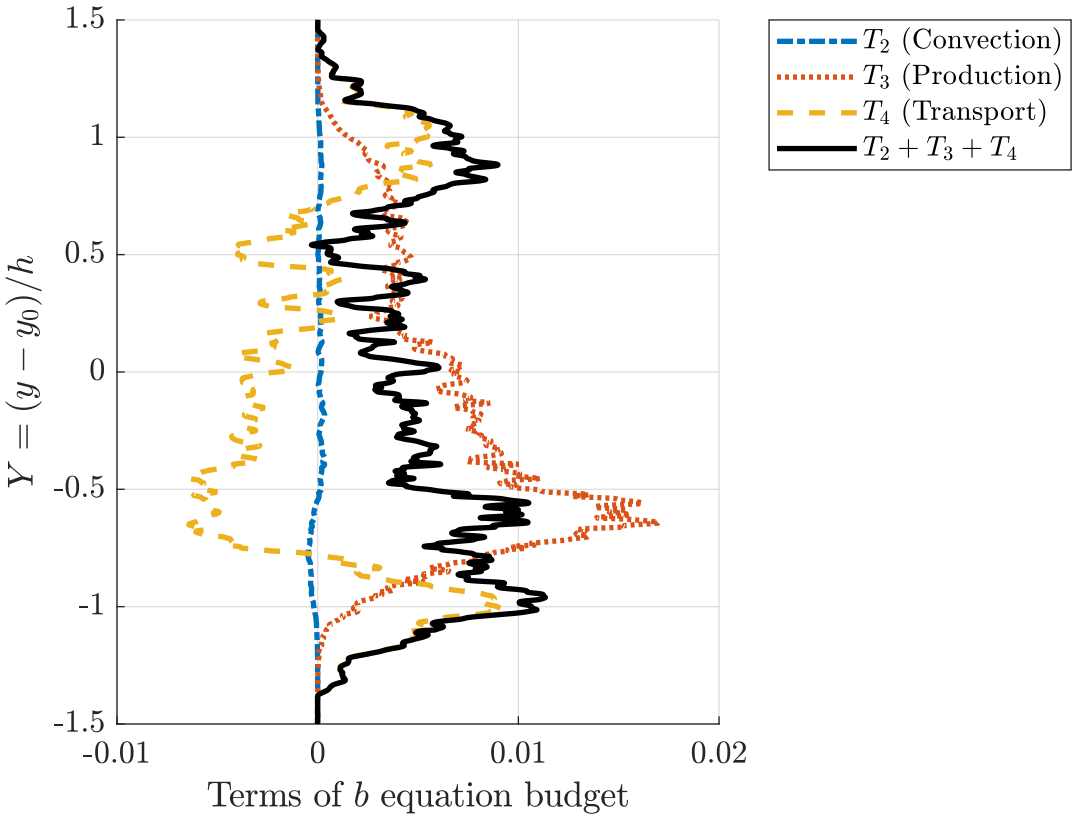


Figure 4.7: Profiles of the terms of the density-specific-volume correlation evolution equation budget, T2, T3, T4, and their sum for the Re = 4050 case.

where it is positive, to the core of the mixing region, where it is negative. It is also interesting to note that, while production rapidly vanishes to zero at the edges of the mixing region, $Y = \pm 1$, transport reaches a peak at these locations. This implies that the spatial growth of the $b$ profile is solely due to the transport of $b$ away from the core of the mixing region by the large-scale motion of the bubble and spike, and not by the production of $b$ at these locations. Together, the behavior of the production and transport profiles show the balance taking place between production of $b$ at the core of the mixing region and the transport of $b$ to the outer edges of the flow.

# CHAPTER 5
# ENERGY TRANSFER IN THE RAYLEIGH-TAYLOR INSTABILITY

## 5.1 Potential Energy Release

At its core, the RTI is an energy transfer process. Gravitational potential energy stored in the density stratification is released as the heavy and light fluid are displaced by each other. This released energy is converted into kinetic energy which, for a turbulent flow, is decomposed into the turbulent kinetic energy, $k$, and the kinetic energy of the mean flow. This conversion is not perfect, and some energy is lost as heat through viscous dissipation. Following the methodology of Youngs [135], we desire to know what fraction of the released potential energy is converted into turbulent kinetic energy based on the simultaneous measurements of the density and velocity fields.

At any downstream location, $x$, the gravitational potential energy per unit width, $PE(x)$, can be measured by integrating the density profile at that $x$ location across the entire $y$ domain of the gas tunnel, which spans from $-H/2$ to $H/2$, where $H$ is the height of the gas tunnel facility test section. This results in equation 5.1.

$$PE(x) = \int_{-H/2}^{H/2} \rho g y dy \tag{5.1}$$

Meanwhile, the kinetic energy per unit width, $KE(x)$, can be found by integrating the turbulent kinetic energy profile multiplied by the density profile across the $y$ domain,

$$KE(x) = \int_{-H/2}^{H/2} \rho k dy \tag{5.2}$$

where $k = \frac{1}{2\overline{\rho}} \left(R_x x + R_y y + R_z z\right)$, and $R_{ij} = \overline{\rho u_i'' u_j''}$. We again make the assumption

that $R_{zz} = R_{xx}$ in this flow. Because the mean flow of the gas tunnel is assumed to be fully-developed and invariant with streamwise distance, $x$, we consider the change in the kinetic energy of the mean flow to be negligible.

Although we take measurements of the density profile and kinetic energy profile at three $x$ locations, we do not take measurements at the initial condition, $x = 0$, which is necessary for a measurement of the potential energy and kinetic energy change between $x = 0$ and the measurement location $x$. Instead, we generate theoretical profiles for density and turbulent kinetic energy at $x = 0$, $\rho_0$ and $k_0$, respectively, based on our knowledge of the properties of the fluid as they flow past the splitter plate and into the test section. Because the heavy and light fluid are not allowed to mix before they enter the test section, and the density of both streams are mostly homogeneous, we assign the initial density profile as,

$$\rho_0 = \begin{cases} \rho_1 & 0 \leq y \leq H/2 \\ \rho_2 & -H/2 \leq y < 0. \end{cases} \tag{5.3}$$

For the initial kinetic energy profile, we consider the measured turbulent kinetic energy in the outer stream for the upper and lower stream, $k_1$ and $k_2$, respectively. To find these, we select the data in the range of $Y > 1.5$ and $Y < -1.5$, considered to be outside the mixing region, and find the average of the measured turbulent kinetic energy in these ranges. We choose these averages as the values of $k_1$ and $k_2$ and assign a step profile based on these values so that

$$k_0 = \begin{cases} k_1 & 0 \leq y \leq H/2 \\ k_2 & -H/2 \leq y < 0. \end{cases} \tag{5.4}$$

These profiles can then be integrated using equations 5.1 and 5.2 to obtain the initial gravitational potential energy and turbulent kinetic energy, $PE_0$ and $KE_0$. At each

measured downstream location $x$ and associated Reynolds number, the potential energy released can then be calculated as $\Delta PE(x) = PE_0 - PE(x)$, whereas the increase in turbulent kinetic energy can be calculated as $\Delta KE(x) = KE(x) - KE_0$. Because it is assumed that the potential energy released can only be converted into turbulent kinetic energy or into dissipation, $D$, the dissipated energy can be calculated as the remainder of the potential energy release which is not converted into turbulent kinetic energy $D(x) = \Delta PE(x) - \Delta KE(x)$.

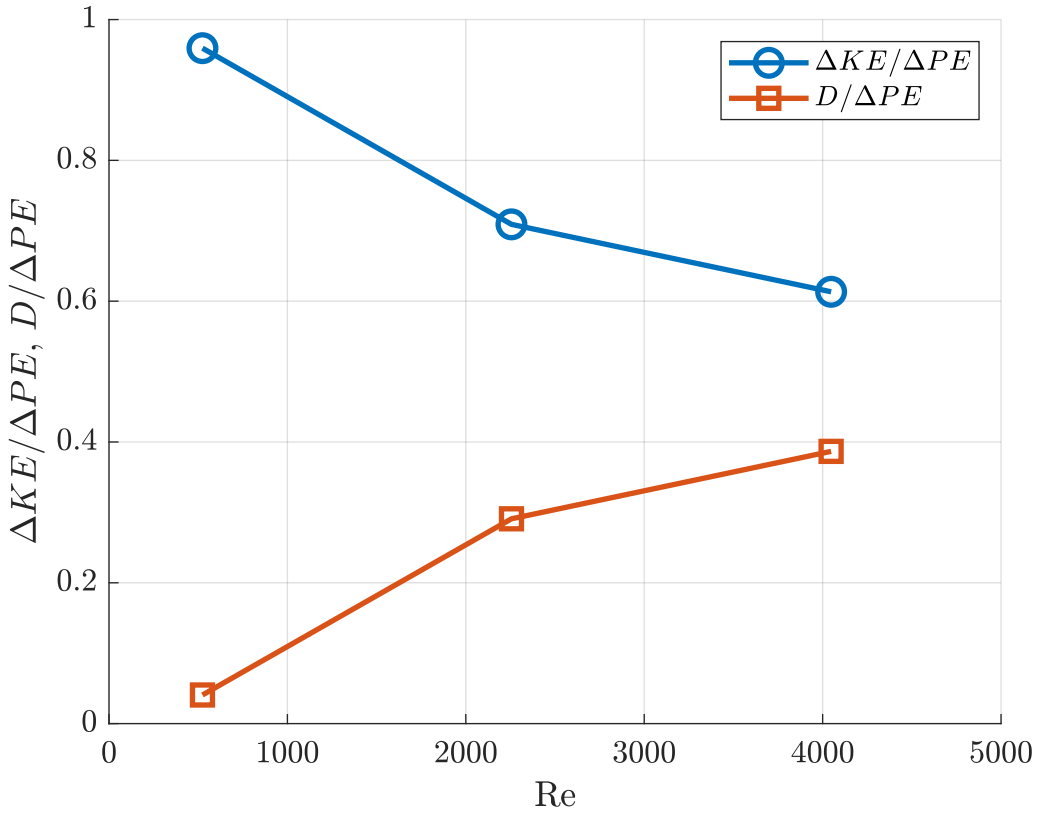


Figure 5.1: The ratio of turbulent kinetic energy generated by the RTI, $\Delta KE$, and dissipated energy, $D$, compared to the potential energy released in the flow, $\Delta PE$ for the three Reynolds numbers tested.

Figure 5.1 shows the $\Delta KE/\Delta PE$ and $D/\Delta PE$ ratios for the three Reynolds numbers tested. A more detailed examination of the values shown in the figure is presented in Table 5.1. At early instability mixing times, nearly all of the potential

Table 5.1: Details on the measured changes in potential energy, turbulent kinetic energy, and dissipated energy for the three Reynolds numbers studied.

| Re | $\Delta PE$ $\mathrm{mJ\,m^{-2}}$ | $\Delta KE$ $\mathrm{mJ\,m^{-2}}$ | $D$ $\mathrm{mJ\,m^{-2}}$ | $\Delta KE/\Delta PE$ | $D/\Delta PE$ |
|---|---|---|---|---|---|
| 520 | 0.49 | 0.47 | 0.02 | 0.96 | 0.04 |
| 2260 | 5.25 | 3.72 | 1.53 | 0.71 | 0.29 |
| 4050 | 11.57 | 7.10 | 4.47 | 0.61 | 0.39 |

energy released is converted into kinetic energy in the flow. At this early instability time there is little shear present at the interface, preventing viscosity from being able to effectively dissipate the velocity variations. However, as the Reynolds number increases and shear between the bubble and spike structures begins to grow, the strength of dissipation also increases until the dissipation accounts for 38 % of the total released potential energy. This value is low compared to the simulation results of Youngs [135] who found $D/\Delta PE \approx 0.52$, and is also low compared to the simultaneous density-velocity point measurements captured by Ramaprabhu and Andrews [71] who found $D/\Delta PE \approx 0.49$. Together with the normalized kinetic energy profile shown in Figure 3.18, these results may imply that the turbulent kinetic energy in our flow is greater than what should be expected for an RTI mixing experiment at the measured Atwood number. One potential cause for this could be the incorrect characterization of the turbulent kinetic energy of the initial condition. In general, for mesh-generated turbulence, $k$ decays with the downstream distance from the mesh as a power law with exponent approximately $n = 1.3$ [115]. Because our measurement for the $k_0$ comes from the decayed downstream location, it is possible that the true value of the $k_0$ at the interface is significantly higher. Another possibility is that the small amounts of shear present in the facility due to non-uniform convective velocity may be stronger at the initial condition than what is seen at the measurement location. As a result of turbulent processes, this shear may be being converted into velocity fluctuations and increasing the turbulent kinetic energy of the flow.

## 5.2 Turbulent Kinetic Energy Evolution Equation Budget

The ratio of turbulent kinetic energy increase to potential energy release is useful in quantifying the RTI energy transfer process. However, this quantity does little to explain the processes which lead to this energy transfer. In order to better describe these processes, we must break down their relative contribution towards the evolution of the turbulent kinetic energy.

As shown in the discussion on turbulence modeling, Section 1.4.1, most RANS-type turbulence models, such as the $k-\epsilon$ model and the BHR model, rely on the accurate modeling of the transport of turbulent kinetic energy, $k$. The compressible transport equation for $k$ can be found first by finding the transport equations for the Reynolds stress by considering the scalar product of $u_j$ and the Navier-Stokes momentum equation. By computing half the trace of this equation, one arrives at the transport equation for $k$, presented as equation 5.5

$$\frac{\partial}{\partial t}\left(\overline{\rho}k\right)+\underbrace{\frac{\partial}{\partial x_i}\left(\tilde{u}_i\overline{\rho}k\right)}_{C^k}=$$
$$\underbrace{-R_{ij}\frac{\partial\tilde{u}_i}{\partial x_j}+a_i\frac{\partial\overline{p}}{\partial x_i}}_{P^k}-\underbrace{a_i\frac{\partial\overline{\tau}_{ij}}{\partial x_j}}_{M^k}+\underbrace{\overline{p'\frac{\partial u_i''}{\partial x_i}}}_{\Phi^k}+\underbrace{\frac{\partial}{\partial x_j}\overline{u_i''\tau_{ji}'}}_{\tau^k}-\underbrace{\frac{1}{2}\frac{\partial}{\partial x_j}R_{jii}}_{D^k}-\underbrace{\frac{\partial}{\partial x_i}\overline{u_i''p'}}_{\Pi^k}-\underbrace{\overline{\tau_{ji}'\frac{\partial u_i''}{\partial x_j}}}_{\epsilon^k} \quad (5.5)$$

where $k=\frac{1}{2\overline{\rho}}R_{ii}$ and $R_{ij}=\overline{\rho u_i''u_j''}$ are the turbulent kinetic energy and Reynolds stress, both defined as they are elsewhere in this work, $R_{ijk}=\overline{\rho u_i''u_j''u_k''}$ is the velocity-triple-correlation term, $a_i=\overline{\rho'u_i'}/\overline{\rho}$ is the turbulent mass flux, and $\tau_{ij}$ is the viscous stress tensor for a Newtonian fluid. The notation used for Reynolds and Favre averaging elsewhere in this work is also applied to this equation. Equation 5.5 has been derived and presented by a variety of authors, including Cebeci and Smith [136] and Besnard et al. [101], and has been used recently for the analysis of variable-density

jet experiments using simultaneous PIV/LIF by Charonko and Prestridge [82].

The role of a turbulence model would be to simplify the grouped terms in equation 5.5 so that they could be represented as functions of the modeled quantities, such as $\rho$, $u_i$, and $k$. This requires the understanding of the relative contribution of each of the underlying equation terms towards the temporal evolution of the flow. In regards to the understanding of energy transfer in the RTI, the individual terms of equation 5.5 each represent a different physical process affecting the evolution of $k$ in the flow. Therefore, their computation and comparison will do much in providing a physical description of the energy transfer process. Thus, the quantification of these terms using the collected PIV/LIF data at $\mathrm{Re} = 4050$ is the goal of this section.

In order to compute the $k$ budget of the current experiment, several assumptions about our underlying flow must be made. First, we assume that in this statistically stationary flow all time derivatives of mean quantities are zero. Secondly, we assume that the convection of gases through the gas tunnel facility constitutes a two-dimensional flow so that derivatives of mean quantities in the $z$ direction are also zero. Thirdly, without the measurement of velocity component in the $z$-direction, $w$, we must make an assumption on the role of this velocity in the various terms in which it is necessary. In the Reynolds stress cross-correlation terms, our analysis of the anisotropy tensor revealed that cross-correlated velocity fluctuations are weakly correlated so that $R_{xy}, R_{xz}, R_{yz} \approx 0$. The term $R_{zz}$ can be estimated as equal to $R_{xx}$ as assumed elsewhere in this work, based on the results found in other RTI experiments that the magnitude of $u$ and $w$ velocity fluctuations are nearly identical. For the velocity-triple-correlation terms, the same argument can be used to determine that $R_{xzz} = R_{xxx}$ and that $R_{yzz} = R_{yxx}$. Fourthly, we apply the assumption based on our results that there is negligible correlation between density fluctuations and velocity fluctuations normal to the growth direction so that the turbulent mass flux in the $x$ and $z$ directions, $a_x = a_z = 0$. Lastly, to simplify certain gradients, we assume

that the flow is convected in a perfectly uniform way so that $\overline{u} = U_c$, the convective speed of the gas tunnel facility and $\overline{v} = \overline{w} = 0$. This simplification leads to the measurements of the Favre-averaged velocities as $\tilde{u} = U_c$, $\tilde{v} = a_y$, and $\tilde{w} = a_w = 0$.

Certain terms of the $k$ budget require the computation of gradients in the $x$ and $y$ directions. From the simultaneous PIV/LIF data that we have recorded, which provide density and velocity on the LIF excitation beam path (a one-dimensional measurement along $y$), $y$ gradients can be computed easily, but $x$ gradients are unavailable. To estimate these $x$ gradients, we assume that the flow has reached a self-similar state by the Re = 4050 location. Based on the good collapse of profiles at Re $\geq$ 2260 shown in previous sections, this is a fair assumption.

For a temporally evolving RTI flow, the similarity variable, $\eta$ can be found in terms of the location across the mixing region, $y$, and the mixing width, $h(t^2)$ as $\eta = y/h$. By substituting the temporal evolution of $h$, and recognizing the application of Taylor's hypothesis in the current flow, this allows us to find a similarity variable to describe the gas tunnel facility flow, $\eta = y/x^2$. Using this similarity variable, the various profiles computed for the flow at location $x$ can be recast in terms of their evolution with time ($t = x/U$ in the current convective flow), and a self-similar equation only dependent on $\eta$. In other words, for every measured quantity $\phi(x, y)$, we apply a self-similar transformation to recast $\phi(x, y) = x^n \hat{\phi}(\eta)$, where the exponent $n$ depends on the growth rate of the quantity $\phi$ in space. Based on the determined PIV results, and the self-similarity scalings applied by other authors [104], we can assume that Reynolds stresses and the turbulent kinetic energy follow a quadratic scaling, $n = 2$, velocity-triple-correlation terms follow a cubic scaling, $n = 3$, and turbulent mass flux follows a linear scaling. The density profile is already assumed to be self-similar, so that $n = 0$. The result of this analysis is the formation of a group of self-similar

profiles, $\hat{R}_{ij}$, $\hat{k}$, $\hat{R}_{ijk}$, $\hat{a}_i$, and $\hat{\rho}$ such that

$$R_{ij}(x,y) = x^2 \hat{R}_{ij}(\eta)$$
$$k(x,y) = x^2 \hat{k}(\eta)$$
$$R_{ijk}(x,y) = x^3 \hat{R}_{ijk}(\eta)$$
$$a_i(x,y) = x \hat{a}_i(\eta)$$
$$\overline{\rho}(x,y) = \hat{\rho}(\eta).$$

The self-similar profiles are found from the measurements of the profiles at the $x = 1.75\,\mathrm{m}$, $\mathrm{Re} = 4050$ location and can be linearly interpolated to find their value at any value of $\eta$.

With the self-similar profiles in hand, gradients of a quantity $\phi$ in the $x$ direction can be found by computing $\phi(x + \Delta x, y)$ and $\phi(x - \Delta x, y)$ and applying a first-order central-difference scheme to define

$$\frac{\partial \phi}{\partial x} = \frac{\phi(x + \Delta x, y) - \phi(x - \Delta x, y)}{2\Delta x} \tag{5.6}$$

with the value of $\phi$ at each downstream location being found using the self-similar profiles. To increase the accuracy of the gradient, small values of $\Delta x$ should be used. Specifically, we chose for $\Delta x$ to equal the $y$ resolution of the LIF measurement so that $\Delta x = \Delta y$. Gradients in the $y$ direction were also found using a central-difference scheme. Finally, in order to reduce the noise in the gradients, a Gaussian filter of 5 cm window size is used to reduce the strength of high-frequency fluctuations in the profiles of the measured quantities before the central-difference derivatives are computed. The measurements of the grouped terms in equation 5.5 are iterated below.

The first term on the left hand side is the unsteady term, which is zero for the

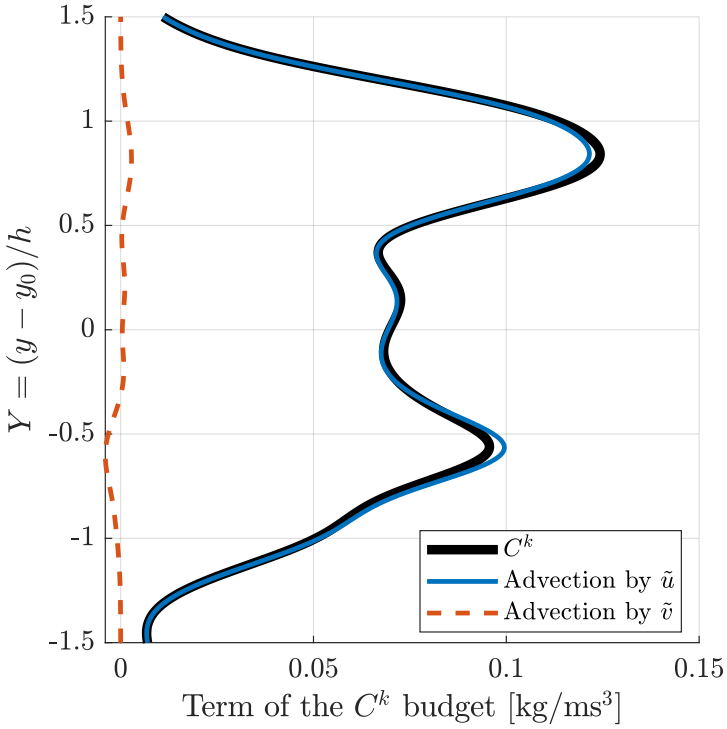


Figure 5.2: Profile of the advection term, $C^k$, and the relative contributions of the horizontal and vertical gradient terms.

statistically stationary flow of the gas tunnel facility. The second term on the left hand side, $C^k$ represents the advection of turbulent kinetic energy, and for the current flow, it simplifies to

$$C^k = \frac{\partial}{\partial x}(\tilde{u}\overline{\rho}k) + \frac{\partial}{\partial y}(\tilde{v}\overline{\rho}k). \tag{5.7}$$

It can be shown that the first term of $C^k = \frac{\partial}{\partial x}(\tilde{u}\overline{\rho}k) = \frac{\partial t}{\partial x}\frac{\partial}{\partial t}(\tilde{u}\overline{\rho}k) = \frac{1}{U_c}\frac{\partial}{\partial t}(U_c\overline{\rho}k) = \frac{\partial}{\partial t}(\overline{\rho}k)$ is identically equal to the unsteady term for the typical "box-type" RTI experiment when Taylor's hypothesis is applied. Figure 5.2 shows the profile for $C^k$, as well as the contributions of the horizontal and vertical gradient. As expected, the horizontal gradient, which represents the total growth rate of $k$, is dominant with the vertical gradient only providing a small effect. The advection peaks at the inner edge of the mixing width, around $Y \approx \pm 0.7$, indicating that the major growth in turbulent kinetic energy in the flow occurs at the edges of the mixing region, and not in the

center. The advection also extends far beyond the mixing width, indicating that the RTI serves to increase the turbulent kinetic energy of the flow even in the free-stream through large-scale motions of the bubbles and spikes. It should be noted that, unlike in the displayed Figure, the advection of $k$ should go to zero or be negative in the free-stream. This is not the case in the current analysis because of the method by which $x$ gradients have been captured, using a self-similarity assumption instead of taking true measurements. The self-similarity assumption does not apply to the flow outside of the mixing region, and so it fails to accurately capture the advection of $k$ in this region. This will have implications on the calculation of the dissipation budget, $\epsilon^k$.

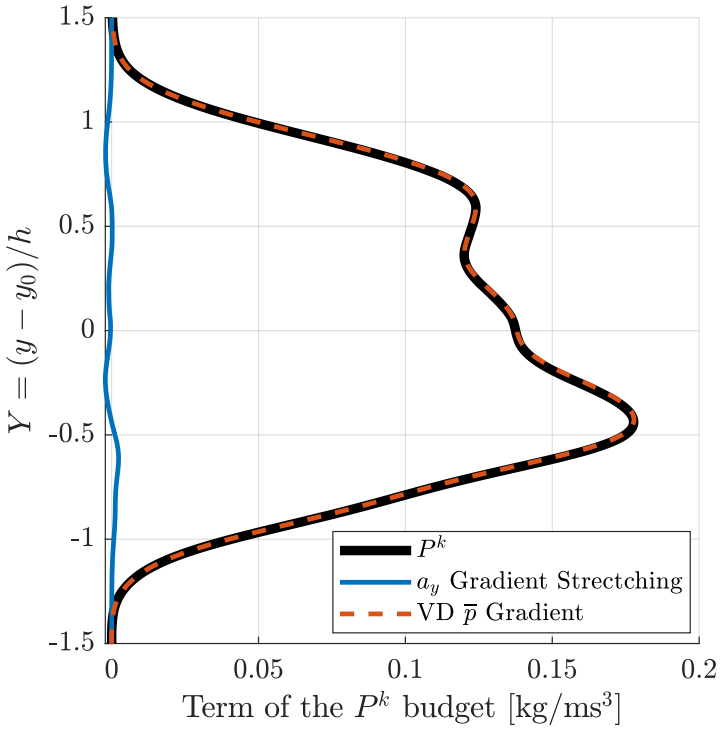


Figure 5.3: Profile of the production term, $P^k$, and the relative contributions of the velocity gradient stretching term and the variable density pressure gradient term.

The first group of terms on the right hand side of equation 5.5 is $P^k$ which represents the production of turbulent kinetic energy. With the assumptions made, the

production term simplifies to

$$P^k = -R_{yy}\frac{\partial a_y}{\partial y} + a_y\frac{\partial \overline{p}}{\partial y}. \tag{5.8}$$

The first term on the right hand side represents the production of turbulence due to the stretching of velocity gradients by the velocity fluctuations. The second term represents the production of turbulence due to the interaction between the pressure gradient and the turbulent mass flux fluctuations. To estimate pressure gradient, we remember that the major contribution to variation of pressure in the RTI framework is the hydrostatic pressure increase due to gravitational acceleration. This provides a measure for $\frac{\partial \overline{p}}{\partial y} = -\overline{\rho}g$. Figure 5.3 shows the profile of the production term, as well as the relative contribution of the velocity gradient and variable-density pressure gradient terms. Because velocity gradients are relatively weak, we find that the production due to velocity gradients is small in this flow. This is one way in which RTI contrasts with a shear-driven instability flow, in which this term is the dominant production term. Meanwhile, due to the large values of $a_y$ and the strong hydrostatic pressure gradient, the variable-density pressure gradient term is the dominant production term. While there is a peak in the production at $Y \approx -0.5$, the production is relatively uniform across the entirety of the mixing core, and proceeds past the mixing width, $h$.

The second group of terms on the right hand side of equation 5.5 is $M^k$, which represents the molecular shearing effect which, for the current flow in which no mean shear is present, is identically zero. The third group of terms, $\Phi^k$, which represents the pressure strain effect, can be thought of as the flow work applied by the turbulent fluctuations. In subsonic flows such as our own, the divergence of the Favre averaged velocity fluctuations is nearly zero and $\Phi^k$ is negligible.

The next three terms in equation 5.5 which are all represented as a gradient

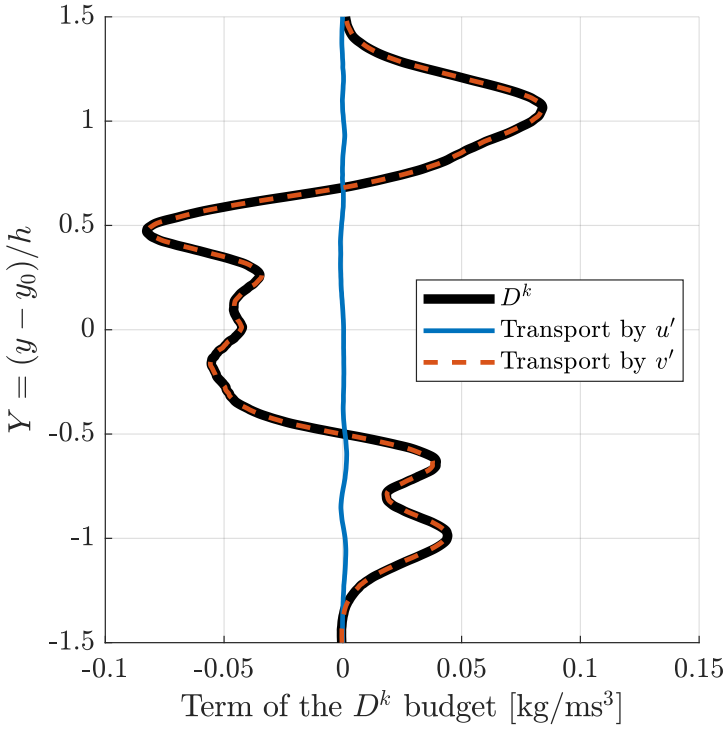


Figure 5.4: Profile of the turbulent transport term, $D^k$, and the relative contributions of the horizontal and vertical velocity fluctuations.

of a mean quantity are the transport terms. Because the integral of these terms across the flow volume is identically zero, these terms represent the movement and redistribution of turbulent kinetic energy around the flow domain, rather than its production or destruction. The first of these terms, $\tau^k$, represents the transport of $k$ by viscous forces, and is generally considered to be small in large Reynolds number flows. The same assumption has been for large Reynolds number flows by other works [82, 137, 138]. Instead, the major contributor towards transport of $k$ is the following term, $D^k$, which represents the transport of turbulent kinetic energy by velocity fluctuations. It is this term which involves the velocity-triple-correlation term, and for the current flow it can be simplified to

$$D^k = -\frac{1}{2}\left[\frac{\partial}{\partial x}\left(R_{xxx} + R_{xyy} + R_{xzz}\right) + \frac{\partial}{\partial y}\left(R_{yxx} + R_{yyy} + R_{yzz}\right)\right]. \tag{5.9}$$

The equation for $D^k$ shows that it can be decomposed into the contribution of the horizontal and vertical velocity fluctuations towards the transport of $k$. For an RTI flow which is dominated by vertical velocity fluctuations, we suspect that the vertical velocity fluctuations will be most responsible for turbulent transport. This is confirmed when inspecting Figure 5.4, which shows the profile of the turbulent transport term, as well as the relative contributions of the horizontal and vertical velocity fluctuations. Overall, horizontal velocity fluctuations have nearly no effect on the transport of turbulent kinetic energy. When considering the total transport, we find a structure similar to the transport term for $b$, in which $k$ is moved away from the core of the mixing region and deposited at the edges, near $Y = \pm 1$. The result is that, even though the production of turbulent kinetic energy is dominated at the core of the mixing region, $k$ in this region is quickly transported in a way that leads to dominant advection at the edges of the mixing region, not at the center. It is this transfer process that results in the growth of the RTI mixing width and the transfer of turbulence into the free-stream.

The final transport term, $\Pi^k$, represents the transport of $k$ due to pressure fluctuations and requires the measurement of pressure fluctuations throughout the flow. In general, most experiments are not able to solve for this term. Lumley [139] proposes a model for the pressure transport in terms of the turbulent transport, $\Pi^k = -2/5 D^k$, which is the model used for this analysis and by Charonko and Prestridge [82]. This model is qualitatively accurate except at near-wall conditions where the presence of the wall suppresses pressure fluctuations dramatically faster than velocity fluctuations, leading to an imbalance between the two.

The final term in equation 5.5 is $\epsilon^k$, the dissipation of turbulent kinetic energy. In general, the computation of this term requires the measurement of velocity gradients down to the smallest dissipative scales in the flow, the Kolmogorov microscale, $\eta$. This would not be possible considering the diagnostic limitations of our PIV setup.

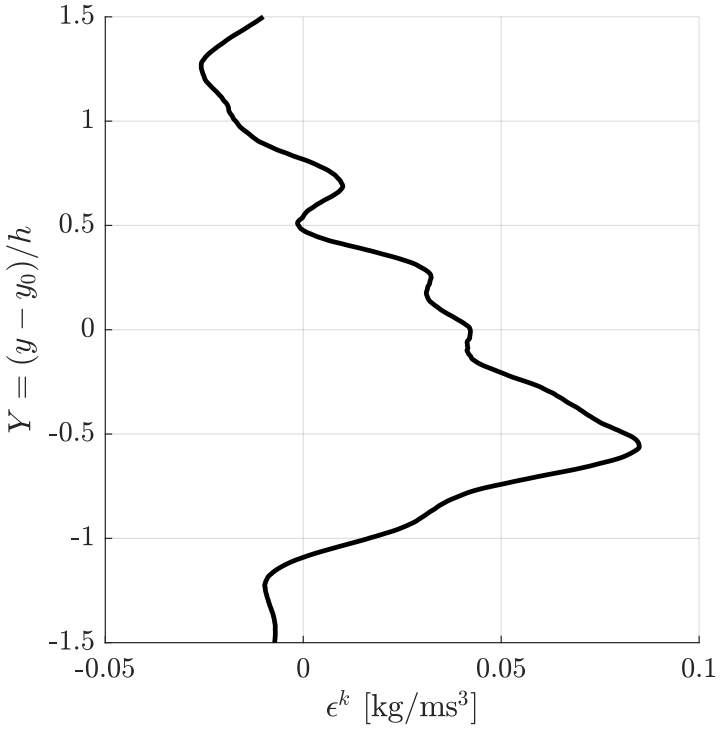


Figure 5.5: Profile of the dissipation, $\epsilon^k$.

However, we are able to provide an estimate for the dissipation by filling in the remaining terms in the $k$ evolution equation and solving for dissipation, leading to the equation that

$$-\epsilon^k \approx C^k - P^k - D^k - \Pi^k. \tag{5.10}$$

Figure 5.5 shows the profile for the dissipation across the mixing region. Most importantly, we find that there are places in the flow where the dissipation is not positive, implying that viscous action is leading to an increase in kinetic energy. This is unphysical, and simply related to the limitations in the current technique for measuring $x$ derivatives. Because the advection term is found using a self-similarity argument, which is invalid at the far edges of the flow, it does not take on the negative value it should take in these regions where only dissipation is present. The result is that the dissipation does not take on a positive value, indicating the loss of advected $k$, and instead has negative value acting as the mechanism that keeps the advected $k$

positive. Despite this limitation, the profile for $\epsilon^k$ still provides insights into the mechanism of viscous action in the flow. The dissipation is greater at the core of the mixing region when compared to the edges, suggesting that it is dominant in the regions where shear between the bubble and spike structures is occurring.

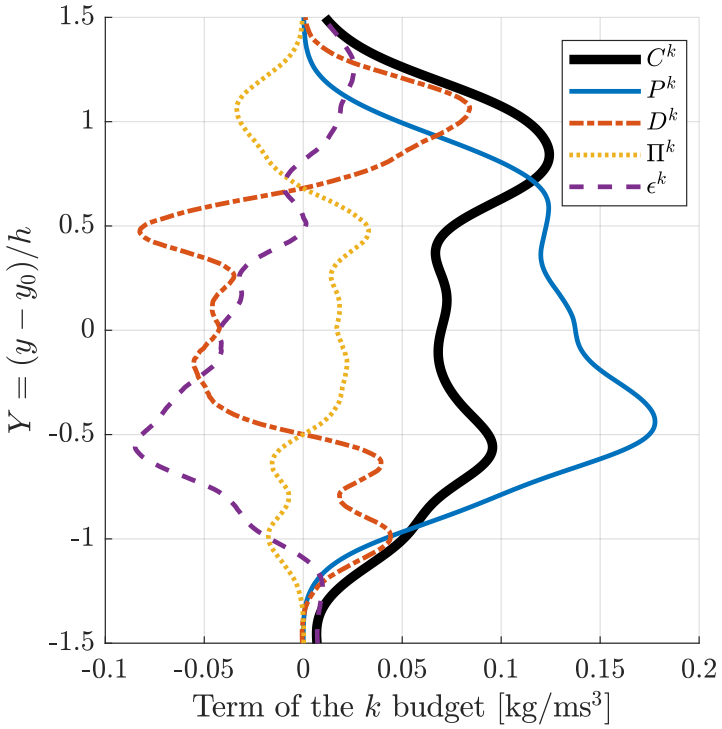


Figure 5.6: Profiles of the terms of the $k$ budget, evaluated for the Re = 4050 case.

Finally, Figure 5.6 shows the overlayed profiles of the terms for the turbulent kinetic energy evolution equation. The first trend to be observed is that in the advection of the flow, $C^k$, is primarily maintained by the production of turbulent kinetic energy, $P^k$ nearly everywhere in the flow. This indicates that, although there are many mechanisms which affect $k$, the primary driver is the production of $k$, specifically through the release of potential energy.

The interaction between production and the transport of turbulent kinetic energy, $D^k$ is also important to note here. In general, transport serves to move $k$ away from the core of the mixing region where the production is dominant to the edges where it

is weaker. As seen when analyzing the budget of $D^k$, the primary mechanism for this transport is vertical velocity fluctuations associated with the large-scale motion of the bubble and spike. At the very edges of the mixing region, especially on the bubble side, this is the dominant process. This implies that the growth of the turbulent mixing region in RTI flows is the primarily the result of the transport of $k$.

As shown in Figure 5.6, the production and dissipation of turbulent kinetic energy is not balanced in RTI flows. It is this imbalance, with production exceeding dissipation, that leads to the overall growth of the instability, resulting in a positive advection term. Despite this imbalance, the shape of the dissipation and production profiles have similarities, with both peaking around $Y = -0.5$. The implication is that, in regions of the flow where the production is greater than can be transported away, a stronger dissipation process serves to normalize the level of $k$ growth.

### 5.3 Taylor Microscale

The Taylor microscale, $\lambda$, represents the scale at which viscosity begins to have an impact on the dynamics of the energy cascade. One method for the computation of $\lambda$, outlined by Pope [115], is by computing the fluctuations and gradients of the velocity fields through equation 5.11.

$$\lambda_{ij} = \sqrt{\frac{2\overline{u_i' u_i'}}{\overline{(\frac{\partial u_i'}{\partial x_j})^2}}} \tag{5.11}$$

For isotropic turbulence, $\lambda_{u,x}$ is termed the longitudinal Taylor microscale and $\lambda_{u,y}$ is the transverse Taylor microscale. However, for an anisotropic flow, the Taylor microscales measured in terms of the vertical velocity fluctuation may also be measured for comparison. In many regards, because the RTI flow is dominated by vertical velocity fluctuations which vary dramatically over the $y$ direction, perhaps $\lambda_{v,y}$ is the length scale most pertinent to the understanding of the flow. Furthermore, there is no reason to assume that the Taylor microscale should be uniform in space for turbulence

which is localized.

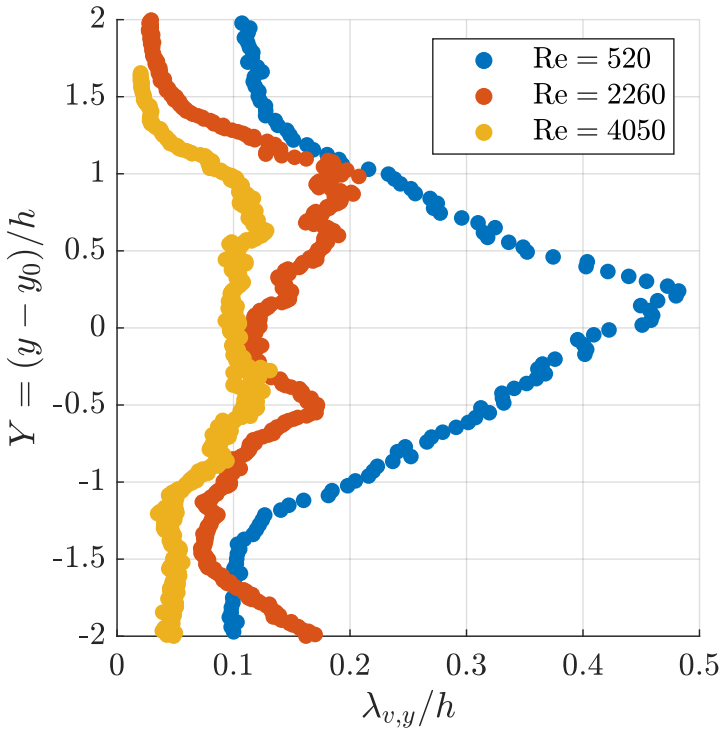


Figure 5.7: Profiles of the Taylor microscale $\lambda_{v,y}$ measured based on $y$ gradients of the vertical velocity fluctuation, $v'$, for the three Reynolds numbers tested. Results are normalized based on the half-width of the mixing region.

Figure 5.7 shows the profiles for $\lambda_{v,y}$ for the three Reynolds numbers tested, normalized by the mixing width for that Reynolds number. Because the mixing width is an estimator for the integral scales of the turbulence, this figure can be used to show the separation of scales that develops as the Reynolds number of the flow increases. At the largest Reynolds number tested, the pertinent Taylor microscale of the flow is separated from the largest scales by about a decade. Figure 5.8 compares the measures of the Taylor microscales for both velocity components and in both gradient directions. There is little variation in $\lambda$ across the entire extent of the mixing region, and it only drops down to the small values of the free-stream near the edges of the mixing region. The figure shows that there is little difference in the length scale behavior for the horizontal velocity component, $u$. However, $\lambda_{v,y}$ is much larger than all

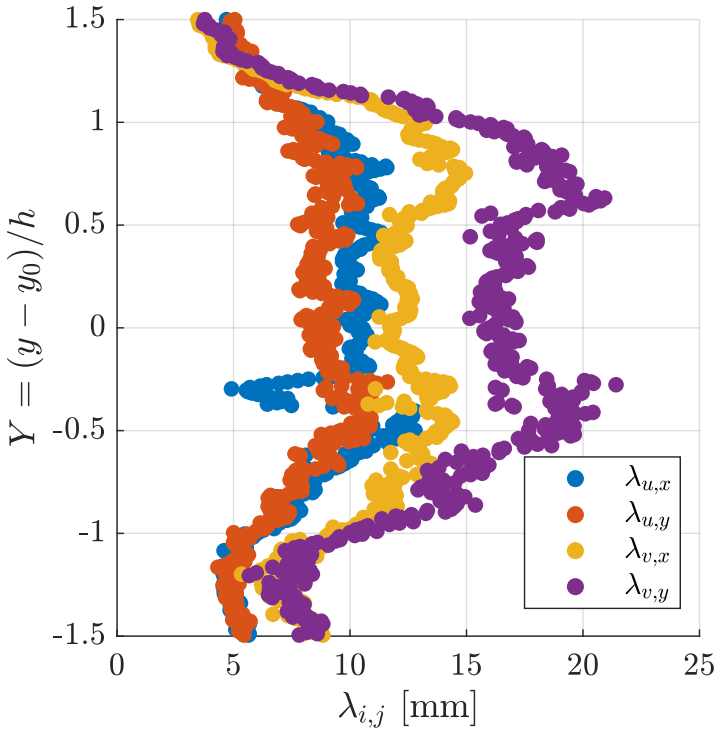


Figure 5.8: Profiles of the Taylor microscales measured based on $x$ and $y$ gradients of the horizontal and vertical velocity fluctuations, $u'$ and $v'$ for the Re = 4050 experimental case.

of the other length scales measured. This implies that vertical gradients in the vertical velocity fluctuations are dissipated by viscosity at larger scales than other gradients in the flow. This may be the result of the strong shear that manifests itself at the interface between the rising bubble and spike. This helps to understand the nature of the anisotropy for RTI flows. Finally, Figure 5.9 shows the profiles of $\lambda_{v,x}$, the "RTI transverse" Taylor microscale for the flow, normalized by the mixing width and $\mathrm{Re}^{-1/2}$, the typical scaling used for the Taylor microscale. The figure shows that the Taylor microscale collapses to a value of 5 in the core of the mixing region. Compare this to the typical value given of $\sqrt{10} \approx 3.1$. This indicates that the Taylor length scale in RTI flows displays the same $\mathrm{Re}^{-1/2}$ scaling typically assumed for isotropic turbulence.

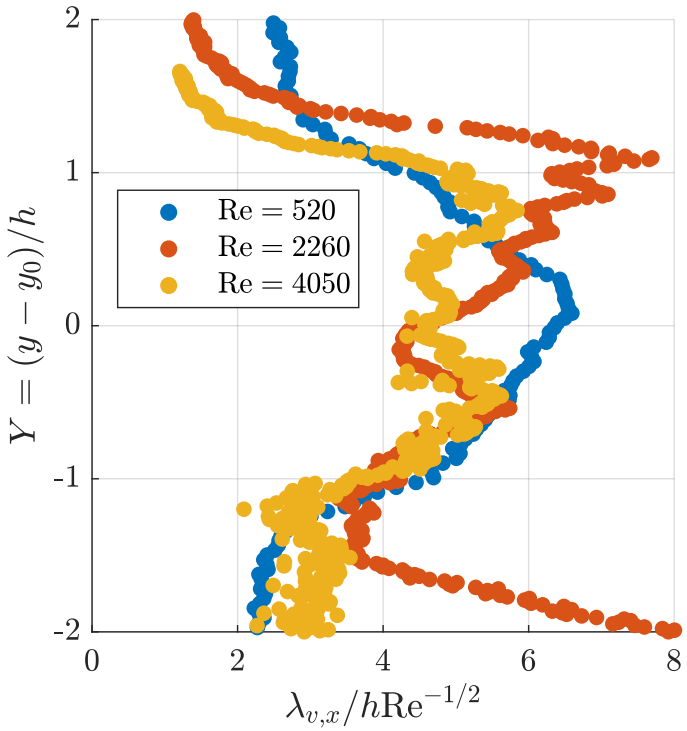


Figure 5.9: Profiles of the Taylor microscale $\lambda_{v,x}$ measured based on $x$ gradients of the vertical velocity fluctuation, $v'$, for the three Reynolds numbers tested. Results are normalized based on the half-width of the mixing region and the inverse square root of the Reynolds number, $\mathrm{Re}^{-1/2}$.

## 5.4 Estimates of Dissipation

Through the analysis of the turbulent kinetic energy budget, we were able to arrive at an estimate for the dissipation of turbulent kinetic energy $\epsilon$ across the flow. However, this is not the only method for computing the dissipation.

Taylor [66] is a classic work which typically marks the beginning of the study of isotropic turbulence. In this paper, Taylor defined the transverse Taylor microscale in terms of the transverse velocity auto-correlation function, $\lambda_g$. He then showed that, for isotropic turbulence, the dissipation of turbulent kinetic energy could be related to the velocity fluctuations in the flow and the Taylor microscale by

$$\tilde{\epsilon} = 15\nu u'^2/\lambda_g^2 \tag{5.12}$$

As described in our analysis of the Taylor microscales evaluated using PIV data, the "longitudinal" flow direction for the RTI flow is the primary direction of interest, $y$, whereas the "transverse" flow direction is the longitudinal normal, $x$. Thus, the best estimate for the transverse Taylor microscale in the current flow is $\lambda_{v,x}$, based on the gradients of the vertical velocity fluctuations in the $x$ direction. Using this Taylor microscale estimate, and choosing $u' = v'_{\mathrm{RMS}}$ to be the turbulent velocity scale for our flow, we can arrive at an equation for the dissipation in the RTI flow in terms of quantities previously presented in this work as

$$\epsilon = 15\overline{\rho}\nu {v'_{\mathrm{RMS}}}^2/\lambda_{v,x}^2 \tag{5.13}$$

Where the addition of the mean density has been applied to transform the dimensions of $\tilde{\epsilon}$ from being per unit mass to being per unit volume.

Figure 5.10 shows the comparison between the two methods for estimating the turbulent kinetic energy dissipation for the flow. The peak values for both profiles are similar, around a value of $0.06\,\mathrm{kg\,m^{-1}\,s^{-3}}$ to $0.08\,\mathrm{kg\,m^{-1}\,s^{-3}}$. However, there is clear deviation between the two dissipation estimates in the upper half of the flow, at $Y \geq 0$, with the estimate found using the Taylor microscale being larger. The reason for this may be the calculation method for the dissipation from the turbulent kinetic energy budget. In that method, the dissipation was defined as the residual energy after considering the effect of advection, production and transport on the budget. Specifically, the production in this region of the flow was smaller compared to the advection, leading to a relatively small value of the dissipation. However, the good agreement of the dissipation estimates shows that both methods of computation may be used to understand the characteristics of the turbulent kinetic energy dissipation.

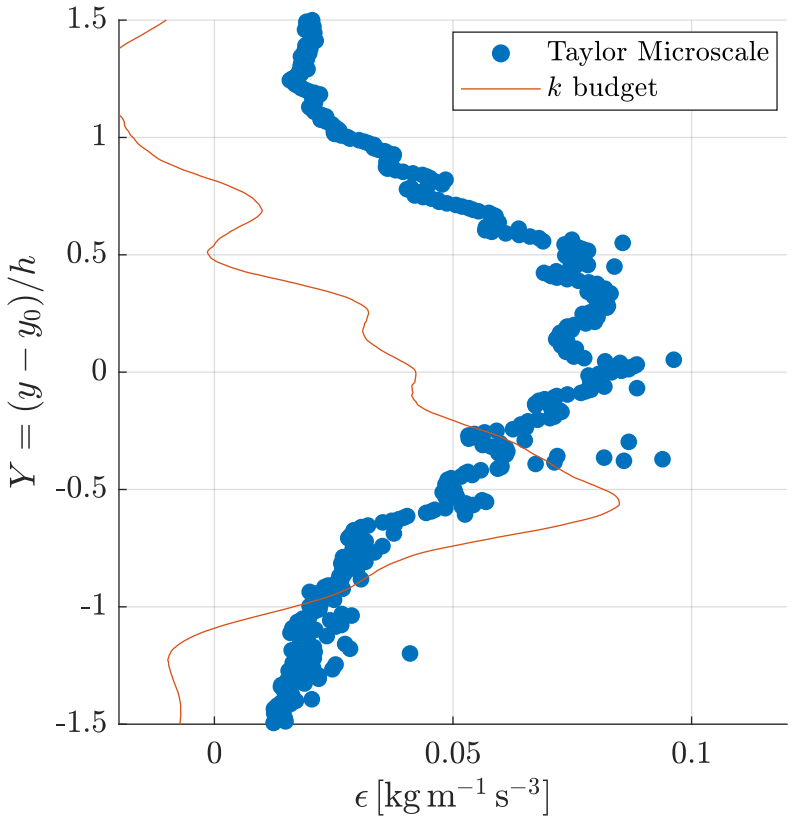


Figure 5.10: Profiles of the dissipation of turbulent kinetic energy found using the Taylor microscale and the $k$ budget.

# CHAPTER 6
# CONCLUSIONS

For the first time, simultaneous density-velocity field measurements were captured for the Rayleigh-Taylor instability using a combined PIV/LIF diagnostic. Measurements were captured at Atwood number $\mathcal{A} \approx 0.1$ at three Reynolds numbers, Re = 520, 2260, and 4050. Results are compared to the experiments performed at $\mathcal{A} = 0.73$ by Akula and Ranjan [76] and at $\mathcal{A} = 7.5 \times 10^{-4}$ by Ramaprabhu and Andrews [71]. The RANS simulations of Schwarzkopf et al. [109] and DNS of Cabot and Cook [110] are also used as comparisions.

The statistically stationary nature of the gas tunnel facility allows for the computation of statistical quantities with small experimental uncertainty. From the LIF diagnostic, measurements of the volume fraction profile show the quadratic growth rate of the instability in the self-similar regime at Reynolds number greater than 2260. The growth rate parameter is found to be $\alpha = 0.049$. When normalized by both the cutoff mixing width and the integral mixing width, the volume fraction profile shows good collapse across all Reynolds numbers, with the shape being most similar to a linear variation in the mixing region. Probability density functions of the volume fraction show that the statistical characteristics do not change dramatically at the edges of the mixing region. However, as Reynolds number increases, the amount of mixed material found at the core of the mixing layer increases. Even at large Reynolds number, there remains significant quantities of unmixed fluid, indicating a strong degree of bubble/spike interpenetration and entrainment.

Velocity measurements are captured using the PIV diagnostic. The root mean square velocity fluctuation profiles show flat peaks through the core of the mixing region, indicating the homogeneous nature of the turbulence in the core. The vertical

velocity fluctuations grow linearly in time, confirming the linear growth of the RTI growth rate and subsequent quadratic growth of the mixing width. The growth rate parameter based on the velocity fluctuations is found to be $\alpha = 0.071$. When normalized by the Goncharov bubble velocity, the velocity profiles show good self-similar collapse and agreement with the low Atwood number/high Schmidt number data of Ramaprabhu and Andrews [71]. The self-similar profiles deviate significantly from the high Atwood number experiments collected by Akula and Ranjan [76], most likely because of the increased turbulence generated by asymmetric spike structures at larger Atwood number. While Schmidt number does not seem to have significant impact on the shape of the RTI fluctuations, the asymmetry between bubble and spike that develops at large Atwood number does. There is also significant anisotropy in the flow, with horizontal velocity fluctuations being only 60 % of the vertical velocity fluctuations. This degree of anisotropy is uniform across the mixing region.

The simultaneous PIV/LIF diagnostic allows the computation of correlated quantities of density and velocity. The profile of the turbulent mass flux shows asymmetry in the development of the instability, with increased turbulent mass flux in the spike. The result is a larger production of turbulence in the spike region. The Reynolds stress profiles show good collapse when normalized by the self-similar velocity scale. When the Reynolds stress profiles are decomposed, it is revealed that the triple correlation term and turbulent mass flux term have negligible impact on the Reynolds stress, contributing together only 1 % of the total value. The turbulent kinetic energy profile is also shown. The simultaneous density-velocity measurements allow us to apply conditional sampling techniques to isolate the relative impact of the bubble and the spike on the statistics. While there is generally similarity between bubble and spike statistics, the turbulence of the spike is found to be slightly greater, indicating the possibility of asymmetry at the currently tested Atwood number.

Molecular mixing in the RTI flow is studied by calculating the molecular mixing

parameter, the scalar dissipation, the total mixing rate, and the density-specific-volume correlation term, $b$. The molecular mixing parameter shows greater molecular mixing at the center of the mixing region compared to the edges. The molecular mixing parameter at the core of the flow increases with Reynolds number towards an asymptotic value of 0.75. The scalar dissipation shows a maximum in the peak value at Reynolds number 2260, suggesting a sharpening of gradients as the flow transitions from the non-linear regime into the bubble re-acceleration regime and finally into the self-similar regime. This peak in scalar dissipation is in agreement with other studies of molecular mixing. The profiles of the density-specific-volume correlation show that it takes on a nearly constant peak value regardless of Reynolds number. At the largest Reynolds number, there is asymmetry towards the spike side, with sharp fall-off towards the mixing edges. An analysis of the transport equation of the density-specific-volume correlation shows that production is the dominant mechanism in the core of the mixing region, while transport is primarily responsible for the movement of $b$ to the edges of the flow and the spatial-growth of the density-specific-volume correlation layer.

An analysis of the turbulent kinetic energy produced and gravitational potential energy released shows that the ratio of dissipated energy to potential energy released is 38 % at the largest Reynolds number, smaller than that typically presented for both experiments and simulations. The budget of the turbulent kinetic energy, $k$, is studied term by term. Advection is found to be maximum at the edges of the mixing region, and not at the core, suggesting that the outward growth of the instability is stronger than the maintenance of turbulence in the core. Production is found to be dominated by the variable-density pressure gradient term and not by velocity gradient stretching. Transport is found to be dominated by the movement of $k$ through large-scale vertical motions of the bubble and spike. It is through the transport that the strong advection at the edges of the mixing region is maintained. Dissipation is found

to increase proportionally to the rate of production, serving as a balancing mechanism. Measurements of the Taylor microscale show the strong anisotropy present in the flow. $\lambda_{v,y}$ has the largest value, suggesting vertical velocity fluctuations in the vertical direction are most strongly acted on by viscosity. The values of $\lambda$ are in line with our predictions. $\lambda$ can also be used to estimate the dissipation of turbulent kinetic energy, and we find good agreement between this calculation of dissipation and the dissipation found in the $k$ budget.

Despite the experimental advances made in this work, there are still many questions about the development of the RTI in the fully turbulent regime that remain unanswered. One is the nature of the self-similarity in this flow. While self-similar collapse was obtained, it is uncertain if this self-similarity will persist as the spectral content of the initial conditions are changed. Likewise, while the mixing transition was seen qualitatively in the flow, we were unable to capture the development of an inertial subrange and separation of scales, or to evaluate other quantitative criteria for the mixing transition. The major suggestion for future work is to perform high-speed LIF or PIV diagnostics both at the initial condition and in the self-similar regime in order to understand the spectral content of the turbulence and make more concrete claims on the topics of self-similarity and mixing transition. Furthermore, the ability to modulate the initial condition, perhaps through the use of active turbulence generation devices, could help to shed light on the universality of the self-similar profiles and their memory of the initial conditions. Also useful towards the understanding of mixing transition is the measurement of streamwise vorticity, requiring the measurement of velocity in the $y$-$z$ plane. The development of these types of vortices is seen as an indicator of mixing transition. As of yet, all statistically stationary measurements of velocity in the RTI have only used PIV to measure velocity in the $x$-$y$ plane, since these are the two dominant velocity directions. However, the application of stereoscopic PIV in the $y$-$z$ plane could be used to measure the $u$ velocity

component normal to the PIV sheet while simultaneously measuring the streamwise vorticity and evaluating the mixing transition point. These diagnostic advances would be invaluable to the characterization of the Rayleigh-Taylor instability fully-turbulent regime.

# Appendices

# APPENDIX A

# RTI TURBULENT/NON-TURBULENT INTERFACE

## A.1 Introduction

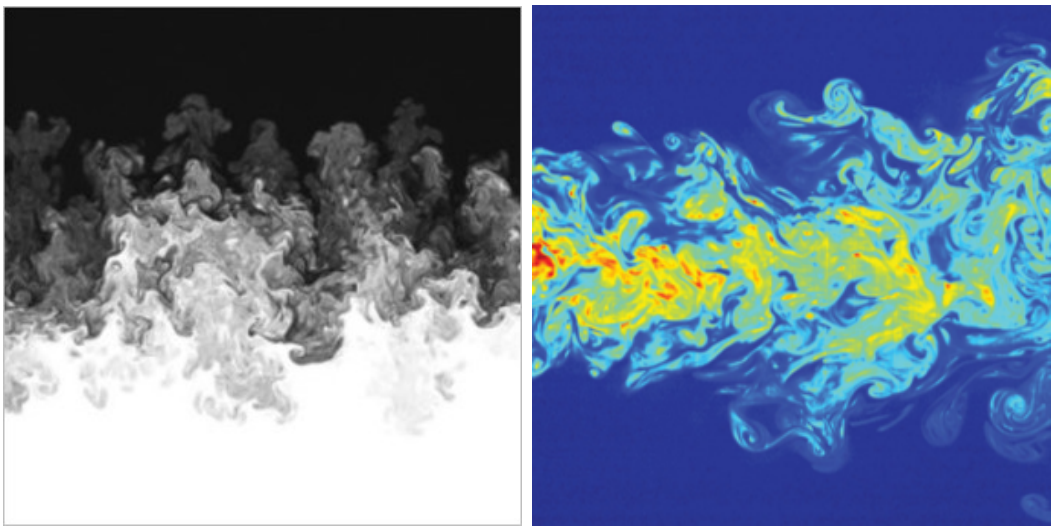

Figure A.1: Left: Cross section image of an RTI direct numerical simulation [110]. Right: Cross section image of a turbulent jet experiment [140].

The fully-turbulent Rayleigh-Taylor instability is an example of a flow with localized turbulence. To understand why, consider the left image of Figure A.1, showing a volume fraction cross section from an RTI direct numerical simulation [110]. The flow in the center of the region shows many of the characteristics of a turbulent flow: stochastic motion of the bubbles and spikes, a wide range of scales, and vortical structures. However, far outside the mixing region, the flow looks distinctly non-turbulent, with no vorticity, mixing, or structure. The localization of turbulence occurs in many different phenomena, such as turbulent jet flows (also pictured in Figure A.1), shear layers, boundary layers, and wakes. One question that may arise then is the nature of the transition between the turbulent region in the core of the mixing layer and the non-turbulent region far from the core.

The first work to seriously consider this transition was that of Corrsin and Kistler [141], in which they analyzed the intermittent turbulent behavior of a number of different localized turbulent flows. Through their hotwire measurements, they developed a framework for describing this transition in terms of a turbulent/non-turbulent interface (TNTI). This separated the zone of transition into three clear regions. The first is a thin interface, having thickness $l_I$, at which the turbulence decreases rapidly. This interface need not be at a static location, and in fact may have a convoluted shape. The region outside of this interface in which the turbulence intensity is small and the flow is mostly irrotational is termed the external layer. Meanwhile, the region directly inside the interface where the flow approaches the conditions indicative of the turbulent core is called the adjustment layer.

Since the work of Corrsin and Kistler [141], many other theoretical and experimental works have been performed to answer questions about the nature of the TNTI. Townsend [142] described the characteristics of the TNTI for a variety of different shear flows. Bisset et al. [143] analyzed the TNTI bounding a wake using previously captured DNS results, showing that many vorticity and velocity variances were nearly constant in the adjustment layer and dropped rapidly to zero at the interface. Combined PIV/PLIF experiments conducted by Westerweel et al. [140] on a turbulent jet were able to show a step change in passive scalar concentration at the interface. This work also recognized that small scale vortical motion at the interface was more impactful towards mixing than the processes of entrainment, stirring, and diffusion typically used to describe turbulent mixing [49]. Chauhan et al. [144] conducted experiments on a boundary layer and determined the location of the interface using a novel thresholding method that looked at the magnitude of variation in the velocity fluctuations in a small window. They were also able to show the strong impact of small-scale vortical motion at the interface.

Based on these previous results, we may then wonder if the same TNTI phe-

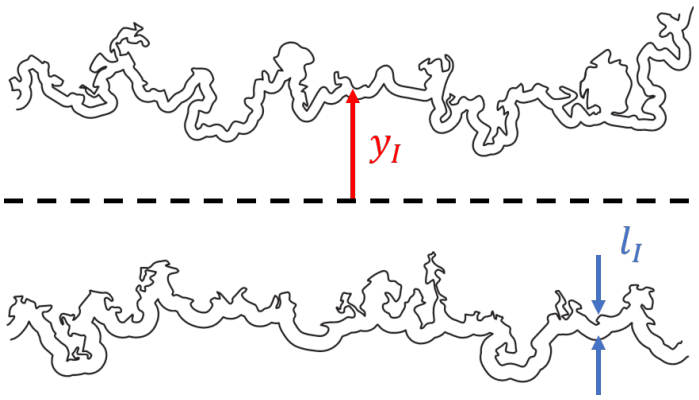


Figure A.2: A schematic of the turbulent/non-turbulent interface bounding the turbulent region of an RTI mixing layer.

nomenology is present in the case of RTI. Looking again at the left hand side of Figure A.1, this seems to be qualitatively true. While the bubble and spike structures seem to have broken up, there is still a distinct interface at the bubble and spike fronts that seems to bound the region of turbulence from the quiescent outer flow. This allows us to reformulate our image of RTI in terms of the presence of a TNTI, as in Figure A.2. There are two relevant interfaces, that at the bubble front and at the spike front. For the purpose of this work, we only consider the bubble front interface, as noise in the measurement prevented the accurate measure of the spike front interface. The bubble front interface varies in distance from the geometric centerline, $y_I$, at different $x$ locations. Meanwhile, it has a mean thickness, $l_I$, within which the flow transitions rapidly from an irrotational and nearly quiescent state to a turbulent state. In this framework we can then ask a variety of questions:

1. What range of values can $y_I$ take on and how frequently does it take on a certain value?

2. What is the thickness of the interface, $l_I$?

3. How do the velocity and vorticity variances change across the interface?

4. How does the volume fraction change across the interface?

5. Where is molecular mixing happening most in the flow? At the interface, or far within it?

To answer these questions, we utilize our PIV/LIF measurements to determine the location of the interface for an RTI flow and perform a conditional averaging method to determine the values of certain quantities in terms of the distance from the interface.

## A.2 Analysis Method

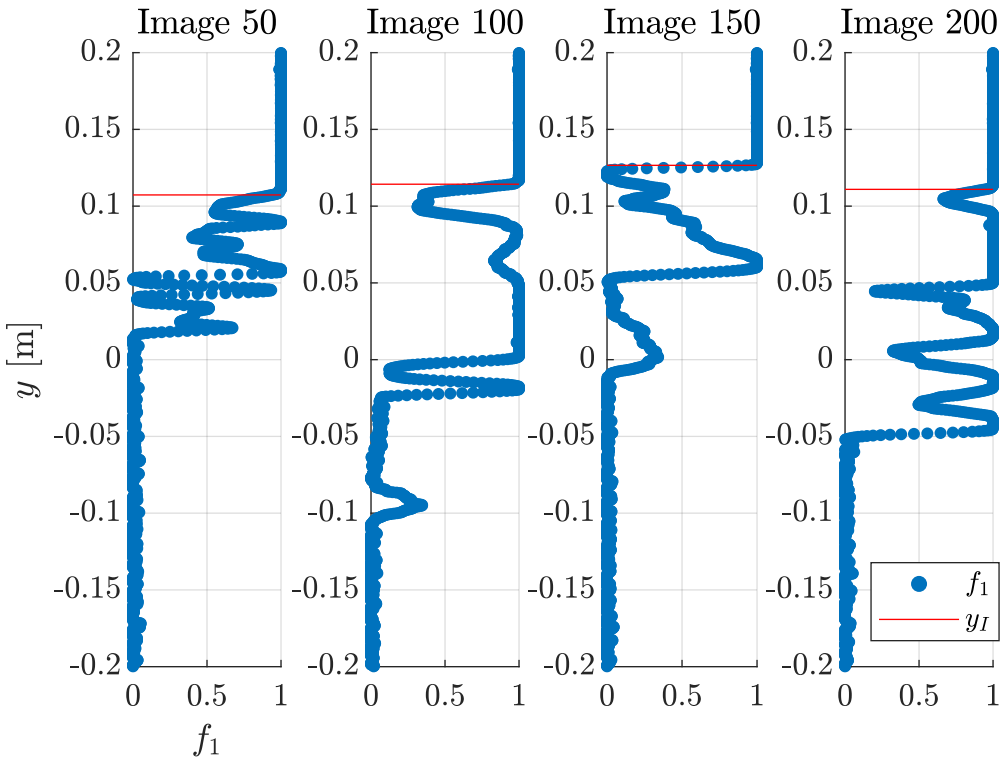


Figure A.3: Four instantaneous measurements of the volume fraction profile, found using LIF, together with the bubble interface location found using a 95 % threshold.

A challenge in most studies of the TNTI is in accurately defining the location of the interface, $y_I$. In the case of shear flows interrogated using PIV, it is possible to use the magnitude of the vorticity as an indicator between the turbulent and non-turbulent regions. Chauhan et al. [144] measured the variation of turbulent kinetic

energy measurements in the vicinity of a PIV vector to determine if the vector was in a non-turbulent location. It is also possible to use the presence of a passive scalar to determine the interface location. For this work, we choose to define the bubble TNTI as the uppermost location where the instantaneous heavy fluid volume fraction, $f_1$, is equal to 95 %. Four example volume fraction profiles and the corresponding bubble TNTI location for each profile are shown in Figure A.3.

For each instantaneous volume fraction and velocity profile, it is then possible to define a new normalized vertical coordinate, $(y - y_I)/h$ which represents a non-dimensional distance from the bubble interface, with the mixing width used as the normalization factor. In this formulation, negative values of the normalized vertical coordinate represent locations in the adjustment layer and positive values represent locations in the external layer. From the combined set of instantaneous profiles, it is then possible to define a conditional averaging technique on any spatially variable quantity $\phi$ in terms of distance to the interface, $\langle\phi\rangle_I((y-y_I)/h)$, defined by equation A.1.

$$\langle\phi\rangle_I((y - y_I)/h) = \frac{1}{N}\sum_{i=1}^{N}\phi_i((y - y_I)/h) \tag{A.1}$$

This conditional averaging technique may be used on many of the volume fraction and velocity statistics previously shown in this work.

## A.3 Results

The first questions we may consider is the range of values which the interface location, $y_I$, may take on. Figure A.4 shows the probability density function of the normalized interface location, $Y_I = (y_I - y_0)/h$ for the Re = 4050 experiment. Overall, there is great variation in the values which $Y_I$ may take on, being as great as much as 40 % greater than the mixing width, and in some instances even proceeding below the

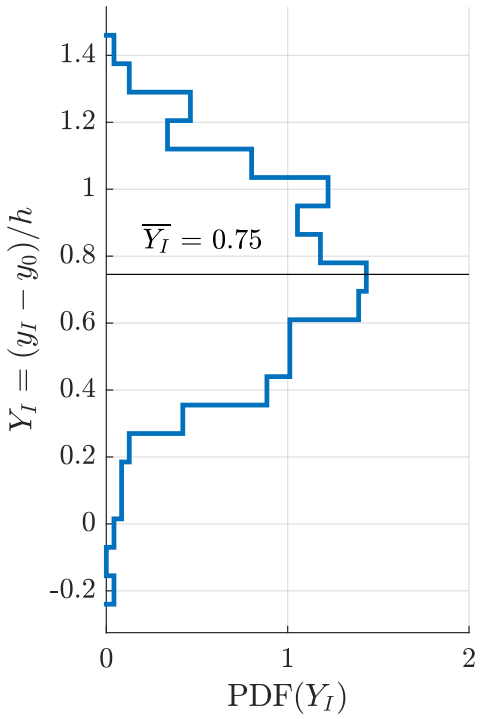


Figure A.4: The probability density function of the normalized interface location, $Y_I$, for the Re = 4050 case.

geometric centerline. Meanwhile, the mean position of the interface occurs at a value of $Y_I = 0.75$. Already upon inspection of this PDF, we see a different understanding of the nature of the RTI interface. While previous works have often perceived the mixing extent of the bubble to penetrate a depth of $h$ into the heavy fluid, it is clear that the penetration is much more convoluted, sometimes proceeding much farther than this value.

With the measurements of the interface location for each instantaneous profile computed, we may begin to show conditionally averaged profiles of various quantities. The first is the conditionally averaged volume fraction profile, shown in Figure A.5 for the Re = 4050 experiment. As one moves from the external layer past the interface, there is a clear step decrease in volume fraction. This step corroborates the understanding of the TNTI as being a thin layer in which there are dramatic changes to the fluid properties. It also explains why the interface is so visible in visualizations

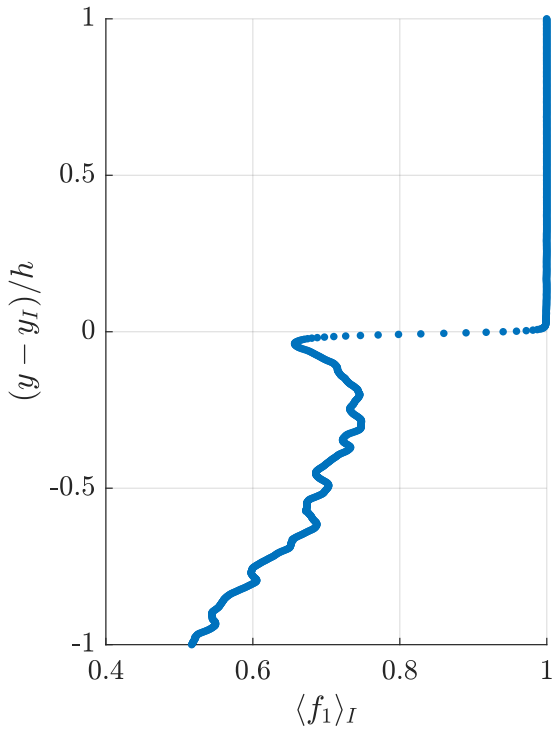


Figure A.5: The profile of the interface conditionally averaged volume fraction, $\langle f_1 \rangle_I$, for the Re = 4050 experiment.

of RTI flows, since there is a sharp contrast at the location of the interface.

This step change is followed by a slight increase until a depth of around $0.2h$ below the interface, followed by a gradual and nearly linear decrease, culminating at a volume fraction of 0.5 at a depth of $h$ from the interface. The slight increase is not seen in the TNTI of shear flows, but has a simple explanation in the context of an RTI flow. In order to explain, consider a Mie scattering visualization image of an example bubble, taken at the Re = 4050 downstream location, shown in Figure A.6. The bubble is composed mostly of light fluid that has penetrated into the heavy material. As it moves upwards, it leaves behind in its path a wake of mixing, the result of KHI rollups between it and the falling spike material. However, the bubble itself retains much of its shape and light density material, not immediately mixing with the fluid it is penetrating. As a result, the volume fraction of the bubble is smaller than the volume fraction of the mixed fluid immediately in its wake, explaining the inversion

Figure A.6: A mie scattering visualization image taken at the Re = 4050 downstream location, showing the general shape of the bubble structure

that occurs in the volume fraction profile.

Having noticed the defect which occurs in the volume fraction at the interface, it is also important to consider if the velocity fluctuations show a similar trend. Figure A.7 show the profiles of the square root of the conditionally averaged squared velocity fluctuations, $\langle u'u' \rangle_I^{1/2}$ and $\langle v'v' \rangle_I^{1/2}$. Both profiles are normalized by the Goncharov model bubble velocity, $v_\infty$. The profiles show that there again is a velocity defect at the interface, suddenly increasing as one moves from the external layer, past the interface, and into the adjustment layer. More interestingly, the value of both the horizontal and vertical velocity fluctuation through the adjustment layer is nearly constant. This seems to suggest that inside the turbulent region the properties of the turbulence are nearly constant. This again stands in contrast to the typical view of the RTI mixing layer, which considers that the turbulence intensity varies gradually as one moves from the centerline of the mixing region to the outer edge.

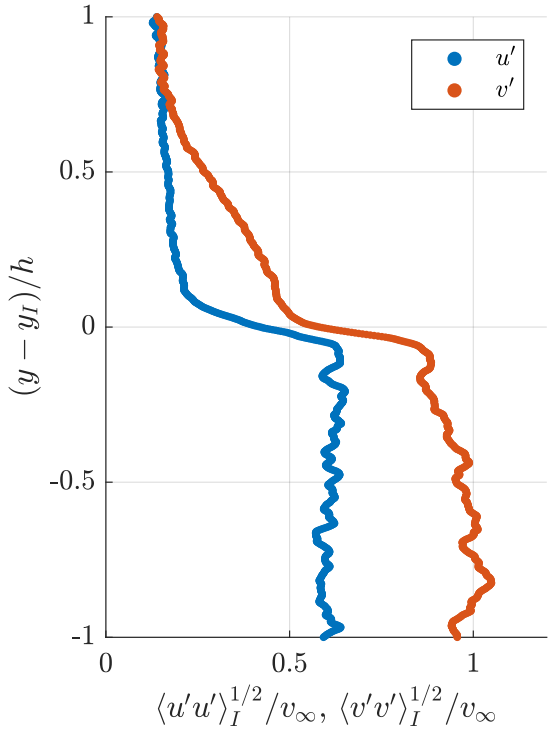


Figure A.7: The profile of the interface conditionally averaged horizontal and vertical velocity fluctuations, $\langle u'u' \rangle_I^{1/2}$ and $\langle v'v' \rangle_I^{1/2}$, for the Re = 4050 experiment, normalized by the Goncharov bubble velocity, $v_\infty$.

It seems actually that the variation is steep, occurring at the TNTI, and it is simply the variation in location of the TNTI which makes it appear that the conventionally averaged turbulence intensity varies gradually.

Upon looking at the profile of the conditionally averaged vorticity, Figure A.8, this view is further confirmed. Even more than in the conditionally averaged velocity fluctuation profile, there is a sharp defect in the vorticity at the interface, with the strength of the vorticity being nearly homogenous in the external layer and in the adjustment layer. There is a peak in vorticity specifically at the interface, suggesting that as the bubble penetrates the heavy fluid, it pushes away material in such a way that it rapidly increases the vorticity at the tip. This stands in direct contrast to the concept that the majority of vorticity is formed behind the bubble tip in the region where the bubble and spike shear past one another and develop KHI rollups. Since

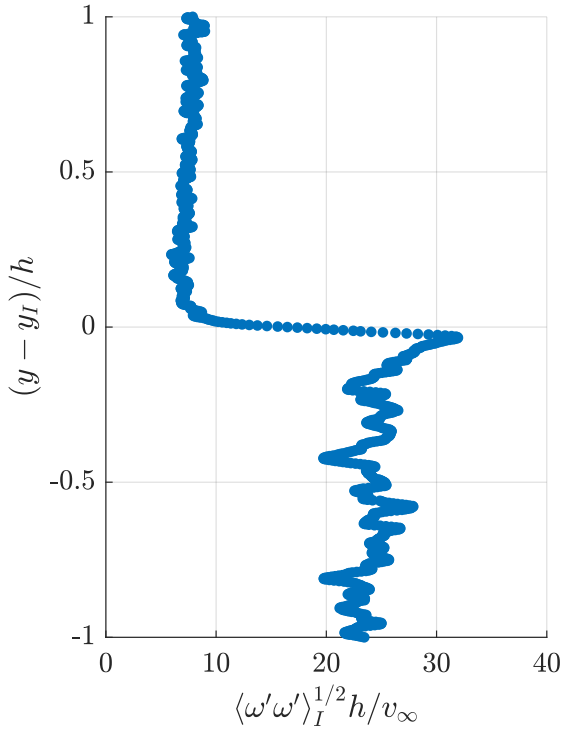


Figure A.8: The profile of the interface conditionally averaged spanwise vorticity, $\langle \omega'\omega' \rangle_I^{1/2}$, for the Re = 4050 experiment, normalized by the Goncharov bubble velocity, $v_\infty$, and the mixing height, $h$.

vorticity is vital in the process of entraining, stirring, and diffusing fluid, eventually leading to molecular mixing, this would imply that a significant amount of mixing is happening at the edge of the interface, and not in the core.

To consider the topic of molecular mixing in more detail, we consider the profile of the conditionally averaged scalar dissipation, $\langle \chi \rangle_I$, presented in Figure A.9. Here, we computed the instantaneous scalar dissipation using the same methodology as described in Section 4.2, but applied the conditional averaging technique, rather than conventional averaging. To emphasize the differences in scalar dissipation, the figure is presented on a semi-log axis. In the external layer, the fluid is mostly pure heavy fluid, leading to no concentration gradients and a nearly zero measurement of the scalar dissipation. However, at the interface, where there is a sharp defect in the concentration (as shown in Figure A.5), there is a very large magnitude of scalar dis-

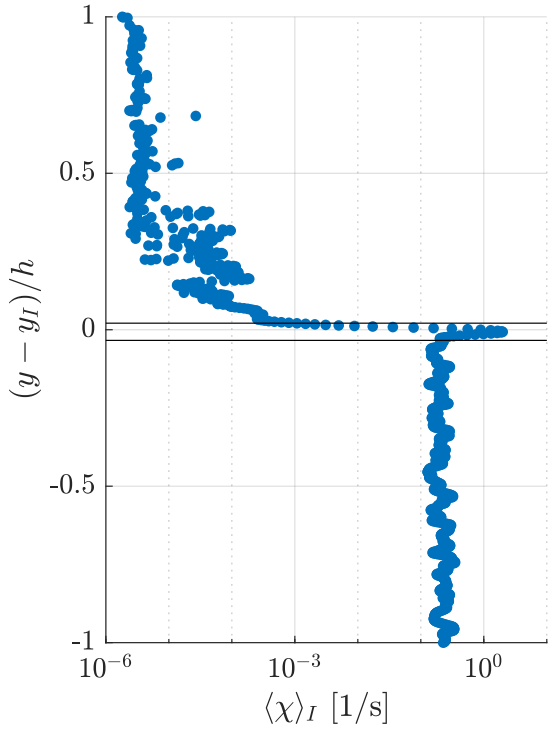


Figure A.9: The profile of the interface conditionally averaged scalar dissipation, $\langle\chi\rangle_I$, for the Re = 4050 experiment.

sipation. In the adjustment layer, the gradients in concentration are less pronounced, leading to an overall lower value, approximately one order of magnitude smaller than that at the interface. Surprisingly, the value of scalar dissipation in this region is nearly constant through the entire adjustment layer.

The scalar dissipation profile is interesting in that it seems to clearly capture a small region of increased gradients in the vicinity of the interface. From the schematic of the TNTI, and our understanding that it represents a sharp transition between the external and adjustment layer, we can use this region of large gradients to help define the width of the interface. We select the region where the value of the scalar dissipation is greater than the average value in the adjustment layer, and define this as the interface region. This region is represented as being between the two black lines in Figure A.9. Based on this measurement, we find that the interface has a thickness of $l_I = 0.04h$. Similar to our analysis technique in Section 4.2, we can

capture the measurements of the total mixing rate by taking the integral of the scalar dissipation profile along the normalized $y$ axis. One question we may have is whether the bulk of the mixing is occurring at the interface, or in the adjustment layer. To answer this, we computed the total mixing rate in the interface region and the total mixing rate in the adjustment layer. The computation reveals that the total mixing rate in the interface region comprises 13 % of the total mixing rate in the entire flow, despite the fact that the interface only accounts for 4 % of the spatial width. Based on this result, we again recognize that small-scale mixing due to steep gradients at the interface contribute significantly to the total amount of mixing in the flow.

## A.4 Conclusions

Through the simultaneous capture of density and velocity statistics in this spatially evolving RTI flow, we present the first (to the extent of the authors knowledge) experimental measurements of the characteristics of the TNTI for a buoyancy-driven flow. The TNTI shows some clear distinctions from experimental results found in shear-driven flows, most notably a more complex conditionally averaged volume fraction profile in the vicinity of the interface. However, many other attributes, such as the wide variety of interface values, the velocity defect at the interface, and the importance of small-scale mixing at the interface are similar to those in shear flows.

Most importantly, these results challenge the conventional knowledge on the shape of profiles in RTI flows. Most experimental and simulation works show parabolic profiles of values such as the turbulent mass flux, the density-specific-volume correlation, the Reynolds stresses, the velocity fluctuations, and other pertinent values across the mixing width. According to this analysis, the more correct way to interpret the variation of these values across the mixing width is to assume them to be nearly uniform in the adjustment layer and core of the flow, and to only be modulated by the location of the interface, which can vary significantly. If a stochastic model for the variation

of the interface could be found which also described the value of these turbulence parameters in the core, the description of the RTI flow could be simplified to only be determined by values at a single point in the core and knowledge about the interface location, drastically simplifying most models.

For such an interface model to be formed, one would need to know not just the probability density function of the interface location, but also the way that it varies in space. To accomplish this experimentally, some sort of spectral information on the interface movement must be captured, again emphasizing the need for high-speed measurements of the interface or of the velocity conditions in the gas tunnel. Furthermore, it is uncertain the universality of these results with varying Atwood number, Schmidt number, or spectral conditions of the initial condition. All of these questions may pave the future of the development of new diagnostics to conduct more advanced experiments in the RTI field.

## REFERENCES


[1] S. Woosley and T. Weaver. The Physics of Supernova Explosions. *Annual Review of Astronomy and Astrophysics*, 24(1):205–253, 2002. ISSN 0066-4146. doi: 10.1146/annurev.astro.24.1.205.

[2] E. Mueller and W. D. Arnett. Carbon combustion supernovae - Numerical studies of the final evolution of degenerate carbon-oxygen cores. *The Astrophysical Journal*, 307:619–643, 1986. ISSN 0004-637X. doi: 10.1086/164448.

[3] E. Livne and D. Arnett. On the instability of deflagration fronts in white dwarfs. *The Astrophysical Journal*, 415:L107, 1993. ISSN 0004-637X. doi: 10.1086/187044.

[4] M. Zingale, S. E. Woosley, C. A. Rendleman, M. S. Day, and J. B. Bell. Three-dimensional numerical simulations of Rayleigh-Taylor unstable flames in Type Ia supernovae. *The Astrophysical Journal*, 632(2):1021–1034, 2005. ISSN 0004-637X. doi: 10.1086/433164.

[5] R. Betti and O. A. Hurricane. Inertial-confinement fusion with lasers. *Nature Physics*, 12(5):435–448, May 2016. ISSN 1745-2473. doi: 10.1038/nphys3736.

[6] J. R. Freeman, M. J. Clauser, and S. L. Thompson. Rayleigh-taylor instabilities in inertial-confinement fusion targets. *Nuclear Fusion*, 17(2):223–230, 1977. ISSN 1741-4326. doi: 10.1088/0029-5515/17/2/005.

[7] John D Lindl, Robert L McCrary, and E Michael Campbell. Progress towards ingnition and burn propagation in Inertial Confinement. *Physics Today*, 45(9): 32, 1992.

[8] J. Sanz. Self-consistent analytical model of the Rayleigh-Taylor instability in inertial confinement fusion. *Physical Review Letters*, 73(20):2700–2703, 1994. ISSN 0031-9007. doi: 10.1103/PhysRevLett.73.2700.

[9] A. R. Piriz. Hydrodynamic instability of ablation fronts in inertial confinement fusion. *Physics of Plasmas*, 8(3):997–1002, 2001. ISSN 1070-664X. doi: 10.1063/1.1344194.

[10] R. Betti, V. N. Goncharov, R. L. McCrory, and C. P. Verdon. Growth rates of the ablative Rayleigh–Taylor instability in inertial confinement fusion. *Physics of Plasmas*, 5(5):1446–1454, 2002. ISSN 1070-664X. doi: 10.1063/1.872802.

[11] S. Atzeni and J. Meyer-ter Vehn. *The Physics of Inertial Fusion*. 2004. doi: 10.1093/acprof:oso/9780198562641.001.0001.

[12] V. Bychkov, M. Modestov, V. Akkerman, and L. E. Eriksson. The Rayleigh-Taylor instability in inertial fusion, astrophysical plasma and flames. In *Plasma Physics and Controlled Fusion*, volume 49, pages 513–520, 2007. doi: 10.1088/0741-3335/49/12B/S49.

[13] J. C. Beale and R. D. Reitz. Modeling spray atomization with the Kelvin-Helmholtz/Rayleigh-Taylor hybrid model. *Atomization and Sprays*, 9(6):623–650, 1999. ISSN 1044-5110. doi: 10.1615/atomizspr.v9.i6.40.

[14] C. Clanet and G. Searby. First experimental study of the Darrieus-Landau instability. *Physical Review Letters*, 80(17):3867–3870, April 1998. ISSN 1079-7114. doi: 10.1103/PhysRevLett.80.3867.

[15] S. Zaleski and P. Julien. Numerical simulation of Rayleigh-Taylor instability for single and multiple salt diapirs. *Tectonophysics*, 206(1-2):55–69, May 1992. ISSN 0040-1951. doi: 10.1016/0040-1951(92)90367-F.

[16] Z. G. Ji. *Hydrodynamics and Water Quality: Modeling Rivers, Lakes, and Estuaries*. 2008. ISBN 0470135433.

[17] J. R. Garratt. Review: the atmospheric boundary layer. *Earth-Science Reviews*, 37(1-2):89–134, October 1994. ISSN 0012-8252. doi: 10.1016/0012-8252(94)90026-4.

[18] D. D. Gray and A. Giorgini. The validity of the Boussinesq approximation for liquids and gases. *International Journal of Heat and Mass Transfer*, 19(5): 545–551, May 1976. ISSN 0017-9310. doi: 10.1016/0017-9310(76)90168-X.

[19] D H Sharp. An overview of Rayleigh-Taylor instability. *Physica D: Nonlinear Phenomena*, 12(1-3), 1984. ISSN 0167-2789. doi: 10.1016/0167-2789(84)90510-4.

[20] J. W. S. Lord Rayleigh. Investigation of the Character of the Equilibrium of an Incompressible Heavy Fluid of Variable Density. *Proc. London Math. Soc.*, 14(39):170–177, 1883.

[21] G I Taylor. The Instability of Liquid Surfaces when Accelerated in a Direction Perpendicular to their Planes. I. *Proceedings of the Royal Society A: Mathematical, Physical and Engineering Sciences*, 201(1065):192–196, March 1950. ISSN 1364-5021. doi: 10.1098/rspa.1950.0052.

[22] S. Chandrasekhar. Hydrodynamic and hydromagnetic stability, January 1961.

[23] R. Menikoff, R. C. Mjolsness, D. H. Sharp, and C. Zemach. Unstable normal mode for Rayleigh-Taylor instability in viscous fluids. *Physics of Fluids*, 20(12): 2000–2004, 1977. ISSN 1070-6631. doi: 10.1063/1.861831.

[24] M. S. Plesset and C. G. Whipple. Viscous effects in Rayleigh-Taylor instability. *Physics of Fluids*, 17(1):1–7, 1974. ISSN 1070-6631. doi: 10.1063/1.1694570.

[25] D. J. Lewis. The Instability of Liquid Surfaces when Accelerated in a Direction Perpendicular to their Planes. II. *Proceedings of the Royal Society A: Mathematical, Physical and Engineering Sciences*, 202(1068):81–96, 1950. ISSN 1364-5021. doi: 10.1098/rspa.1950.0086.

[26] David Layzer. On the Instability of Superposed Fluids in a Gravitational Field. *The Astrophysical Journal*, 122:1, 1955. ISSN 0004-637X. doi: 10.1086/146048.

[27] G Birkhoff and D Carter. Rising plane bubbles. *Journal of Mathematics and Mechanics*, 6(6):769–779, 1957. doi: 10.2307/24900621.

[28] V. N. Goncharov. Analytical Model of Nonlinear, Single-Mode, Classical Rayleigh-Taylor Instability at Arbitrary Atwood Numbers. *Physical Review Letters*, 88(13):134502, March 2002. ISSN 0031-9007. doi: 10.1103/PhysRevLett.88.134502.

[29] G Dimonte, P. Ramaprabhu, D. L. Youngs, M. J. Andrews, and R. Rosner. Recent advances in the turbulent Rayleigh-Taylor instability. In *Physics of Plasmas*, volume 12, pages 1–6, 2005. ISBN 0563012005. doi: 10.1063/1.1871952.

[30] S. W Haan. Onset of nonlinear saturation for Rayleigh-Taylor growth in the presence of a full spectrum of modes. *Physical Review A*, 39(11):5812–5825, 1989. ISSN 1050-2947. doi: 10.1103/PhysRevA.39.5812.

[31] D. Ofer, D. Shvarts, Z. Zinamon, and S. A. Orszag. Mode coupling in nonlinear Rayleigh-Taylor instability. *Physics of Fluids B*, 4(11):3549–3561, November 1992. ISSN 0899-8221. doi: 10.1063/1.860362.

[32] D. Shvarts, U. Alon, D. Ofer, R. L. McCrory, and C. P. Verdon. Nonlinear evolution of multimode Rayleigh-Taylor instability in two and three dimensions. *Physics of Plasmas*, 2(6):2465–2472, 1995. ISSN 1070-664X. doi: 10.1063/1.871476.

[33] W. Cabot. Comparison of two- and three-dimensional simulations of miscible Rayleigh-Taylor instability. *Physics of Fluids*, 18(4), 2006. ISSN 1070-6631. doi: 10.1063/1.2191856.

[34] J R Ristorcelli and T. T. Clark. Rayleigh-Taylor turbulence: Self-similar analysis and direct numerical simulations. *Journal of Fluid Mechanics*, 507(507): 213–253, May 2004. ISSN 0022-1120. doi: 10.1017/S0022112004008286.

[35] K.I. Read. Experimental investigation of turbulent mixing by Rayleigh-Taylor instability. *Physica D: Nonlinear Phenomena*, 12:45–58, 1984. ISSN 0167-2789. doi: 10.1016/0167-2789(84)90513-X.

[36] D L Youngs. Numerical simulation of turbulent mixing by Rayleigh-Taylor instability. *Physica D: Nonlinear Phenomena*, 12(1-3):32–44, 1984. ISSN 0167-2789. doi: 10.1016/0167-2789(84)90512-8.

[37] N. N. Anuchina, Y.A. Kucherenko, V. E. Neuvazhaev, V. N. Ogibina, L. I. Shibarshov, and V. G. Yakovlev. Turbulent mixing at an accelerating interface between liquids of different density. *Fluid Dynamics*, 13(6):916–920, 1978. ISSN 0015-4628. doi: 10.1007/BF01050969.

[38] A W Cook and Paul E Dimotakis. Transition stages of Rayleigh-Taylor instability between miscible fluids. *Journal of Fluid Mechanics*, 443:69–99, 2001. ISSN 0022-1120. doi: 10.1017/S0022112001005377.

[39] M J Andrews and D. B. Spalding. A simple experiment to investigate two-dimensional mixing by Rayleigh-Taylor instability. *Physics of Fluids A*, 2(6): 922–927, June 1990. ISSN 0899-8213. doi: 10.1063/1.857652.

[40] P F Linden, J M Redondo, and D L Youngs. Molecular mixing in Rayleigh-Taylor instability. *Journal of Fluid Mechanics*, 265(September):97–124, 1994. ISSN 0022-1120. doi: 10.1017/S0022112094000777.

[41] G. Dimonte and Marilyn Schneider. Density ratio dependence of Rayleigh–Taylor mixing for sustained and impulsive acceleration histories. *Citation: Physics of Fluids*, 12(304), 2000. doi: 10.1063/1.870309.

[42] A Banerjee and M J Andrews. Statistically steady measurements of Rayleigh-Taylor mixing in a gas channel. *Physics of Fluids*, 18(3), 2006. ISSN 1070-6631. doi: 10.1063/1.2185687.

[43] D. H. Olson and J W Jacobs. Experimental study of Rayleigh–Taylor instability with a complex initial perturbation. *Physics of Fluids*, 21(3):034103, March 2009. ISSN 1070-6631. doi: 10.1063/1.3085811.

[44] D. L. Youngs. Three-dimensional numerical simulation of turbulent mixing by Rayleigh-Taylor instability. *Citation: Physics of Fluids A: Fluid Dynamics*, 3: 1312, 1991. doi: 10.1063/1.858059.

[45] A W Cook, W H Cabot, and Paul L. Miller. The mixing transition in Rayleigh-Taylor instability. *Journal of Fluid Mechanics*, 511:333–362, 2004. ISSN 0022-1120. doi: 10.1017/S0022112004009681.

[46] D Livescu, J R Ristorcelli, R A Gore, S H Dean, W H Cabot, and A W Cook. High-Reynolds number Rayleigh-Taylor turbulence. *Journal of Turbulence*, 10 (13):1–32, 2009. ISSN 1468-5248. doi: 10.1080/14685240902870448.

[47] G. Dimonte, D L Youngs, A. Dimits, S. Weber, M. Marinak, S. Wunsch, C. Garasi, A. Robinson, M J Andrews, P. Ramaprabhu, A. C. Calder, B. Fryxell, J. Biello, L. Dursi, P. MacNeice, K. Olson, P. Ricker, R. Rosner, F. Timmes, H. Tufo, Y. N. Young, and M. Zingale. A comparative study of the turbulent Rayleigh-Taylor instability using high-resolution three-dimensional numerical simulations: The Alpha-Group collaboration. *Physics of Fluids*, 16(5):1668–1693, May 2004. ISSN 1070-6631. doi: 10.1063/1.1688328.

[48] P. Ramaprabhu, G. Dimonte, P. Woodward, C. Fryer, G. Rockefeller, K. Muthuraman, P. H. Lin, and J. Jayaraj. The late-time dynamics of the single-mode Rayleigh-Taylor instability. *Physics of Fluids*, 24(7), 2012. ISSN 1070-6631. doi: 10.1063/1.4733396.

[49] Paul E Dimotakis. Turbulent Mixing. *Annual Review of Fluid Mechanics*, 37(1): 329–356, 2005. ISSN 0066-4189. doi: 10.1146/annurev.fluid.36.050802.122015.

[50] H W Emmons, C T Chang, and B C Watson. Taylor instability of finite surface waves. *Journal of Fluid Mechanics*, 7(2):177–193, 1960. ISSN 1469-7645. doi: 10.1017/S0022112060001420.

[51] R L Cole and R S Tankin. Experimental study of Taylor instability. *Physics of Fluids*, 16(8):1207, 1973. ISSN 0031-9171. doi: 10.1063/1.1694499.

[52] M Ratafia. Experimental investigation of Rayleigh-Taylor instability. *Physics of Fluids*, 16(8):1207, 1973. ISSN 0031-9171. doi: 10.1063/1.1694499.

[53] R. M. Davies and G I Taylor. The Mechanics of Large Bubbles Rising through Extended Liquids and through Liquids in Tubes. *Proceedings of the Royal Society A: Mathematical, Physical and Engineering Sciences*, 200(1062):375–390, 1950. ISSN 1364-5021. doi: 10.1098/rspa.1950.0023.

[54] J. T. Waddell, C. E. Niederhaus, and J. W. Jacobs. Experimental study of Rayleigh–Taylor instability: Low Atwood number liquid systems with single-mode initial perturbations. *Physics of Fluids*, 13(5):1263–1273, May 2001. ISSN 1070-6631. doi: 10.1063/1.1359762.

[55] J. P. Wilkinson and J. W. Jacobs. Experimental study of the single-mode three-dimensional Rayleigh-Taylor instability. *Physics of Fluids*, 19(12):124102, December 2007. ISSN 1070-6631. doi: 10.1063/1.2813548.

[56] G. Dimonte and Marilyn Schneider. Turbulent rayleigh-taylor instability experiments with variable acceleration. *Physical Review E - Statistical Physics, Plasmas, Fluids, and Related Interdisciplinary Topics*, 54(4):3740–3743, 1996. ISSN 1063-651X. doi: 10.1103/PhysRevE.54.3740.

[57] Y.A. Kucherenko, A.P. Pylaev, V.D. Murzakov, A.V. Belomestnih, V.N. Popov, and A.A. Tyaktev. Experimental study into the Rayleigh–Taylor turbulent mixing zone heterogeneous structure. *Laser and Particle Beams*, 21(03):375–379, July 2003. ISSN 0263-0346. doi: 10.1017/S0263034603213136.

[58] M S Roberts and J W Jacobs. The effects of forced small-wavelength, finite-bandwidth initial perturbations and miscibility on the turbulent Rayleigh-Taylor instability. *Journal of Fluid Mechanics*, 787:50–83, 2015. ISSN 1469-7645. doi: 10.1017/jfm.2015.599.

[59] V. S. Smeeton and D. L. Youngs. Experimental investigation of turbulent mixing by Rayleigh-Taylor instability (part 3). *AWE report number 0*, 35(87):1987, 1987.

[60] P F Linden and J M Redondo. Molecular mixing in Rayleigh-Taylor instability. Part I: Global mixing. *Physics of Fluids A*, 3(5):1269–1277, 1991. ISSN 0899-8213. doi: 10.1063/1.858055.

[61] S B Dalziel. Rayleigh-Taylor instability: experiments with image analysis. *Dynamics of Atmospheres and Oceans*, 20(1-2):127–153, 1993. ISSN 0377-0265. doi: 10.1016/0377-0265(93)90051-8.

[62] S B Dalziel, P F Linden, and D L Youngs. Self-similarity and internal structure of turbulence induced by Rayleigh–Taylor instability. *Journal of Fluid Mechanics*, 399:1–48, 1999. ISSN 0022-1120. doi: 10.1017/S002211209900614X.

[63] S B Dalziel, Michael D Patterson, C P Caulfield, and Imran A Coomaraswamy. Mixing efficiency in high-aspect-ratio Rayleigh-Taylor experiments. *Physics of Fluids*, 20(6), 2008. ISSN 1070-6631. doi: 10.1063/1.2936311.

[64] Andrew G.W. Lawrie and S B Dalziel. Rayleigh-Taylor mixing in an otherwise stable stratification. *Journal of Fluid Mechanics*, 688:507–527, 2011. ISSN 0022-1120. doi: 10.1017/jfm.2011.398.

[65] Dale M Snider and M J Andrews. Rayleigh-Taylor and shear driven mixing with an unstable thermal stratification. *Physics of Fluids*, 6(10):3324–3334, 1994. ISSN 1070-6631. doi: 10.1063/1.868065.

[66] G I Taylor. Statistical Theory of Turbulence, 1935.

[67] A. L. Kistler and T. Vrebalovich. Grid turbulence at large Reynolds numbers. *Journal of Fluid Mechanics*, 26(01):37, September 1966. ISSN 0022-1120. doi: 10.1017/S0022112066001071.

[68] Peter Wilson, M J Andrews, and Francis Harlow. Spectral nonequilibrium in a turbulent mixing layer. *Physics of Fluids*, 11(8):2425, July 1999. ISSN 1070-6631. doi: 10.1063/1.870103.

[69] Peter N. Wilson and M J Andrews. Spectral measurements of Rayleigh–Taylor mixing at small Atwood number. *Physics of Fluids*, 14(3):938–945, March 2002. ISSN 1070-6631. doi: 10.1063/1.1445418.

[70] P. Ramaprabhu and M. J. Andrews. Simultaneous measurements of velocity and density in buoyancy-driven mixing. *Experiments in Fluids*, 34(1):98–106, 2003. ISSN 0723-4864. doi: 10.1007/s00348-002-0538-0.

[71] P. Ramaprabhu and M J Andrews. *Experimental investigation of Rayleigh-*

*Taylor mixing at small Atwood numbers*, volume 502. Cambridge University Press, 2004. ISBN 0022112003007. doi: 10.1017/S0022112003007419.

[72] Nicholas J. Mueschke, M J Andrews, and Oleg Schilling. Experimental characterization of initial conditions and spatio-temporal evolution of a small-Atwood-number Rayleigh-Taylor mixing layer. *Journal of Fluid Mechanics*, 567:27–63, 2006. ISSN 0022-1120. doi: 10.1017/S0022112006001959.

[73] Nicholas J. Mueschke, Oleg Schilling, D L Youngs, and M J Andrews. Measurements of molecular mixing in a high-Schmidt-number Rayleigh-Taylor mixing layer. *Journal of Fluid Mechanics*, 632:17–48, 2009. ISSN 0022-1120. doi: 10.1017/S0022112009006132.

[74] W. N. Kraft, A. Banerjee, and M. J. Andrews. On hot-wire diagnostics in Rayleigh-Taylor mixing layers. *Experiments in Fluids*, 47:49–68, 2009. doi: 10.1007/s00348-009-0636-3.

[75] A Banerjee, W N Kraft, and M J Andrews. Detailed measurements of a statistically steady Rayleigh–Taylor mixing layer from small to high Atwood numbers. *Journal of Fluid Mechanics*, 659(2010):127–190, 2010. ISSN 0022-1120. doi: 10.1017/S0022112010002351.

[76] B Akula and D Ranjan. Dynamics of buoyancy-driven flows at moderately high Atwood numbers. *Journal of Fluid Mechanics*, 795:313–355, May 2016. ISSN 1469-7645. doi: 10.1017/jfm.2016.199.

[77] B. Akula, P. Suchandra, M. M. Mikhaeil, and D. Ranjan. Dynamics of unstably stratified free shear flows: an experimental investigation of coupled Kelvin–Helmholtz and Rayleigh–Taylor instability. *Journal of Fluid Mechanics*, 816:619–660, April 2017. ISSN 0022-1120. doi: 10.1017/jfm.2017.95.

[78] S. Kuchibhatla and D. Ranjan. Rayleigh-Taylor experiments. In *Volume 7: Fluids and Heat Transfer, Parts A, B, C, and D*, page 1341. ASME, November 2012. ISBN 978-0-7918-4523-3. doi: 10.1115/IMECE2012-93087.

[79] S. Kuchibhatla and D. Ranjan. Effect of initial conditions on Rayleigh–Taylor mixing: modal interaction. *Physica Scripta*, T155:014057, July 2013. ISSN 0031-8949. doi: 10.1088/0031-8949/2013/T155/014057.

[80] A. G. W. Lawrie and S. B. Dalziel. Rayleigh–Taylor mixing in an otherwise stable stratification. *Journal of Fluid Mechanics*, 688:507–527, December 2011. ISSN 0022-1120. doi: 10.1017/jfm.2011.398.

[81] Megan S. Davies Wykes and Stuart B. Dalziel. Efficient mixing in stratified flows: experimental study of a Rayleigh–Taylor unstable interface within an otherwise stable stratification. *Journal of Fluid Mechanics*, 756:1027–1057, October 2014. ISSN 0022-1120. doi: 10.1017/jfm.2014.308.

[82] John J Charonko and Katherine Prestridge. Variable-density mixing in turbulent jets with coflow. *Journal of Fluid Mechanics*, 825:887–921, 2017. ISSN 1469-7645. doi: 10.1017/jfm.2017.379.

[83] R V Morgan, W H Cabot, J A Greenough, and J W Jacobs. Rarefaction-driven Rayleigh–Taylor instability. Part 2. Experiments and simulations in the nonlinear regime. *Journal of Fluid Mechanics*, 838:320–355, 2018. ISSN 0022-1120. doi: 10.1017/jfm.2017.893.

[84] A. J. Wachtor, V. Mocko, F. F. Jebrail, and M. J. Andrews. On buoyancy driven mixing by volumetric microwave energy deposition. *International Journal of Heat and Mass Transfer*, 86:443–454, July 2015. ISSN 0017-9310. doi: 10.1016/j.ijheatmasstransfer.2015.01.112.

[85] Kyle A Baldwin, Matthew M Scase, and Richard J.A. Hill. The inhibition of the Rayleigh-Taylor instability by rotation. *Scientific Reports*, 5, 2015. ISSN 2045-2322. doi: 10.1038/srep11706.

[86] J. A. Zufiria. Bubble competition in Rayleigh–Taylor instability. *Physics of Fluids*, 31(3):440, September 1988. ISSN 0031-9171. doi: 10.1063/1.866825.

[87] L. Baker and J. R. Freeman. Heuristic model of the nonlinear Rayleigh-Taylor instability. *Journal of Applied Physics*, 52(2):655–663, February 1981. ISSN 0021-8979. doi: 10.1063/1.328793.

[88] D. Oron, L. Arazi, D. Kartoon, A. Rikanati, U. Alon, and D. Shvarts. Dimensionality dependence of the Rayleigh–Taylor and Richtmyer–Meshkov instability late-time scaling laws. *Physics of Plasmas*, 8(6):2883–2889, June 2001. ISSN 1070-664X. doi: 10.1063/1.1362529.

[89] A. R. Miles, D. G. Braun, M. J. Edwards, H. F. Robey, R. P. Drake, and D. R. Leibrandt. Numerical simulation of supernova-relevant laser-driven hydro experiments on OMEGA. *Physics of Plasmas*, 11(7):3631–3645, July 2004. ISSN 1070-664X. doi: 10.1063/1.1753274.

[90] V. Rana, H. Lim, J. Melvin, J. Glimm, B. Cheng, and D. H. Sharp. Mixing with applications to inertial-confinement-fusion implosions. *Physical Review E*, 95 (1):013203, January 2017. ISSN 2470-0045. doi: 10.1103/PhysRevE.95.013203.

[91] Y. Zhou, G. B. Zimmerman, and E. W. Burke. Formulation of a two-scale transport scheme for the turbulent mix induced by Rayleigh-Taylor and Richtmyer-Meshkov instabilities. *Physical Review E*, 65(5):056303, May 2002. ISSN 1063-651X. doi: 10.1103/PhysRevE.65.056303.

[92] I. W. Kokkinakis, D. Drikakis, D. L. Youngs, and R. J. R. Williams. Two-equation and multi-fluid turbulence models for Rayleigh–Taylor mixing. *Inter-*

*national Journal of Heat and Fluid Flow*, 56:233–250, December 2015. ISSN 0142-727X. doi: 10.1016/J.IJHEATFLUIDFLOW.2015.07.017.

[93] A. J. Favre. Review on space-time correlations in turbulent fluids. *Journal of Applied Mechanics*, 32(2):241–257, June 1965. ISSN 0021-8936. doi: 10.1115/1.3625792.

[94] J. Rotta. Statistische theorie nichthomogener turbulenz. *Zeitschrift für Physik*, 129(6):547–572, November 1951. ISSN 1434-6001. doi: 10.1007/BF01330059.

[95] C. G. Speziale. Analytical methods for the development of Reynolds-Stress closures in turbulence. *Annual Review of Fluid Mechanics*, 23(1):107–157, January 1991. ISSN 0066-4189. doi: 10.1146/annurev.fl.23.010191.000543.

[96] G. Dimonte and R. Tipton. K-L turbulence model for the self-similar growth of the Rayleigh-Taylor and Richtmyer-Meshkov instabilities. *Physics of Fluids*, 18(8):085101, August 2006. ISSN 1070-6631. doi: 10.1063/1.2219768.

[97] D. L. Youngs. The density ratio dependence of self-similar Rayleigh–Taylor mixing. *Philosophical Transactions of the Royal Society A: Mathematical, Physical and Engineering Sciences*, 371(2003):20120173, November 2013. ISSN 1364-503X. doi: 10.1098/rsta.2012.0173.

[98] E. Scannapieco and M. Brüggen. Subgrid modeling of AGN-driven turbulence in galaxy clusters. *The Astrophysical Journal*, 686(2):927–947, October 2008. ISSN 0004-637X. doi: 10.1086/591228.

[99] O. A. Hurricane, V. A. Smalyuk, K. Raman, O. Schilling, J. F. Hansen, G. Langstaff, D. Martinez, H.-S. Park, B. A. Remington, H. F. Robey, J. A. Greenough, R. Wallace, C. A. Di Stefano, R. P. Drake, D. Marion, C. M. Krauland, and C. C. Kuranz. Validation of a Turbulent Kelvin-Helmholtz

Shear Layer Model Using a High-Energy-Density OMEGA Laser Experiment. *Physical Review Letters*, 109(15):155004, October 2012. ISSN 0031-9007. doi: 10.1103/PhysRevLett.109.155004.

[100] V. A. Smalyuk, L. J. Atherton, L. R. Benedetti, R. Bionta, D. Bleuel, E. Bond, D. K. Bradley, J. Caggiano, D. A. Callahan, D. T. Casey, P. M. Celliers, C. J. Cerjan, D. Clark, E. L. Dewald, S. N. Dixit, T. Döppner, D. H. Edgell, M. J. Edwards, J. Frenje, M. Gatu-Johnson, V. Y. Glebov, S. Glenn, S. H. Glenzer, G. Grim, S. W. Haan, B. A. Hammel, E. P. Hartouni, R. Hatarik, S. Hatchett, D. G. Hicks, W. W. Hsing, N. Izumi, O. S. Jones, M. H. Key, S. F. Khan, J. D. Kilkenny, J. L. Kline, J. Knauer, G. A. Kyrala, O. L. Landen, S. Le Pape, J. D. Lindl, T. Ma, B. J. MacGowan, A. J. Mackinnon, A. G. MacPhee, J. McNaney, N. B. Meezan, J. D. Moody, A. Moore, M. Moran, E. I. Moses, A. Pak, T. Parham, H.-S. Park, P. K. Patel, R. Petrasso, J. E. Ralph, S. P. Regan, B. A. Remington, H. F. Robey, J. S. Ross, B. K. Spears, P. T. Springer, L. J. Suter, R. Tommasini, R. P. Town, S. V. Weber, and K. Widmann. Performance of High-Convergence, Layered DT Implosions with Extended-Duration Pulses at the National Ignition Facility. *Physical Review Letters*, 111(21):215001, November 2013. ISSN 0031-9007. doi: 10.1103/PhysRevLett.111.215001.

[101] Didier Besnard, Francis H. Harlow, Rick M. Rauenzahn, and Charles Zemach. Turbulent Transport Equations for Varaible-Density Turbulence and Their Relationship to Two-Field Models. Technical report, Los Alamos National Laboratory (LANL), Los Alamos, NM (United States), June 1992.

[102] D. Besnard, F. H. Harlow, and R. Rauenzahn. Conservation and transport properties of turbulence with large density variations. *Unknown*, 88, 1987.

[103] M. Gittings, R. Weaver, M. Clover, T. Betlach, N. Byrne, R. Coker, E. Dendy, R. Hueckstaedt, K. New, W. R. Oakes, D. Ranta, and R. Stefan. The

RAGE radiation-hydrodynamic code. *Computational Science & Discovery*, 1(1): 015005, November 2008. ISSN 1749-4699. doi: 10.1088/1749-4699/1/1/015005.

[104] A. Banerjee, R. A. Gore, and M. J. Andrews. Development and validation of a turbulent-mix model for variable-density and compressible flows. *Physical Review E - Statistical, Nonlinear, and Soft Matter Physics*, 82(4):046309, October 2010. ISSN 1539-3755. doi: 10.1103/PhysRevE.82.046309.

[105] K. Stalsberg-Zarling and R. A. Gore. The BHR2 turbulence model: incompressible isotropic decay, Rayleigh–Taylor, Kelvin–Helmholtz and homogeneous variable density turbulence. *LANL Report, LA-UR–11*, 4773, 2011.

[106] N. A. Denissen, J. Fung, J. M. Reisner, and M. J. Andrews. Implementation and Validation of the BHR Turbulence Model in the FLAG Hydrocode. Technical report, Los Alamos National Laboratory (LANL), Los Alamos, NM (United States), August 2012.

[107] N. A. Denissen, B. Rollin, J. M. Reisner, and M. J. Andrews. The Tilted Rocket Rig: A Rayleigh–Taylor test case for RANS models. *Journal of Fluids Engineering*, 136(9), September 2014. ISSN 0098-2202. doi: 10.1115/1.4027776.

[108] John D. Schwarzkopf, Daniel Livescu, Robert A. Gore, Rick M. Rauenzahn, and J. Raymond Ristorcelli. Application of a second-moment closure model to mixing processes involving multicomponent miscible fluids. *Journal of Turbulence*, 12:N49, January 2011. ISSN 1468-5248. doi: 10.1080/14685248.2011.633084.

[109] J. D. Schwarzkopf, D Livescu, J R Baltzer, R A Gore, and J R Ristorcelli. A Two-length Scale Turbulence Model for Single-phase Multi-fluid Mixing. *Flow, Turbulence and Combustion*, 96(1):1–43, January 2016. ISSN 1386-6184. doi: 10.1007/s10494-015-9643-z.

[110] W H Cabot and A W Cook. Reynolds number effects on Rayleigh-Taylor instability with possible implications for Type Ia supernovae. *Nature Physics*, 2(8):562–568, 2006. ISSN 1745-2473. doi: 10.1038/nphys361.

[111] J. H. Bell and R. D. Mehta. Contraction design for small low-speed wind tunnels. Technical report, 1988.

[112] E. M. Laws and J. L. Livesey. Flow through screens. *Annual Review of Fluid Mechanics*, 10(1):247–266, January 1978. ISSN 0066-4189. doi: 10.1146/annurev.fl.10.010178.001335.

[113] H. L. Dryden and G. B. Schubauer. The Use of Damping Screens for the Reduction of Wind-Tunnel Turbulence. *Journal of the Aeronautical Sciences*, 14(4):221–228, 1947. doi: 10.2514/8.1324.

[114] R. G. Cunningham. Orifice meters with supercritical compressible flow. *Trans. ASME*, 73:625–638, 1951.

[115] S B Pope. *Turbulent Flows*. IOP Publishing, November 2000. ISBN 9780511840531. doi: 10.1088/0957-0233/12/11/705.

[116] A. Melling. Tracer particles and seeding for particle image velocimetry. *Measurement Science and Technology*, 8(12):1406–1416, December 1997. ISSN 0957-0233. doi: 10.1088/0957-0233/8/12/005.

[117] I Grant. Particle image velocimetry : A review. *Proceedings of the Institution of Mechanical Engineers*, 1997.

[118] C. R. Weber, N. S. Haehn, J. G. Oakley, D. A. Rothamer, and R. Bonazza. An experimental investigation of the turbulent mixing transition in the Richtmyer-Meshkov instability. *Journal of Fluid Mechanics*, 748:457–487, June 2014. ISSN 1469-7645. doi: 10.1017/jfm.2014.188.

[119] M. Mohaghar, J. Carter, B. Musci, D. Reilly, J. McFarland, and D. Ranjan. Evaluation of turbulent mixing transition in a shock-driven variable-density flow. *Journal of Fluid Mechanics*, 831:779–825, 2017. ISSN 1469-7645. doi: 10.1017/jfm.2017.664.

[120] M. Mohaghar, J. Carter, G. Pathikonda, and D. Ranjan. The transition to turbulence in shock-driven mixing: Effects of Mach number and initial conditions. *Journal of Fluid Mechanics*, pages 595–635, 2019. ISSN 1469-7645. doi: 10.1017/jfm.2019.330.

[121] R. D. Keane and R. J. Adrian. Theory of cross-correlation analysis of PIV images. *Applied Scientific Research*, 49(3):191–215, July 1992. ISSN 0003-6994. doi: 10.1007/BF00384623.

[122] D. P. Hart. PIV error correction. *Experiments in Fluids*, 29(1):13–22, July 2000. ISSN 0723-4864. doi: 10.1007/s003480050421.

[123] M Raffel, CE Willert, F Scarano, CJ Kähler, and ST Wereley. *Particle image velocimetry: a practical guide*. 2018.

[124] B. Wieneke. PIV uncertainty quantification from correlation statistics. *Measurement Science and Technology*, 26(7):074002, July 2015. ISSN 0957-0233. doi: 10.1088/0957-0233/26/7/074002.

[125] M. C. Thurber. Acetone laser-induced fluorescence for temperature and multiparameter imaging in gaseous flows. *Thesis (PhD). STANFORD UNIVERSITY, Source DAI-B 60/04, p. 1822, Oct 1999, 137 pages.*, 1999.

[126] J. S. Bendat and A. G. Piersol. *Random data: analysis and measurement procedures*, volume 729. John Wiley & Sons, 2011.

[127] A. Sciacchitano and B. Wieneke. PIV uncertainty propagation. *Measurement Science and Technology*, 27(8):084006, August 2016. ISSN 0957-0233. doi: 10.1088/0957-0233/27/8/084006.

[128] C. R. Wilke. A viscosity equation for gas mixtures. *The Journal of Chemical Physics*, 18(4):517–519, 1950. ISSN 0021-9606. doi: 10.1063/1.1747673.

[129] F. H. Champagne, Y. H. Pao, and I. J. Wygnanski. On the two-dimensional mixing region. *Journal of Fluid Mechanics*, 74(2):209–250, 1976. ISSN 1469-7645. doi: 10.1017/S0022112076001778.

[130] D Livescu, J R Ristorcelli, M R Petersen, and R A Gore. New phenomena in variable-density Rayleigh–Taylor turbulence. *Physica Scripta*, T142(T142): 014015, December 2010. ISSN 0031-8949. doi: 10.1088/0031-8949/2010/T142/014015.

[131] A. N. Kolmogorov. The local structure of turbulence in incompressible viscous fluid for very large Reynolds numbers. *C. R. Acad. Sci. URSS*, 30:301–305, 1941.

[132] R. A. Antonia. Conditional Sampling in Turbulence Measurement. *Annual Review of Fluid Mechanics*, 13(1):131–156, January 1981. ISSN 0066-4189. doi: 10.1146/annurev.fl.13.010181.001023.

[133] P. V. Danckwerts. The definition and measurement of some characteristics of mixtures. *Applied Scientific Research, Section A*, 3(4):279–296, July 1952. ISSN 0365-7132. doi: 10.1007/BF03184936.

[134] C D Tomkins, B J Balakumar, G Orlicz, K P Prestridge, and J R Ristorcelli. Evolution of the density self-correlation in developing Richtmyer-Meshkov turbulence. *Journal of Fluid Mechanics*, 735:288–306, 2013. ISSN 0022-1120. doi: 10.1017/jfm.2013.430.

[135] D. L. Youngs. Numerical simulation of mixing by rayleigh-taylor and richtmyer-meshkov instabilities. *Laser and Particle Beams*, 12(4):725–750, 1994. ISSN 1469-803X. doi: 10.1017/S0263034600008557.

[136] T. Cebeci and A. M. O. Smith. Analysis of turbulent boundary layers. *Applied Mathematics and Mechanics (An Internation Series of Monographs)*, (15 , Publ. Academic Press Inc. New York (1974)):404, 1974. ISSN 0021-8936. doi: 10.1115/1.3423784.

[137] N R Panchapakesan and D J L Lumley. Turbulence measurements in axisymmetric jets of air and helium. Part 1. Air jet. *J. FZuidMech*, 246:197–223, 2019. doi: 10.1017/S0022112093000096.

[138] N. R. Panchapakesan and J. L. Lumley. Turbulence Measurements in Axisymmetric Jets of Air and Helium. Part 2. Helium Jet. *Journal of Fluid Mechanics*, 246:225–247, 1993. ISSN 1469-7645. doi: 10.1017/S0022112093000102.

[139] J. L. Lumley. Computational Modeling of Turbulent Flows. *Advances in Applied Mechanics*, 18(C):123–176, January 1979. ISSN 0065-2156. doi: 10.1016/S0065-2156(08)70266-7.

[140] J Westerweel, C Fukushima, J M Pedersen, and J. C.R. Hunt. Momentum and scalar transport at the turbulent/non-turbulent interface of a jet. *Journal of Fluid Mechanics*, 631:199–230, 2009. ISSN 0022-1120. doi: 10.1017/S0022112009006600.

[141] S. Corrsin and A. L. Kistler. Free-stream boundaries of turbulent flows. *NACA report 1244*, pages 1033–1064, 1955.

[142] A. A. Townsend. The structure of turbulent shear flow, 1976.

[143] D. K. Bisset, J. C. R. Hunt, and M. M. Rogers. The turbulent/non-turbulent interface bounding a far wake. *Journal of Fluid Mechanics*, 451:383–410, January 2002. ISSN 0022-1120. doi: 10.1017/s0022112001006759.

[144] K. Chauhan, J. Philip, C. M. de Silva, N. Hutchins, and I. Marusic. The turbulent/non-turbulent interface and entrainment in a boundary layer. *Journal of Fluid Mechanics*, 742:1–33, March 2014. ISSN 0022-1120. doi: 10.1017/jfm.2013.641.